INVESTIGAÇÃO DA ABSORÇÃO ACÚSTICA DE MONÓLITOS DE AL2O3/MGO PRODUZIDOS VIA FREEZE-CASTING.

Tome Seichi da Nóbrega Guenka

Dissertação de Mestrado
Ciências Mecânicas

UNIVERSIDADE DE BRASÍLIA

Faculdade de Tecnologia
Departamento de Engenharia Mecânica

UNIVERSIDADE DE BRASÍLIA
FACULDADE DE TECNOLOGIA
DEPARTAMENTO DE ENGENHARIA MECÂNICA

INVESTIGAÇÃO DA ABSORÇÃO ACÚSTICA DE MONÓLITOS DE AL2O3/MGO PRODUZIDOS VIA FREEZE-CASTING.

Tome Seichi da Nóbrega Guenka

Orientador: Marcela Rodrigues Machado, Dr. Sc (ENM/UnB)

Co-orientador: Alysson Martins Almeida Silva

DISSERTAÇÃO DE MESTRADO

PUBLICAÇÃO: ENM.DM - XXX.XXX

BRASÍLIA/DF: 5 de abril de 2023

UNIVERSIDADE DE BRASÍLIA
FACULDADE DE TECNOLOGIA
DEPARTAMENTO DE ENGENHARIA MECÂNICA

Investigação da absorção acústica de monólitos de Al2O3/MgO produzidos via freeze-casting.

Tome Seichi da Nóbrega Guenka

DISSERTAÇÃO DE MESTRADO SUBMETIDA AO DEPARTAMENTO DE ENGENHARIA MECÂNICA DA FACULDADE DE TECNOLOGIA DA UNIVERSIDADE DE BRASÍLIA COMO PARTE DOS REQUISITOS PARCIAIS PARA A OBTENÇÃO DO GRAU DE MESTRE EM CIÊNCIAS MECÂNICAS.

APROVADA POR:

Marcela Rodrigues Machado, Dr. Sc (ENM/UnB)
(Orientador)

Dachamir Hotza, Dr. Sc. (UFSC)
(Examinador Externo)

Paulo Henrique Mareze, Dr. Sc. (UFSM)
(Examinador Externo)

BRASÍLIA/DF, 5 DE ABRIL DE 2023.

FICHA CATALOGRÁFICA

Guenka, T. S. da N.
Investigação da absorção acústica de monólitos de Al2O3/MgO produzidos via freeze-casting.
[Distrito Federal] 2022.
xvii, 84p. (ENM/FT/UnB, Mestre, Ciências Mecânicas, 2022.
Dissertação de Mestrado - Universidade de Brasília.
Faculdade de Tecnologia.
Departamento de Engenharia Mecânica.
Palavras-chave:

1. Absorvedor acústico	2. Cerâmica porosa
3. Freeze-casting	4. JCAL
I. ENM/FT/UnB	II. Título (série)

REFERÊNCIA BIBLIOGRÁFICA

Guenka, T. S. da N.(2022). Investigação da absorção acústica de monólitos de Al2O3/MgO produzidos via freeze-casting.. Dissertação de Mestrado, Publicação ENM.DM - XXX.XXX, Departamento de Engenharia Mecânica, Universidade de Brasília, Brasília, Distrito Federal, xvii, 84p.

CESSÃO DE DIREITOS

NOME DO AUTOR: Tome Seichi da Nóbrega Guenka.

TÍTULO DA DISSERTAÇÃO DE MESTRADO: Investigação da absorção acústica de monólitos de Al2O3/MgO produzidos via freeze-casting..

GRAU / ANO: MESTRE / 2022

Tome Seichi da Nóbrega Guenka

Para minha família

Agradecimentos

Agradeço primeiramente a minha família pelo contínuo e afetuoso suporte desde o começo de minha trajetória acadêmica e profissional.

A meus amigos, amigas e amigues pelo apoio e descontração em inúmeros momentos.

Aos colegas do Grupo de Dinâmica de Sistemas pelas aulas em tópicos que eu jamais compreenderia sem suas pacientes explicações, e pelas risadas.

Às queridas colegas do LMCNano, pelo auxílio em cotidianamente no laboratório, em especial ao Rodrigo, pelas inúmeras caracterizações. Também aos membros do projeto Petronas, Luiz e Daniel, pelas caracterizações e pelos ensinamentos.

A professora Maria Alzira, pela permissão de uso de seus equipamentos e pela instrução. A Maria dos Reis, pelo inestimável auxílio na operação do tubo de imperdância.

Ao pessoal da CPRM pelo auxílio no uso do microscópio, principalmente Jo e Kotaro.

A querida professora Marcela, pelos quase 5 anos de preciosa, paciente orientação e apoio fundamentais para minhas conquistas, e ao professor Alysson que me aceitou mesmo tendo justificativas para não fazê-lo e me mostrou o mundo da ciências dos materiais como eu nunca havia o experenciado.

Aos amigos Pedro Zepp, Natália Montenegro e Ana Clara Queiroz pelos incontáveis almoços no RU e pela amizade.

Um agradecimento especial ao amigo e co-autor Arthur Bizzi, pela preciosa amizade que dura tantos anos e cooperação acadêmica.

A minha querida namorada Anna Clara, por me acompanhar e aturar durante toda essa jornada.

Finalmente agradeço à qualquer pessoa que tenha acreditado em meu trabalho durante esse período, àqueles que torceram por mim apenas interessados em ver minha felicidade, mesmo nos momentos mais complicados.

Resumo

Investigação da absorção acústica de monólitos de Al2O3/MgO produzidos via freeze-casting.

Autor: Tome Seichi da Nóbrega Guenka

Orientador: Marcela Rodrigues Machado, Dr. Sc (ENM/UnB)

Coorientador: Alysson Martins Almeida Silva

Programa de Pós Graduação em Ciências Mecânicas

Brasília, 5 de abril de 2023

Absorvedores acústicos são materiais de ampla aplicação em engenharia acústica e arquitetura. Atualmente inúmeras opções desses materiais estão disponíveis, enquanto várias outras estão sendo pesquisadas. Buscando propor novas soluções com diferenciais dificilmente encontrados, como resistência a ambientes agressivos, o presente estudo investigou as propriedades acústicas de cerâmicas porosas produzidas via *freeze-casting*. Baseadas nos solventes Dimetil Sulfóxido (DMSO) e Canfeno, as amostras foram produzidas com variação de parâmetros do processo de *freeze-casting*, obtendo assim grupos com características finais (e.g. porosidade e composição de fases) diferentes. As amostras de cerâmica produzidas foram caracterizadas utilizando métodos numéricos e experimentais relacionados à acústica e também relacionados à microstrutura. Obteve-se amostras com coeficiente de absorção sonoro acima de 0,7 dentro da faixa de frequência de 1000 Hz-6300 Hz, e características microstruturais observadas nas amostras obtidas, como variação de microstrutura dentro de uma amostra, foram relacionadas às propriedades absorção acústica.

Key-words: Freeze-casting, absorvedor acústico, cerâmica porosa, espinélio.

Abstract

INVESTIGATION OF THE ACOUSTIC ABSORPTION OF AL2O3/MGO MONOLITHS PRODUCED VIA FREEZE-CASTING.

Author: Tome Seichi da Nóbrega Guenka

Advisor: Marcela Rodrigues Machado, Dr. Sc (ENM/UnB)

Co-advisor: Alysson Martins Almeida Silva

Master in Mechanical Sciences

Brasília, 2022

Acoustic absorbers are materials with widespread application in acoustic engineering and architecture, and currently, countless options for such materials are available, and many more are being researched. In aiming to propose new solutions with hardly found features, such as resistance to aggressive environments, the present study investigated the acoustic properties of porous ceramics produced via freeze-casting. Based on Dimethyl Sulfoxide (DMSO) and camphene, the samples were produced with variations of the set of freeze-casting process parameters, consequently obtaining sample groups with different characteristics (e.g. porosity and phase composition). The ceramic samples were characterized using numerical and experimental methods related to sound propagation and microstructure. Samples with sound absorption coefficients values upwards of 0.7 in the studied 1000 Hz-6300 Hz frequency range were obtained, and observed microstructure characteristics such as porosity grading inside samples, were related to the sound absorption characteristics.

Key-words: Freeze-casting, sound absorber, spinel, porous ceramic.

Summary

List of Figures

List of Tables

List of Abbreviations and Acronyms

FEM	Finite Element
ISO	International Standards Organization
PUC	Periodic Unit Cell
REV	Representative Elementary Volume
SEM	Scanning Electron Microscope/Microscopy
TMM	Transfer Matrix Method
XRD	X-Ray Diffraction

List of Symbols

η_f	Dynamic Viscosity [Pa $\cdot$ s]
r	Electrical resistivity [n.u.]
T_f	Freezing temperature [°C]
K_a	Fluid Adiabatic Bulk Modulus [Pa]
ρ_f	Fluid density [$\frac{\mathrm{kg}}{\mathrm{m}^3}$]
Φ	Fluid Displacement Potential [n.u]
p	Fluid pressure [Pa]
v	Fluid velocity [n.u.]
α_∞	High-Frequency Limit of Tortuosity [n.u.]
σ_{er}	Impedance Measurement Standard Deviation [n.u]
ν_f	Kinematic Viscosity [$\frac{\mathrm{m}^2}{\mathrm{s}}$]
ϕ	Porosity [%]
γ	Ratio of Specific Heats [n.u.]
α	Sound Absorption Coefficient [n.u.]
c	Speed of Sound [$\frac{m}{s}$]
σ	Static Air Flow Resistivity [Nsm^{-2}]
k_0'	Static Thermal Permeability [m^2]
k_0	Static Viscous Permeability [m^2]
Z_S	Surface Impedance [$\frac{\mathrm{Pa\cdot s}}{\mathrm{m}}$]
λ'	Thermal Characteristic length [μm]
λ	Viscous Characteristic length [μm]
k	Wave number [m^{-1}]

1 Introduction

Porous ceramics (ceramic foams) has been an area of focus inside the ceramic materials field of study and is increasingly gaining attention from recent advances in manufacturing technologies and applications. Controlled porosity allows ceramic materials to overcome limitations usually found in nearly non-porous ceramics, e.g. strain tolerance, usually used in common applications such as household utensils and refractories. Aside from this feature, such porosity improves thermal and acoustic isolation, yields higher specific area, and lowers density. Ceramic materials with tailored porosity may thus be used for a plethora of engineering applications, one of which being sound absorbers.

Sound absorbers are a fundamental part of noise-sound control solutions. One of the main types of absorbers is porous materials (COX; D'ANTONIO, 2016). For such materials, absorption traits and effectiveness are related to the dissipation of sound waves inside the pore structure due to thermal and viscous effects and structural coupling effects (ALLARD; ATALLA, 2009). Such phenomena are directly correlated to porosity and pore structure, yet further in materials where the effects from body vibration are negligible (cases in which the rigid-body assumption is valid), making the control of these properties the main investigation subject for the development of new foams. Some sound absorption applications may depend on the survivability of the absorbent material in extreme environments and conditions such as corrosion and high temperature. In this case, using ceramic material in sound control in hazardous conditions can bring a potentiality of this material over the normally used for sound absorption.

Porosity in ceramic materials can be controlled by varying the method (e.g. direct foaming, sacrificial template) used for the production of samples and these method's parameters, such as component concentration (STUDART et al., 2006). Among the controlled porosity characteristics are pore size, orientation, and shape. Common applications to porous ceramics are filtering/separation membranes, where pore morphology is a paramount factor for application, though others such as insulation and absorption (thermal, acoustic, and even electromagnetic). For further references in applications of porous ceramics, see Eom, Kim e Raju (2013), Chen et al. (2021).

One of the main processes used to manufacture ceramic materials is freeze-casting (also known as ice-templating). This method produces a suspension containing the main material components (e.g. alumina, zirconia), freezing such suspension, sublimating the

frozen fluid and sintering the remaining structure. Freeze-cast ceramics give good pore shape and size control by controlling different freezing parameters, such as cooling direction (e.g. unidirectional, bi-directional, radial) and solid loading in the suspension phase. Like other fabrication routes, freeze-cast ceramics may be used for tailored applications such as energy-related ones (e.g. solid oxide fuel cells, gas separation, catalytic membrane reactors) (GAUDILLERE; SERRA, 2016), acoustic absorption (RIES et al., 2013), emulsion separation (USMAN; KHAN, 2021) and even the production of piezoelectric ceramics for ultrasound transducers (RYMANSAIB et al., 2022). In matters of cost-effectiveness, the additional freezing and sublimation steps necessary for this route summed to higher-cost solvents commonly used (e.g. camphene), may raise the cost of ceramic processing when compared to other possible routes. Nevertheless, there are cost-reducing options such as the use of lower-cost solvents like water (e.g. (TANG et al., 2014)), and hydrogenated vegetable oil (VIJAYAN; NARASIMMAN; PRABHAKARAN, 2014) (which also will reduce costs associated with freeze-drying, due to its sublimation in ambient atmosphere). Another matter of this route is the scalability of the process, as pointed out in Scotti e Dunand (2018), due to the already mentioned issues of process intricacies and ingredients which will also affect the viability of large-scale production. Options such as tape-casting (REN; ZENG; JIANG, 2007) allow production on greater scales, though research is still necessary in this regard.

This work aims to investigate the acoustic absorption properties of freeze-cast corundum (Al_2O_3-α)/MgO ceramics. Such properties will be correlated to the obtained samples' physical and microstructural properties to acquire a solid basis for future research on freeze-cast ceramics in sound-absorbing applications.

1.1 Porous material acoustic modeling

With widespread use for noise control in multiple contexts, porous materials are very diverse in their microstructural and mechanical properties hence having different acoustic absorption behaviour among their possibilities. For more efficient prediction and optimisation of porous material performance (and also an understanding of the phenomena responsible for sound dissipation of these materials), theoretical models of acoustic propagation through porous materials were developed.

One of the first models of wave propagation in poroelastic media saturated by viscous fluid was proposed by Biot in 1956 (BIOT, 1956a; BIOT, 1956b) where three types of waves are said to propagate through the solid-fluid medium: two compressional waves and a shear wave. The compressional waves propagate as separate waves through the frame and air when there is no while coupling between the two. When weak coupling happens, the wave which propagated solely through the frame now also propagates via the air phase. The shear wave will propagate solely through the frame when appropriately

excited. This model was fundamental for analysing different porous media, though it is very complex and difficult to implement. From this, other simpler models were created, departing from Biot's model using assumptions relative to characteristics of the porous materials, such as rigid or limp skeleton assumption. These simplified models are further discussed in Section 2.1.

1.2 Porous ceramics

In the literature, several papers have proposed different ways for the obtention of porous ceramics have been published. These methods may be divided into four main categories (STUDART et al., 2006; CHEN et al., 2021):

- Partial sintering;
- Direct foaming;
- Sacrificial template;
- Replica (template).

The four categories have within their reports methods capable of producing macroporous ceramics. **Partial sintering** consists of lowering the sintering temperature or increasing the heating rate to promote reduced densification of the green body and thus allow for forming pores between grains. In **direct foaming**, the slurry is subjected to the dispersion of gas bubbles, stabilising the structure formed by these bubbles so that they don't coalesce and later treating the formed ceramic structure. **Sacrificial templating** is defined by the dispersion of sacrificial inclusions in the green body that are removed during a later process (e.g. freeze-drying, heating) through a different physical process (e.g. sublimation, melting), leaving a negative replica of the template. **Replica templating** is similar to sacrificial templating, although now using the template (usually a polymeric foam) as a mold to which the ceramic material adheres, forming a coating. The template is removed, and the ceramic foam (now a replica of the former template) is sintered. Figure 1.1 shows an illustration of the main steps involved in these routes.

Studart et al. (2006) and Chen et al. (2021) include freeze-casting in the family of sacrificial templating. Some of the main aspects common to sacrificial templating routes are the direct relation of the template shape and dimensions to the pore shape and dimensions and of template concentration to final ceramic total porosity (CHEN et al., 2021). Similarly, for freeze-casting, where the template is initially liquid, the formed pores are molded to the shape and dimensions of the solid structures created during freezing, and the porosity is dependent on the solvent proportion to the solid phase in slurry preparation. Hence, the solidified solvent geometry defines the final pore structure. Different parameters determine them, like the type of solvent, freezing speed and direction, and slurry solid concentration,

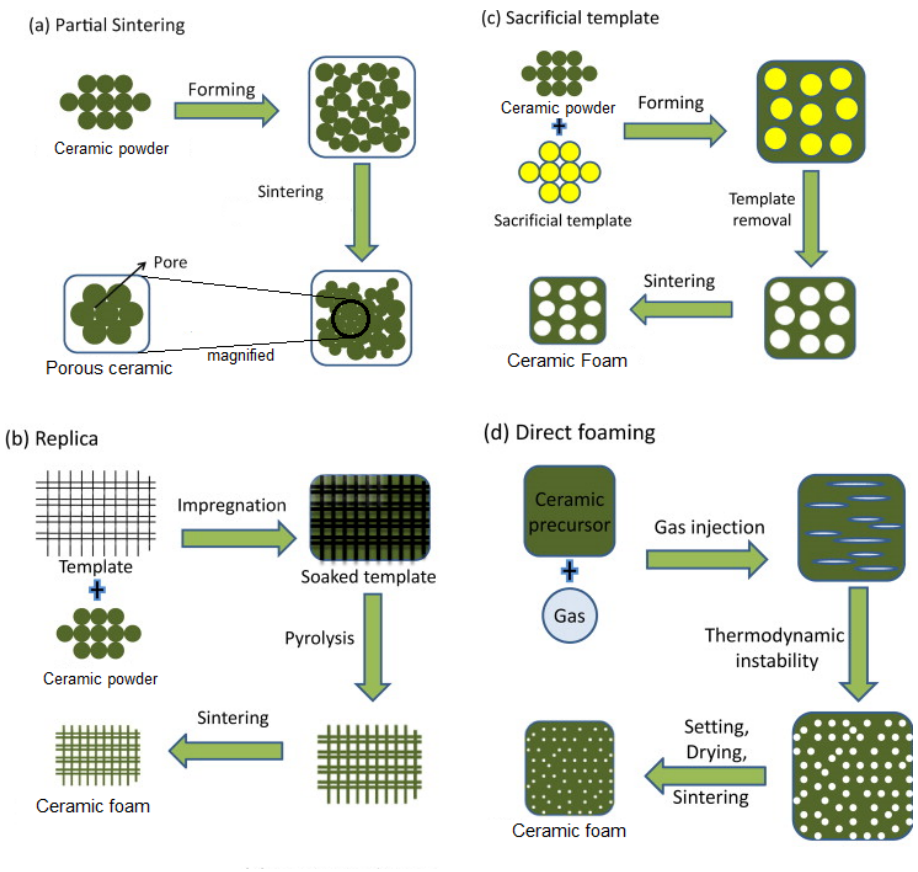

Figure 1.1 – Main categories of porous ceramic fabrication routes. Adapted from Eom, Kim e Raju (2013)

among others (DEVILLE, 2008). Different types of solvent have been shown to produce various shapes of pores, e.g. water has been shown to produce lamellar structures (PAPA et al., 2015), prismatic pores have been obtained from Tert-Butyl-Alcohol (XU; WANG, 2016), and varying pore shapes from solvent mixtures (FU et al., 2008; RAHAMAN; FU, 2008).

1.3 Literature review

Early studies on the sound absorption of porous ceramics already pointed out the aforementioned benefits of ceramic foams but focused on the acoustical modelling of the sound absorption based on the evaluated properties of the ceramic samples (mainly porosity and flow resistivity), paying little attention to fabrication route. Takahara (1994), aiming at investigating the possibility of open pore ceramics use for sound absorption, evaluates the absorption coefficients, flow resistivity and porosity of Al_2O_3/SiO_2 samples with different grain sizes. The grain size was controlled mostly by the initial ceramic powder particulate size. The flow resistivity and porosity measurements are used to examine the relation between these properties and sound absorption while also being fed to the model presented by Beranek (1947) to compare the fit of experimental and theoretical results. In the work of Shirahatti e Munjal (1987), the authors perform a similar analysis of Takahara

(1994), using experimental porosity and flow resistivity values in theoretical models and comparing the resulting sound absorption coefficients to experimentally obtained curves. Therefore, the authors use two additional models (namely those by Mechel (1976) and Attenborough (1983a)) to evaluate the best model to describe ceramic tile absorption. It is interesting to notice that in these studies, the missing ceramic material information necessary to the models (not available through direct measurements) is simply assigned by the authors with no mathematical fitting method (e.g. least squares), rather by visual evaluation.

Since then, more studies have been conducted with a greater focus on controlling final microstructure properties through adjustment of process parameters and on the relation between such microstructure and the evaluated acoustic properties. Cuiyun et al. (2012) produced zeolite samples using the sacrificial template, achieving porosity up to 76 % while maintaining good control of pore size by using controlled-size polymer foam spheres as a template. In their study, Cuiyun et al. (2012) also evaluated the samples' air flow resistivity and used it associated with the measured porosity to obtain the sound absorption coefficients through the Johnson-Champoux-Allard (ALLARD, 1993) and Delany-Bazley model (DELANY; BAZLEY, 1970), reaching a decent fit of numerical and experimental results for all samples. Also, using the sacrificial template, Chen, Liu e Sun (2020) produces zeolite samples with pore size controlled by varying the diameter of spheres used as templates, showing better absorption by the larger pore samples when compared to the smaller pore samples.

Research on gelcasting method studied the consequences of different process components and fabrication route variations, showing ways to obtain higher total porosity associated with larger pore size, which was shown to improve sound absorption (FUJI et al., 2006; ZHANG et al., 2006). Later, both Frank, Christian e Dietmar (2011) and Carlesso et al. (2013) used freeze-gelation, a sol-gel route modified by a freezing step whose final influence in the pore structure follows the same principle as that of freeze-casting, combined with sacrificial templating to obtain samples with bimodal porosity, resulting in sound absorption coefficients above 0.6 and up to greater than 0.9 in low frequencies ($\leq$ 800 Hz).

Another fabrication route, commonly used to produce porous ceramics for sound absorption studies, is direct foaming. This method involves mixing chemical pore-forming agents in the slurry during its preparation. These agents will expand, forming spaces between the ceramic powders during either mixing or firing. Studies based on this kind of method can obtain pores with large average size ($\geq$ 50 μm) within a broad range of porosities, from intermediate to very high and consequently reach sound absorption coefficients upwards of 0.8 (WANG; LIU; GU, 2017; WANG et al., 2017; DU et al., 2020a).

Some distinct methods that do not necessarily fit into the aforementioned four fabrication route categories have also been studied in acoustical applications. Hot-pressure sintering is used by Yan et al. (2020) to produce porous zirconium carbide samples, and

variation of fabrication parameters are shown to shift absorption peaks and increase/decrease their maximum value, a change associated with pore size variation. Another category of porous ceramic that has attracted extensive attention is aerogels. These ceramics have porosities upwards of 95 % and consequently can obtain high absorption coefficient values even at lower frequencies while having different attractive properties such as high thermal insulation and compression resistance (YAN et al., 2020; JIA et al., 2020; HE et al., 2021; XIE et al., 2021; CAO et al., 2022; ZONG et al., 2022; DONG et al., 2022).

Finally, freeze-casting is attractive for sound absorption due to its various possible pore structures and good control of porosity, although the literature on freeze-cast ceramics for such applications is scarce. Aside from the mentioned freeze-gelation cited studies, silica foams were produced using unidirectional freeze-casting by Du et al. (2020b) with TBA as a solvent and investigated the correlation of average pore size and porosity to sound absorption and airflow resistance.

1.4 Objectives

Using diverse experimental and numerical methods, the present work aims to investigate the acoustic properties of experimentally produced porous ceramic Al_2O_3/MgO samples. The specific objectives are:

- Understand the main models used for porous material sound propagation, its theoretical aspects, and applications;
- Produce porous ceramic samples via the freeze-casting route with possible applications in sound absorption solutions;
- Investigate the correlation between fabrication parameters and obtained acoustic behavior through theoretical models.
- Investigate the correlation between sample chemical phases and material efficiency in sound absorption.

1.5 Methodology

A brief theoretical review of available models for rigid-frame porous material acoustic properties is conducted. Due to its completeness in the description of material microstructure influence on sound absorption when compared to other simpler models, the Johnson-Champoux-Allard-Lafarge (JCAL) model (JOHNSON; KOPLIK; DASHEN, 1987; CHAMPOUX; ALLARD, 1991; LAFARGE et al., 1997) was chosen for our studies. A description of its parameters (and methods for their estimation) is provided. The main method chosen for estimating model parameters, inverse characterization (model

calibration), is implemented, and testing on different approaches to this calibration is conducted using numerically generated (synthetic) results. Additionally, a small study is conducted on applying inverse methods to multi-layer systems.

Experimentally, samples with different mass ratios of Al_2O_3/MgO are produced via freeze-casting using two different unidirectional freezing setups that enable different freezing temperatures. The freezing procedure used in the present work is similar to the unidirectional one reported by (ARAúJO et al., 2018). Aside from different chemical compositions and freezing temperatures, samples are produced using different solvents, namely Dimethyl Sulfoxide (DMSO) and camphene, and different solid loading in slurry preparation.

Final sample acoustic properties are evaluated using impedance tube testing associated with the implemented inversion method. Material properties are also characterized using Archimedes' principle porosity testing, Scanning Electron Microscopy (SEM, Quanta FEI 450), X-ray powder Diffraction (XRD, Shimadzu XRD-6000), and Micro Computed Tomography (μ-CT, Heliscan Mk 1).

1.6 Text Organisation

The present work is organised into 6 chapters. The first chapter presents an introduction to the modelling of porous materials as sound absorbers and to the production of porous ceramics, besides presenting an overview of the conducted studies. Chapter two presents the theoretical aspects of modelling porous materials, and delves into the JCAL model formulation, measurements of its parameters, and application to multi-layer systems. Chapter three consists of a brief overview of the main aspects of the experimentally produced ceramics, the freeze-casting method, and porosity assessment using Archimedes principle. Chapter four presents the numerically obtained results for inverse characterisation techniques applied to single and multi-layer systems. Finally, chapter five shows the experimentally obtained acoustic and material characterisations for different types of samples and discusses the relations between those. Chapter 6 presents the conclusion of the present work.

2 Acoustic Modeling

2.1 Categories of models

Many sound propagation models are available in the literature, each focusing on different aspects of the acoustic phenomena and paths to obtain its mathematical formulation. There are four main categories for the models that use the assumption of rigid frame: empirical, analytical (phenomenological), semi-phenomenological and microstructure (MAREZE, 2013).

Empirical models are those obtained by associating experimental impedance results of samples to other properties measured from them. The main example of empirical models is that presented by Delany e Bazley (1970) and its proposed variations (MECHEL, 1976; MIKI, 1990). The authors relate characteristic impedance and wave number (propagation coefficient/constant) obtained from numerous fibrous material samples to their respective static air flow resistivity. A power-law relation is observed between the experimental results for wave number and characteristic impedance and the measured resistivity, enabling the formulation of a one-parameter (resistivity) model for the acoustic properties of fibrous materials.

Analytical models are based on the solution of fluid flow and acoustic field equations for simplified pore geometries, such as cylinders and slit channels. Available simplifying assumptions enable analytical solutions using pore shape and bulk properties. The seminal work by Zwikker e Kosten (1949) is a great demonstration of this type of model, simplifying the sound propagation equations in tube obtained by Kirchhoff (1868) and defining an equivalent density and equivalent bulk modulus, both complex quantities, used for obtaining tube characteristic impedance and wave number. These properties can later be used to obtain the impedance of a layer of a porous material composed of straight cylindrical tubes.

Considering that it is virtually impossible to propose analytical models that describe sound propagation through common porous materials in all their intricacy, semi-phenomenological models extend analytical models by proposing analogous properties representative of large-scale samples to obtain wave propagation parameters. These properties are available experimentally from accessory tests, showing an average behaviour of the

full sample without considering the intricacies of the varying complicated microstructure. Attenborough's model (ATTENBOROUGH, 1983b), for example, departs from Zwikker & Kosten's model and expands it into a model descriptive of granular and fibrous media, depending on porosity, pore shape factor, air flow resistivity and static tortuosity of the material.

Microstructure-based models follow the same principle as the analytical ones, although the solution is obtained using numerical procedures of the necessary equations of sound propagation. The evolution of numerical methods allows solving those equations for complex pore geometries in computational replicas. Often called Representative Elementary Volume (REV) or Periodic Unit Cell (PUC) (ZIELINSKI et al., 2020), these replicas four are constituted by idealised small volumes representing approximations of the geometry of porous materials. Once numerical solutions are obtained, the found pore properties are usually applied to semi-phenomenological (DOUTRES; ATALLA; DONG, 2011) or empirical models (SOLTANI; NOROUZI, 2020). The resulting impedance/absorption may be used for different applications: simple comparison to experimental results (REN et al., 2022), material absorption prediction (SOLTANI; NOROUZI, 2020) or used for optimisation (BOULVERT et al., 2019). In other instances, the dynamic permeability and tortuosity are obtained directly from PUC geometry through the solution of harmonic fluid flow. In cases where the geometry is simple enough, the flow equations are solved for a complete layer of material adjacent to a boundless fluid, obtaining its response to acoustic excitation. This method has grown in popularity, and many papers have been published recently. Nevertheless, a good example of the early works that use this method is that by Gasser, Paun e Bréchet (2005) where the author uses the Finite Element Method (FEM) to obtain the parameter of a semi-phenomenological method, reaching final results close to those of other previous works that analyse material described by similar geometries.

2.2 Equivalent Fluid Modelling

For this present work, the main model used for evaluating the produced porous ceramic samples was the JCAL model, one of the most important and widely used in the semi-phenomenological category. Its extensive application provides significant literature and references on the topic, besides proving its effectiveness in describing these materials.

The JCAL model pertains to the equivalent fluid models category. The work of Zwikker e Kosten (1949), besides having importance as a model in itself, brought the important contribution of equivalent fluid modelling. This class of models replaces the absorber material layer with an equivalent fluid layer whose properties are calculated based material related parameters.

2.2.1 Sound Propagation in a fluid layer

Before proceeding to the description of equivalent fluid models, it is necessary to understand the propagation of sound in an unbound fluid. The equations of sound propagation in an inviscid, compressible fluid are an important starting point. Considering small disturbances, the wave equation may be written as in Eq. 2.1, considering the stress-strain relations for an isotropic elastic medium (ALLARD; ATALLA, 2009)

$$\nabla \left[K_{\mathrm{a}} \nabla^2 \Phi - \rho_{\mathrm{f}} \frac{\partial^2}{\partial t^2} \Phi \right] = 0, \tag{2.1}$$

where K_{a} is the fluid adiabatic bulk modulus, Φ is the displacement potential, and ρ_{f} is the fluid density.

The wave equation may also be expressed in terms of pressure variation around equilibrium pressure (FAHY; GARDONIO, 2007), shown in

$$\nabla^2 p = \frac{1}{c^2} \frac{\partial^2 p}{\partial t^2}, \tag{2.2}$$

where c is the speed of sound given by $c^2 = (\gamma P_0 / \rho_{\mathrm{f}})$, P_0 the mean ambient pressure, and γ the temperature-independent specific-heat ratio γ of the fluid (PIERCE, 2019). This form of the wave equation is obtained from two fundamental fluid motion governing laws: the continuity equation (Eq. 2.3) and the Euler momentum equation (Eq. 2.4) as

$$\frac{\partial \rho}{\partial t} + \nabla \cdot (\rho_{\mathrm{f}} \mathbf{v}) = 0; \tag{2.3}$$

$$\rho \frac{Dv}{Dt} = -\nabla p. \tag{2.4}$$

Equations 2.3 and 2.4 are the starting point of the works that constitute the discussed semi-phenomenological models. Moreover, from the different forms of the equation of motion presented in Eqs. 2.1, 2.2, the characteristic wave number and impedance of a fluid can be obtained from their solutions - two fundamental concepts that will be expanded to the analysis of porous materials' acoustic behaviour. From Eq. 2.1, we can develop the stress-strain relations of a fluid. The pressure relative to potential is

$$p = -K_{\mathrm{a}} \nabla^2 \Phi, \tag{2.5}$$

while the fluid velocity, from the definition of displacement potential, yields

$$\boldsymbol{v} = \frac{\partial}{\partial t} \left(\nabla \Phi \right). \tag{2.6}$$

For a wave propagating in a direction x, the solution for Φ is presented by

$$\Phi = \frac{A}{\rho \omega^2} e^{[j(-kx + \omega t) + \alpha]}, \tag{2.7}$$

where A and α are arbitrary constants, ω is the wave frequency and k is the wave number. Considering Eq. 2.1, the wave number k is found to be

$$k = \omega(\rho/K)^{\frac{1}{2}}. \tag{2.8}$$

Additionally, the characteristic impedance Z_c of fluid is obtainable from Eqs. 2.5 and 2.6, yields

$$Z_c = (\rho K)^{\frac{1}{2}}. \tag{2.9}$$

In the situations where viscosity effects are non-negligible, Eqs. 2.8, 2.9 and their relations to fluid velocity and pressure still apply. Nevertheless, in such cases, the density and bulk modulus are complex quantities (ALLARD; ATALLA, 2009).

2.2.2 Zwikker & Kosten Model

The equations used in the Zwikker & Kosten model for a porous material are analogous to those of an unbound fluid. As mentioned, this model is restricted to materials whose pores are straight cylindrical tubes with a specific radius. However, further models would use the equivalent fluid modelling for more generalised pore geometries.

To achieve the material equations, first the tube properties are necessary. As in the case of a fluid layer, characteristic impedance Z_c and wave number k of a tube is given by (STINSON, 1991)

$$Z_c = [\rho_{\text{eq}}(\omega)K_{\text{eq}}(\omega)]^{1/2}; \tag{2.10}$$

$$k^2 = \omega^2\rho_{\text{eq}}(\omega)/K_{\text{eq}}(\omega), \tag{2.11}$$

where ρ_{eq} is the equivalent fluid density and K_{eq} its bulk modulus. Both these quantities are complex and functions of frequency, with parameters related to pore geometry (may be obtained analytically for simplified pore geometries such as cylinders and slits) and saturating air properties.

As presented in Allard e Atalla (2009), the tube acoustic properties may be extended to obtain the impedance surface of a material composed of parallel tubes. Here, porosity "ϕ" is defined as the ratio between interconnected pore volume V_T inside a porous sample and its total volume V_T, as shown in

$$\phi = \frac{V_a}{V_T}. \tag{2.12}$$

The porosity definition presented in Eq. 2.12 may differ slightly from the open porosity defined in Eq. 3.7 due to dead-end pores, i.e. pores with connection to the atmosphere that does not form an interconnected network with other pores, that inevitably will be measured in open pore volume defined in Sec. 3.3. Some studies have been conducted on

the dead-end pore effect on sound absorption (CHEVILLOTTE; PERROT; PANNETON, 2010), and measurement of its volume (DUPONT; LECLAIRE; PANNETON, 2013).

Under the consideration of a pore structure composed of homogeneously distributed pores through the bulk, the porosity, a volume property, also reflects the material/air surface relation, which is the case of the materials covered by the Zwikker & Kosten model. Then, to calculate the surface impedance of this material layer, two points of the surface are chosen: a point M_1 inside the material and a point M_2 in free air, as shown in Fig. 2.1.

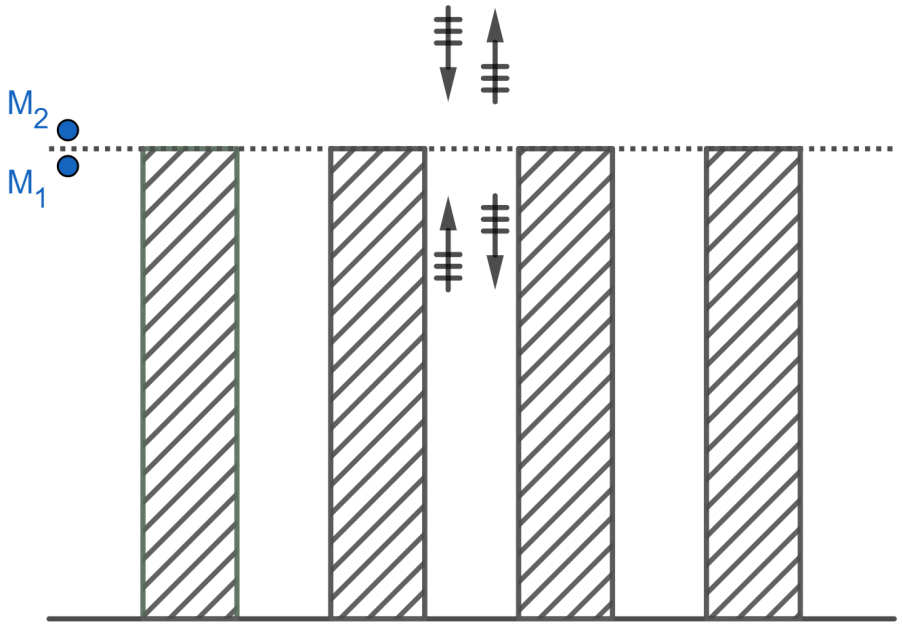

Figure 2.1 – Simplified transverse cut of the porous material layer.

In the case of normal incidence, assuming the non-normal components of velocity close to the solid surface to be negligible (plane field) and the air velocity to be the same in all pores, the pressure and velocity continuity relations at the boundary are presented by

$$p(\mathrm{M}_2) = p(\mathrm{M}_1); \tag{2.13}$$

$$v(\mathrm{M}_2) = \phi v(\mathrm{M}_1), \tag{2.14}$$

where $p(\mathrm{M}_2)$ and $p(\mathrm{M}_1)$ are the air pressures in free air and inside the pores, respectively, and $v(\mathrm{M}_2)$ and $v(\mathrm{M}_1)$ the average air velocities for the same regions close to the surface. The impedances at points M_1 and M_2 are given by

$$Z(\mathrm{M}_1) = p(M_1)/v(M_1), \quad Z(\mathrm{M}_2) = p(M_2)/v(M_2), \tag{2.15}$$

and are, considering Eqs. 2.13, 2.14 correlated by

$$\phi Z(M_2) = Z(M_1). \tag{2.16}$$

Finally, using the impedance translation theorem applied to a fluid layer with height h backed by a rigid impervious backing (ALLARD; ATALLA, 2009) and considering Eqs. 2.11,2.10, the impedance of at point M_1 is given

$$Z(M_1) = -jZ_c\text{cotg}(kh). \tag{2.17}$$

Consequently, the impedance at point M_2 is given by

$$Z(M_2) = -\frac{jZ_c}{\phi}\text{cotg}(kh). \tag{2.18}$$

2.3 Johnson-Champoux-Allard-Lafarge model

Although the Zwikker & Kosten model presented a very important contribution, its applicability is restricted. Posterior to the presentation of such a model, further models aimed at expanding the scope of their use to other more complicated and thus more realistic (common) pore geometries. These may be semi-phenomenological or microstructure based, as mentioned in Section 2.1.

One of the main semi-phenomenological models with widespread use is the so-called Johnson-Champoux-Allard-Lafarge (JCAL) model. It is an equivalent fluid model and is the result of contributions by multiple researchers. Originally proposed to describe the complex equivalent fluid density of a rigid (motionless), isotropic porous material, the model proposed by Johnson, Koplik e Dashen (1987) was then complemented with the model by Champoux and Allard (CHAMPOUX; ALLARD, 1991) that further elaborated the equivalent bulk modulus behaviour at high frequencies for the same materials. Finally, Lafarge et al. (1997) suggested changes to the bulk modulus equation to correct the lacking description of low-frequency thermal phenomena in the previous models, leading to the JCAL model.

2.3.1 Johnson‘s dynamic permeability and tortuosity

In the work of Johnson, Koplik e Dashen (1987), the authors state that for a porous medium saturated by an incompressible Newtonian fluid, whose pores and grains are much smaller than the sound wavelength and under a macroscopic pressure gradient $\nabla P e^{-j\omega t}$, the following equations relate the pressure gradient and the velocity as

$$\alpha(\omega)\rho_\text{f}\frac{\partial \mathbf{v}}{\partial t} = -\nabla P; \tag{2.19}$$

$$\phi\mathbf{v} = -\frac{k(\omega)}{\eta_\text{f}}\nabla P, \tag{2.20}$$

where ρ_f is the saturating fluid density, η_f its dynamic viscosity. Variable $\mathbf{v}$ is the average fluid velocity over an area A such that $\phi\mathbf{v}\cdot\hat{n}A$ is the fluid flow rate, where $\hat{n}$ is the outward

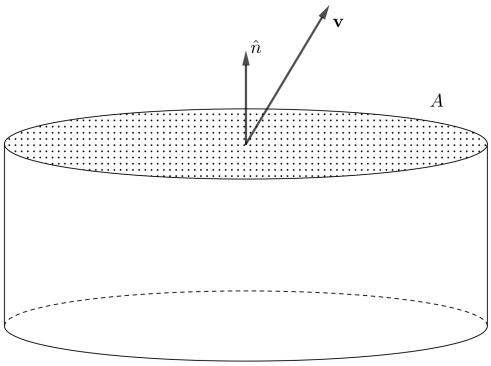

Figure 2.2 – Representation of average velocity **v**.

unit vector normal to the material surface, as shown in Fig. 2.2 (JOHNSON; KOPLIK; DASHEN, 1987).

Equation 2.19 is obtained from the momentum equations presented in Eq. 2.4, and Eq. 2.20 from Darcy's law, both applied to porous materials following the assumptions mentioned above and both containing functions dependent of frequency ω, thus describing sound propagation in that domain. These functions are the dynamic tortuosity $\alpha(\omega)$, related to the effective density by the relation $\rho_{\text{eq}} = \alpha(\omega)\rho_{\text{f}}$ (ALLARD; ATALLA, 2009); and the permeability $k(\omega)$, analogous to the permeability of Darcy Law for flow through porous media (SCHEIDEGGER, 1974). Johnson's model presents two final equations for the dynamic tortuosity and the permeability, respectively, by

$$\alpha(\omega) = \alpha_\infty + \frac{j\eta_{\text{f}}\phi}{\omega k_0 \rho_{\text{f}}} \left\{ 1 - \frac{4j\alpha_\infty^2 k_0^2 \rho_{\text{f}} \omega}{\eta_{\text{f}} \lambda^2 \phi^2} \right\}^{\frac{1}{2}}, \tag{2.21}$$

$$k(\omega) = \frac{k_0}{\left\{ 1 - \frac{4j\alpha_\infty^2 k_0^2 \rho_{\text{f}} \omega}{\eta_{\text{f}} \lambda^2 \phi^2} \right\}^{\frac{1}{2}} - \frac{j\alpha_\infty k_0 \rho_{\text{f}} \omega}{\eta_{\text{f}} \phi}}, \tag{2.22}$$

where α_∞ is the high frequency limit of the tortuosity, k_0 is the static viscous permeability, λ is the viscous characteristic length, ϕ is the material's porosity, ω is the frequency, ρ_{f} is the fluid density, η_{f} the fluid's dynamic viscosity. These are the porous material acoustic parameters that describe the wave propagation inside the pore channels.

Although the porosity parameter ϕ has been defined as the ratio between pore volume and total material volume, it is important to notice that for sound absorption and propagation, only open pores and interconnected pore channels are interesting, once no propagation (and hence no dissipation) occurs in closed pores (COX; D'ANTONIO, 2016). Therefore, for the presented models, porosity is referent to open porosity.

The parameter α_∞, called the high-frequency limit of tortuosity, is a dimensionless quantity representative of deviation in pore orientation from the axis parallel to sound

propagation direction and pore constriction variation (MAREZE, 2013). It describes the inertial effects of an ideal non-viscous fluid flow through porous media (COX; D'ANTONIO, 2016) and it is equivalent to the dynamic tortuosity for an ideal inviscid fluid saturating a porous medium, thus obeying the relation $\rho_{\text{eq}} = \alpha_\infty \rho_{\text{f}}$ for such a case (JOHNSON; SEN, 1981). For very high frequencies, the viscous skin depth, given by (LAFARGE et al., 1997)

$$\delta = \left(\frac{2\nu_f}{\rho_{\text{f}}\omega} \right)^{\frac{1}{2}}, \tag{2.23}$$

where ν_f is the fluid kinematic viscosity, becomes much smaller than the pore diameter, and the fluid flow is equivalent to that of the ideal fluid except for the narrow boundary layer. Thus, since the model is validated for both the high and low-frequency limit, the parameter α_∞ arises as a minimum value for the dynamic tortuosity as the frequency limit goes to infinity.

A mathematical definition of α_∞ is given by Johnson, Koplik e Dashen (1987) and the simplified version of it is given by Allard e Atalla (2009)

$$\alpha_\infty = \frac{\langle v_m^2(M) \rangle_V}{v^2(M_0)}, \tag{2.24}$$

where the $\langle\rangle$ brackets represent average, $v_m(M)$ is the microscopic inviscid flow velocity inside a pore at a point M, $v(M_0)$ is given by the average $v(M_0) = \langle v_m(M) \rangle_V$ inside a representative volume V around a point M_0. The inequality between the average of squares and the square of averages may be a reason for the $\alpha_\infty \geq 1$.

The static thermal permeability k_0 has similar significance to tortuosity in the sense of its obtention for a low frequency (close to 0); the frequency-dependent permeability will become the conventionally measured permeability k for a steady flow, used in Darcy Law as

$$\lim_{\omega \to 0} k(\omega) = k_0. \tag{2.25}$$

This parameter is commonly substituted by the airflow resistivity σ (also called airflow resistance) in applications of the JCAL model once its value is directly obtainable from the static air pressure drop experiment. The relation between the two parameters is given by

$$k_0 = \frac{\eta_{\text{f}}}{\sigma}. \tag{2.26}$$

Finally, the last parameter shown in work by Johnson et al.(JOHNSON; KOPLIK; DASHEN, 1987) is the viscous characteristic length λ, related to the energy dissipation rate per volume at high frequency, where "$2/\lambda$ is essentially the surface-to-pore-volume ratio of the pore-solid interface in which each area or volume element is weighted according to the local value of the field u_p". Equation 2.27 shows the mathematical representation for this parameter, where u_p is the velocity of an inviscid fluid inside the pores.

$$\frac{2}{\lambda} = \frac{\int |u_p|^2 \mathrm{d}A}{\int |u_p|^2 \mathrm{d}V}. \tag{2.27}$$

2.3.2 Champoux and Allard's bulk modulus

Continuing the work by Johnson, Champoux e Allard (1991) points out the dependency of a fluid bulk modulus on its thermal behaviour and introduces an equation for the equivalent fluid bulk modulus. It is obtained through the high-frequency behaviour of the thermal skin depth (just as the viscous skin depth goes to very small dimensions and high frequencies), also using a newly define parameter λ' - the thermal characteristic length. It is defined as

$$\lambda' = 2\frac{\int_V \mathrm{d}V}{\int_A \mathrm{d}A}, \tag{2.28}$$

similarly to the viscous characteristic length, though now without weighting by the velocity inside pores and now representative of the volume-to-pore surface ratio. For irregular pores, the viscous and thermal characteristic lengths have different values. Additionally, the thermal characteristic length is always higher than the viscous (ATALLA; PANNETON, 2005).

The final equation for the bulk modulus proposed by Champoux & Allard is

$$K_{\mathrm{eq}}(\omega) = \gamma P_0 \left\{ \gamma \frac{\gamma - 1}{1 - j\frac{\phi\sigma}{\omega\rho_{\mathrm{f}}\alpha_\infty \mathrm{Pr}}\sqrt{1 + 4j\alpha_\infty^2\eta_{\mathrm{f}}\rho_{\mathrm{f}}\mathrm{Pr}\omega/\sigma^2\lambda'^2\phi^2}} \right\}^{-1}, \tag{2.29}$$

where Pr is the fluid's Prandtl number.

In possession of the equations necessary to obtain both the equivalent density and the equivalent bulk modulus specific to a porous material, it is then possible to obtain its characteristic impedance and wave number, having a full description of the material acoustic behaviour. Thus, these two contributions constitute the Johnson-Champoux-Allard (JCA) model.

2.3.3 Lafarge's correction

In an attempt to improve the description of thermal exchanges in saturating fluids, Lafarge et al. (1997) suggests the use of static thermal permeability k_0' as an additional parameter. To describe sound propagation through a porous material, a dynamic compressibility $\beta(\omega)$ is defined as a function of the dynamic thermal permeability $k'(\omega)$, correspondent to the viscous permeability $k(\omega)$ presented in Eq. 2.20. As so, it is represented as

$$\phi\tau = \frac{k'(\omega)}{\kappa}\frac{\partial}{\partial t}p, \tag{2.30}$$

where τ is the macroscopic excess temperature in saturating fluid, and κ its heat conductivity.

Analogous to viscous permeability, a more thorough description of low-frequency limit behaviour in Eq. 2.30 is available by using a thermal low-frequency parameter. To obtain it, the principle is equivalent to static viscous permeability: for very low frequencies,

the $\lim_{\omega \to 0} k'(\omega) = k'_0$ - hence the static thermal permeability k'_0. Like those previously shown, this parameter is dependent only on pore geometry and not on fluid properties.

With the newly defined parameter, a detailed behaviour of the equivalent bulk modulus is available. The dynamic compressibility $\beta(\omega)$ is related to the equivalent bulk modulus by $K_{\text{eq}} = K_{\text{a}}/(\beta(\omega))$, and it is defined as

$$\beta(\omega) = \gamma - (\gamma - 1)/\alpha'(\omega), \tag{2.31}$$

where α' is the thermal analogous to the dynamic tortuosity $\alpha(\omega)$ (ALLARD; ATALLA, 2009; ZIELIńSKI, 2015) and is represented by :

$$\alpha' = 1 + \frac{\nu'\phi}{j\omega k'_0}\sqrt{1 + \frac{j\omega}{\nu'}\left(\frac{2k'_0}{\lambda'\phi}\right)^2}, \tag{2.32}$$

where ν' is given by ν_f/Pr.

With the parameters presented so far, it is possible to reconstruct the JCAL model. Combining Eqs. 2.31, 2.32 and 2.21 to obtain equivalent density and bulk modulus, both final functions of sound frequency ω, are given as

$$\rho_{\text{eq}}(\omega) = \rho_{\text{f}}\left[\alpha_\infty + \frac{\nu_f\phi}{j\omega k_0}\sqrt{1 + j\frac{\omega}{\nu_f}\left(\frac{2\alpha_\infty k_0}{\phi\Lambda}\right)^2}\right], \tag{2.33}$$

$$K_{\text{eq}}(\omega) = \gamma P_0\left\{\gamma - \frac{\gamma - 1}{1 + \frac{\phi\nu'_f}{j\omega k'_0}\sqrt{\frac{j\omega}{\nu'_f}\left(\frac{2k'_0}{\Lambda'\phi}\right)^2 + 1}}\right\}^{-1}. \tag{2.34}$$

2.4 Direct Parameter Measurement

All semi-phenomenological and empirical models are dependent on different microstructure-related parameters. In total, the JCAL model requires six, while Delaney-Bazley, needs one. These parameters are referent to the average properties of a material, reflecting its bulk and not necessarily specific local geometries. Therefore, the tests necessary to evaluate such properties are conducted on large samples taken from the material of interest, searching for the most representative average properties. Different tests may simultaneously obtain results for more than one parameter, though other parameters require specific tests. In the present study, only porosity measurement tests were available to the authors - Archimedes's principle, the main method used in the present study is better detailed in Sec. 3.3.

2.4.1 Porosity

Besides the main Archimedes principle-based method presented in Sec. 3.3, some others have been proposed to evaluate porosity using different principles. One of the

earliest procedures reported by acousticians was that presented in Beranek (1942), with later suggested improvements by Champoux, Stinson e Daigle (1991) and Leclaire et al. (2003), that uses a sample holder connected to a U tube manometer. By enclosing a porous material sample with known total volume inside the holder, closing and pressurizing it, and evaluating the height/volume change at the manometer, it is possible to determine the sample open pore volume and thus the total open porosity using Boyle's law. Salissou e Panneton (2007) presented a method also based on Boyle's law, but with no U-tube manometers. Instead, four mass measurements are done on a closed vessel with know volume. Two are done with the "empty" vessel, and another with the sample held inside. Each of these is done either with high pressure or under a vacuum. Using the four measurements and knowledge of the sample's total volume, it is possible to determine its solid phase volume using the pressure-volume relations from Boyle's law.

Another interesting option also reliant on Archimedes principle is the "missing mass" method, presented by Panneton e Gros (2005). It measures a sample's mass under a vacuum and in a normal atmosphere. Knowing air's density ρ_{f} and the total sample volume V_t, the mass under vacuum m', in atmosphere m and porosity are related by

$$\phi = 1 - \frac{(m - m')}{\rho_{\mathrm{f}} V_t}. \tag{2.35}$$

Although the balance precision has to be high to detect the small mass variation from the vacuum condition, and very low pressure needs to be achieved to assure the precision of the buoyancy condition, it is a simple method compared to those presented previously.

2.4.2 Static viscous permeability

As mentioned, the static viscous permeability is related to the airflow resistivity by Eq. 2.26. This parameter has long been obtained due to its simplicity in concept and evaluation, also showing direct relation to sound absorption performance by researchers since early studies (DELANY; BAZLEY, 1970; BERANEK, 1947).

Focusing on the flow resistivity of a sample, Cox e D'Antonio (2016) defines it as the ease of flow through the sample and resistance to this flow presented by the material. For a sample with height h subject to a steady flow with velocity U and pressure drop of ΔP after passage through the sample, the resistivity is given by

$$\sigma = \frac{\Delta P}{Uh}. \tag{2.36}$$

Airflow resistivity, as shown in Eq. 2.36, is written as a function of material layer thickness, allowing its use as an intensive property, assuming it is a homogeneous material. Airflow resistance is the measure specific to a sample, shown in Eq. 2.37. Resistance σ_s is

measured in unit of N s/m^3 and thus resistivity σ unit is N s/m^4.

$$\sigma_s = \frac{\Delta P}{U} = \sigma h. \tag{2.37}$$

Two main standards offer instructions on methods of airflow resistance measurements: ISO 9053-1/ISO 9053-2 (INTERNATIONAL ORGANIZATION FOR STANDARDIZATION, 2018; INTERNATIONAL ORGANIZATION FOR STANDARDIZATION, 2020) and ASTM C522 (ASTM INTERNATIONAL, 2016). These explain the evaluated properties, suggesting test setups and good practices associated with testing. All pass to the same testing principle with slight test method and apparatus variations. Basic components may be defined as

- An airflow source, either negative or positive pressure, able to produce a steady velocity flow;
- Flowmeters to evaluate volume velocity of airflow during testing;
- Differential manometers to detect the pressure drop from flow through the sample;
- An appropriate sample holder with measuring devices to report sample height in the testing position.

Figure 2.3 shows the basic organisation expected from a testing apparatus for airflow resistivity. It is worth noting that ISO 9053-2 presents slightly different testing, where instead of static flow, the evaluation is done on an alternating flow with controlled frequency - the measured properties remain the same, though (INTERNATIONAL ORGANIZATION FOR STANDARDIZATION, 2020).

2.4.3 Tortuosity

The earliest methods of tortuosity measurement were based on the saturation of the material of interest with a conductive fluid and further evaluation of its electrical resistance. This method, proposed by Brown (1980), depends on previous knowledge of material porosity and gives the tortuosity value as

$$\alpha_\infty = \phi \frac{r_s}{r_f}, \tag{2.38}$$

where r_s and r_f are the electrical resistivities of the material saturated by conducting fluid and the fluid, respectively.

Another method proposed by Johnson et al. (1982) involves saturating the sample with superfluid helium. At temperatures below T = 2, 17 K, ^{4}He goes through a phase transition and becomes He II (Helium 2), a "superfluid" phase at which it has no measurable viscosity, and its bulk modulus is much smaller than that of most solids, allowing the rigid

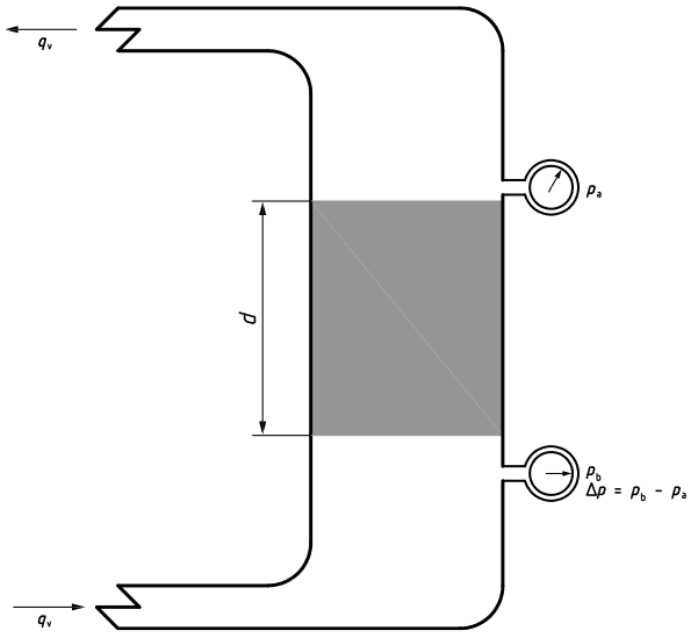

Figure 2.3 – Basic organisation of the flow resistivity apparatus (INTERNATIONAL ORGANIZATION FOR STANDARDIZATION, 2018).

structure approximation for a large range of materials (JOHNSON; KOPLIK; DASHEN, 1987) (THUNEBERG, 2005). These two conditions permit the measurement of a high-frequency limit of tortuosity using acoustic measurements of slow wave velocity V_{slow}, due to the fourth sound phenomena (JOHNSON, 1980), represented in Eq. 2.39, that reveals a simple relation between slow wave velocity, speed of sound in the fluid and tortuosity.

$$V_{\text{slow}} = (K_f/\alpha\rho_{\text{f}})^{\frac{1}{2}} = V_f/\sqrt{\alpha_\infty}, \tag{2.39}$$

where V_f is the speed of sound in the superfluid. The main problem with this approach is the difficulty accessing the equipment necessary for using the superfluid.

2.4.4 Ultrasound techniques

There are a few reports in the literature describing ultrasound-based methods, relying on measurement of mainly fluid phase speeds in ultrasound frequencies (JAOUEN, 2021), to find the high-frequency limit of tortuosity α_∞, and both characteristic lengths λ,λ'. A representation of the basic apparatus necessary to perform these ultrasound measurements is presented in Fig. 2.4.

The first reported method, presented in Allard et al. (1994), requires measurements for the free fluid and when it is saturating a sample. For this method, the author points out that the principle behind it is equivalent to that of the aforementioned superfluid method. In Leclaire et al. (1996), measurements of sound phase velocity and attenuation are performed to obtain parameter values, using the variation of phase and amplitude of ultrasound evaluated for samples with different heights. As for Leclaire et al. (1996), helium and air are used to obtain different curves of acoustic properties (propagation index

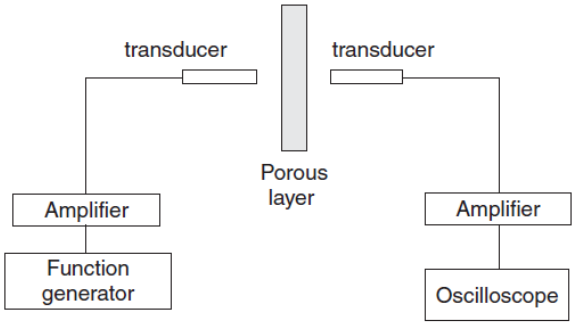

Figure 2.4 – Representation of the testing setup for ultrasound measurements (ALLARD; ATALLA, 2009).

and the product of the quality factor and the viscous skin depth) of porous materials and, taking advantage of the linear dependence on controlled variables and asymptotic behaviour of these properties, find all the parameters.

All these methods are derived from the complex wave number equation, shown in Eq. 2.40, for very high-frequency behavior, as discussed in Lafarge et al. (1993)

$$k = \frac{\omega}{c}\sqrt{\alpha_\infty}\left[1 + \delta\frac{(1-j)}{2}\left(\frac{1}{\lambda} + \frac{\gamma - 1}{\mathrm{Pr}\lambda'}\right)\right], \tag{2.40}$$

where c is the fluid sound speed.

These methods have shown good results for highly porous and smooth materials. Reports show that low porosity materials with rough pores form an overly dissipative medium for ultrasound propagation, hampering any methods based on ultrasound (BOTTERMAN et al., 2016; ATALLA; PANNETON, 2005).

2.4.5 Static thermal permeability and bulk modulus based methods

From direct equivalent dynamic bulk modulus and density measurements, it is possible to find approximate values for different parameters based on the known behaviour of both these dynamic properties for certain frequency ranges, including the static thermal permeability, which has no other direct measurement routes. These methods have been named analytical methods in some reports (BONFIGLIO; POMPOLI, 2013; NISKANEN et al., 2017) due to the use of analytical relations to reach parameter values.

Tarnow (1995) presents a tube configuration to evaluate compressibility (related to bulk modulus, as mentioned in Sec. 2.3.3), positioning the microphone away from the loudspeaker at a quarter of the resonance frequency wavelength, where the pressure is minimal. This method is mentioned in Lafarge et al. (1997), and its experimental results are compared with predicted behaviour using the model based on static thermal permeability.

Another means of obtaining the dynamic bulk modulus is impedance tube testing, as presented in Panneton e Olny (2006) and Olny e Panneton (2008). Both these works show

the viability of parameter extraction from bulk modulus and density measurements using the known relation between parameters and acoustic properties. In the proposed techniques, not all parameters are extracted, requiring previous knowledge of other parameters, such as open porosity. It has been shown by Jaouen, Gourdon e Glé (2020) that all six parameters of the JCAL model are obtainable from impedance tube measurements of the bulk modulus (e.g. two microphones impedance tube with multiple sample thicknessess method (SMITH; PARROTT, 1983), two microphones with two cavity depths (UTSUNO et al., 1989), apud (JAOUEN; GOURDON; GLé, 2020)). In the same manner as the previous works, from K_{eq} and ρ_{eq}, the parameters are obtained out of relations between these equivalent properties, known/controlled fluid properties, and the parameters through semi-phenomenological models. These known relations also show asymptotic behaviours that enable a parameter estimation for certain frequency ranges. They also show that many different methods to obtain K_{eq} and ρ_{eq} are available in literature using different impedance tube configurations and sample positioning variations. Besides necessary equipment, some drawbacks of these estimations are the need for clear asymptotic behaviour represented in data on the results and also the dependence all other parameter estimations have on porosity and static flow resistivity estimations (the equations necessary to obtain the other parameters are still dependent on previous knowledge of these two).

2.4.6 Model calibration methods

One final method commonly used to evaluate all parameters of the JCAL model is the model calibration (inverse characterization (ATALLA; PANNETON, 2005)) option. It consists of fitting the model to any sample's experimentally measured impedance curves using a nonlinear problem solver to minimise cost function between numerical and experimental values. It will be later subjected to an in-depth description in Chapter 4.

2.5 Multilayer systems

Another numerically studied aspect of sound propagation through porous media in the present work was the absorption of multilayered systems. These are interesting solutions for the design of sound absorbers since combining different absorber materials may result in better absorption performance compared to a simple material layer with the same thickness as the combined materials (COX; D'ANTONIO, 2016). Modelling these systems is made simple by the use of the Transfer Matrix Method (TMM), well described in Allard e Atalla (2009) and Bruneau e Potel (2009).

Sound propagation modelling will depend on the assumed layer type for a multilayer system with n layers, as illustrated in Fig. 2.5. As an example, for poroelastic layers it is necessary to describe the three waves predicted by Biot's model propagating through the fluid and solid parts of that layer using the velocity and stress components of both these

media. Only fluid layers will be analysed in this work since the materials studied here are modelled under the rigid material assumption. An equivalent fluid layer describes sound propagation through a porous material layer. This description only needs two fluid flow properties, pressure and velocity, at each point specified adjacent to the borders of a given layer. In turn, for two different points, these two properties are related by the relation

$$\mathrm{V}(M_n) = [T]\mathrm{V}(M_{n+1}), \tag{2.41}$$

where $\mathrm{V}(M_n)$ is the fluid flow property vector at point M_n, T is the transfer matrix between these two points. Considering the fluid velocity component $v_3^f(M_n)$ perpendicular to the layers and fluid pressure $p(M_n)$, both at a point M_n, the $V(M_n)$ vector is given by

$$V(M_n) = [p(M_n) \qquad v_3^f(M_n)]^{\mathrm{T}}. \tag{2.42}$$

It is necessary to use sound propagation equations to obtain the matrix T relating the properties at each point M_n. Considering the one-dimensional propagation of sound in the x_3 direction, the pressure equation may is given by

$$p(x_3, t) = [A_1 e^{(-jk_3x_3)} + A_2 e^{(jk_3x_3)}]e^{(j\omega t)}, \tag{2.43}$$

where k_3 is the wave number of the propagating wave, ω is the frequency, and A_1,A_2 are the waves' amplitudes related to the negative and positive going elements of the propagating wave. Similarly, the fluid velocity is described by

$$v_3^f(x_3) = \frac{k_3}{\omega\rho_{\mathrm{f}}}[A_1 e^{(-jk_3x_3)} - A_2 e^{(jk_3x_3)}]e^{(j\omega t)}. \tag{2.44}$$

Considering a steady state sound response, the time-dependent part of Eqs. 2.43 and 2.44 may be ignored. Referent to Fig. 2.5, one may obtain the relations of two adjacent points, say M_1 and M_2, by defining the position of M_2 to be $x_3(M_2) = 0$ and of its adjacent point $x_3(M_1) = h$. At M_1, the pressure and velocities are defined by

$$p(M_2) = A_1 + A_2; \tag{2.45}$$

$$v_3^f = \frac{k_3}{\omega\rho_{\mathrm{f}}}(A_1 - A_2). \tag{2.46}$$

Hence, to achieve the relation of Eq. 2.42, Eqs.2.43, and 2.44 are applied to the point M_1 (at position $x_3 = h$). Using Euler's formula applied to Eqs. 2.43 and 2.44, the transfer matrix $[T]$ is thus given by

$$[T] = \begin{bmatrix} \cos(k_3h) & j\frac{\omega\rho_{\mathrm{f}}}{k_3}\sin(k_3h) \\ j\frac{k_3}{\omega\rho_{\mathrm{f}}}\sin(k_3h) & \cos(k_3h) \end{bmatrix} \tag{2.47}$$

Thus, the transfer matrix is defined as the interface between adjacent points at the borders of the same layer. It is necessary to evaluate the global transfer matrix, which

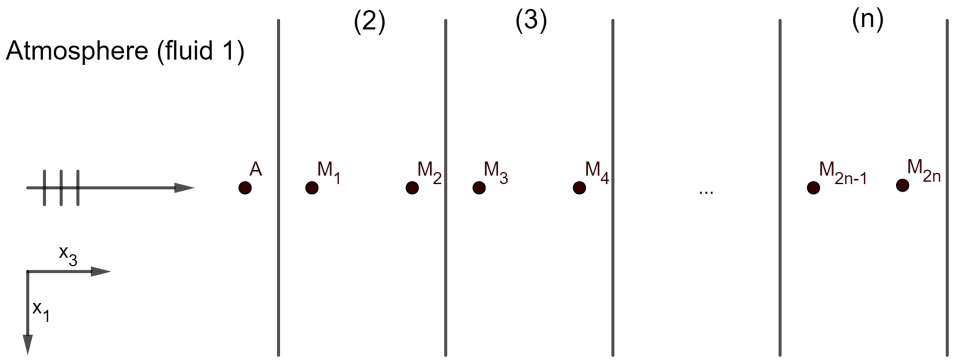

Figure 2.5 – Representation of a multilayer system (adapted from Allard e Atalla (2009)).

describes the whole multilayer system. For systems composed of layers of the same nature (fluid, solid, poroelastic, etc.), the transfer matrix is simply composed of the multiplication of individual transfer matrices. The presented modelling only applies to systems composed solely of fluid layers, however, this rule should be applied. Nevertheless, as these "fluid" layers represent porous materials, it is necessary to consider the continuity equations between two different porosity media. Take the interface between points M_2 and M_3 in Fig. 2.5, which connect the layers with porosity ϕ_1 and ϕ_2, respectively. The continuity relations there are given by

$$\begin{aligned} p(M_2) &= p(M_3), \\ \phi_1 v_3^f(M_2) &= \phi_2 v_3^f(M_3). \end{aligned} \tag{2.48}$$

Given these conditions, one may build a matrix that relates the vector V at the two interfaces. This matrix called "I_{pp}" is shown in Eq. 2.49. Besides the interfaces between equivalent fluid layers, this matrix will also be used for the interface between the first porous layer and the atmosphere fluid.

$$\mathrm{V}(M_2) = I_{12}\mathrm{V}(M_1), \qquad I_{12} = \begin{bmatrix} 1 & 0 \\ 0 & \frac{\phi_2}{\phi_1} \end{bmatrix}. \tag{2.49}$$

Now that the relations between layers are determined, following a similar procedure to that presented in Allard e Atalla (2009), they may be written in as a matrix equation. For this, Eq. 2.50 relating the atmosphere fluid to the first layer using the interface matrix $I + f1$, and Eq. 2.51 relating the following layers, are used.

$$[I_{f1}]\mathrm{V}(A) - [T^{(1)}]V(M_2) = 0, \tag{2.50}$$

$$[I_{(k)(k+1)}]\mathrm{V}(M_{2k}) - [T^{(k+1)}]V(M_{2(k+1)}) = 0, \quad k = 1, ..., n-1. \tag{2.51}$$

From these equations, we aim at obtaining the matrix equation $[D][\mathrm{V}_0] = 0$, where the matrix $[D]$, containing information of each layer and its interfaces, must be associated with the vector V_0 descriptive of all the system's fluid flow properties. A matrix $[D_0]$ is

defined as

$$[D_0] = \begin{bmatrix} [I_{f1}] & -[T^{(1)}] & [0] & \cdots & [0] & [0] \\ [0] & [I_{12}] & -[T^{(2)}] & \cdots & [0] & [0] \\ \vdots & \vdots & \vdots & \ddots & \vdots & \vdots \\ [0] & [0] & [0] & \cdots & -[T^{(k-1)}] & [0] \\ [0] & [0] & [0] & \cdots & [I_{(n-1)(n)}] & -[T^{(n)}] \end{bmatrix}, \tag{2.52}$$

$$\mathrm{V}_0 = \begin{bmatrix} \mathrm{V}(A) & \mathrm{V}(M_2) & \mathrm{V}(M_4) & \cdots & \mathrm{V}(M_{2n-2}) & \mathrm{V}(M_{2n}) \end{bmatrix}^{\mathrm{T}}. \tag{2.53}$$

Looking at Eq. 2.42, it can be noted that the vector V_0 will have, in the present case, $2n + 2$ elements, two for each layer plus two for the atmosphere layer. Matrix $[D)]$ though will have only $2 * n$. With this lacking information, the system is filled with boundary conditions, namely the impedance relations at the open surface and the material termination.

The hard wall termination condition is at the rigid border, so the pressure is that of the point adjacent to it, and the velocity of the fluid is zero. This condition may be defined in the same way as the other layer points, using the vector $Y^{(n)}$ as shown by

$$[Y^{(n)}]\mathrm{V}(M_{2n}) = 0, \quad [Y^{(n)}] = [0 \quad 1]. \tag{2.54}$$

This information can be added to the $[D_0]$ matrix, as

$$[\mathrm{D}] = \left[\begin{array}{c} [D_0] \\ \hline [0] \quad \cdots \quad [Y^{(n)}] \end{array}\right]. \tag{2.55}$$

Finally, the last equation to be added to this system is the surface impedance Z_s at the first layer. As presented in Eq. 2.15, the surface impedance relates pressure and velocity at a point, i.e. $Z_s = p(A)/v_3^f(A)$. Thus, this relation may be defined as

$$[-1 \quad Z_s]\mathrm{V}(A) = 0. \tag{2.56}$$

As in the case of the hard wall termination condition, the relation presented in Eq. 2.56 is used to define the matrix [D], is presented as

$$[\mathrm{D}] = \left[\begin{array}{ccccc} -1 & Z_s & [0] & \cdots & [0] \\ \hline & & [\mathrm{D}] & & \end{array}\right]. \tag{2.57}$$

Now matrix [D] is square, and the system is fully determined, meaning that $[\mathrm{D}]\mathrm{V}_0 = 0$. As pointed out by Allard e Atalla (2009), the impedance may be obtained from

$$Z_s = -\frac{[D_1]}{[D_2]}, \tag{2.58}$$

where $[D_1]$ is the matrix obtained when the first column of the matrix $[D]$ as presented in Eq. 2.55, and $[D_2]$ is that obtained performing the same procedure for the second column.

3 Ceramics

In the present study, the acoustic properties of porous ceramics are studied. The present chapter is dedicated to presenting the main details related to the material element of the conducted research, discussing the freeze-casting fabrication route and its main aspects, the Al_2O_3/MgO system, and Archimedes principle testing.

3.1 Freeze-casting procedure

Freeze-casting has been researched as a means to achieve porous ceramics with a wide range of properties relating to microstructure. These successful uses of the technique on ceramics allow it to be an attractive choice for different applications such as filtration (FUKASAWA; ANDO; OHJI, 2002; SOFIE, 2007), bioactive structures (QIN; PARISI; FERNANDES, 2021), and even piezoelectric transducers (RYMANSAIB et al., 2022). The vast literature available on the process offers well-defined relations between process parameters and final ceramic properties. Thus to obtain the desired set of microstructural properties optimal for each of these applications, the parameters of each freeze-casting process step are adjusted.

The fabrication route may be divided into four main steps: slurry/suspension preparation, freezing (solidification of solvent), drying (sublimation of solvent), and sintering (firing). Briefly, the process consists of pouring the prepared slurry on a mold and freezing it. During freezing, solid crystals (dendrites) will nucleate in the slurry liquid phase and push away the ceramic particles, creating two different solid phases, the frozen solvent and the concentrated ceramic particles (lamellae). The frozen slurry is then freeze-dried, obtaining a green body (also called a powder compact in other ceramic applications). The solidified liquid acts as a "negative replica" (CHEN et al., 2021), leaving behind the green body porous channels once it is dried. After freeze-drying, the green body goes through sintering to improve its mechanical resistance, achieving the final produced sample. A graphic representation of the four steps is shown in Fig. 3.1. These four steps' main aspects and some intricacies are discussed to achieve a thorough appreciation of the method.

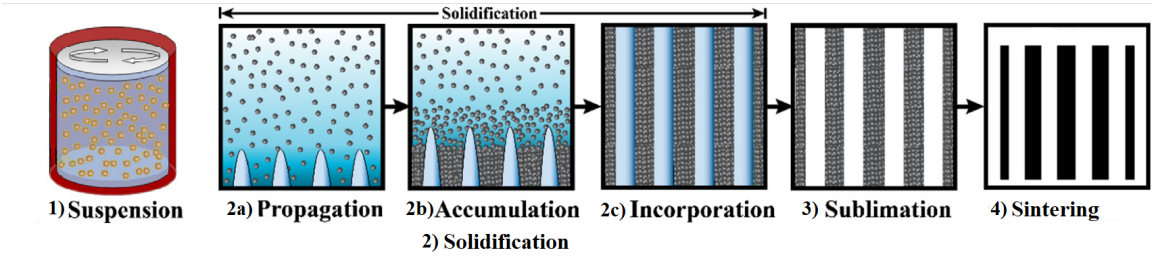

Figure 3.1 – Graphic representation of the freeze-casting steps (adapted from (SCOTTI; DUNAND, 2018) and (ZHANG; ZHAO; HONG, 2015)).

3.1.1 Slurry-suspension preparation

Preparing the slurry, also called suspension, is the beginning of the process. This step is common to plastic forming methods, such as extrusion and slip casting, so its principles and associated practices are often shared between the two processing categories. It consists of the dispersion of ceramic raw powders in a liquid (solvent), aiming at a homogeneously dispersed suspension of the powders to ensure a later homogeneous structure. Its most defining aspect concerning freeze-casting is the proportion between solid and liquid (solid loading). The amount of each component is directly related to the final obtained porosity (KOH et al., 2006; ARAúJO et al., 2018) since more solvent will result in more frozen crystals (consequently higher porosity) and vice-versa. Three main component categories are used in this stage: raw powders, solvents, and additives.

3.1.1.1 Starting powders

The choice of raw powders will depend on the inherent material properties, and whether it is fitting to the intended use, e.g. hydroxyapatite for bone-tissue engineering solutions (DEVILLE; SAIZ; TOMSIA, 2006; FU et al., 2008; MACCHETTA; TURNER; BOWEN, 2009a). Likewise, in conventional ceramic processing methods, some aspects of the starting powders will significantly influence the final sample's microstructure. Particle size distribution, shape, chemical/phase composition, and impurities may all affect processing steps and produce different final characteristics. Some of these issues are discussed in the following steps.

3.1.1.2 Additives

In freeze-casting, the homogeneity of solid particle suspension is of paramount importance to avoid process-specific phenomena like particle entrapment and unwanted density/porosity gradients through the sample‘s dimensions or general ceramic processing problems such as particle agglomerates in the green body. This issue is mainly tackled by using additives, which may be broadly refered to as dispersants. These act by adsorbing to the surfaces of the ceramic particles, creating electrically charged layers (ionic dispersants)

around them and consequently repealing forces between particles. Another possibility is the absorption of organic chains with functional head groups (nonionic surfactants) to the surfaces, once again creating repulsion, though now steric. Independent of the type, these additives stabilise the suspension, preventing undesired phenomena such as settling or flocculation, and help reach lower viscosity in spite of the solid loading (RAHAMAN, 2017), playing a major role in keeping the slurry from becoming too viscous ("thick") before pouring it into a mold.

Another type of additive is binders. After drying the sample, the formed green-body will be mostly constituted by loosely joined agglomerates of ceramic powder with little to no mechanical resistance and structural support. Organic binders can join the particles and improve the green body strength after drying and preventing structural damage before reaching the sintering phase (DEVILLE, 2008). These organic binders have a degradation temperature much lower than those needed for sintering and are normally burned during (or before) the sintering phase. Finally, it is important to mention that both binders and dispersants have been shown to greatly influence the final microstructure of produced porous ceramics (LI; LU; WALZ, 2012).

3.1.1.3 Slurry mixing

All additives, solvents, and ceramic powders must be well mixed to obtain a stable suspension appropriate for the following steps. This mixing can be conducted through different methods such as ball milling (ARAKI; HALLORAN, 2004) (which will also promote finer particle size distribution and possibly mechanochemical synthesis (RAHAMAN, 2017)) or magnetic stirring (ARAúJO et al., 2018). The main concern here is to promote proper dispersion of all components, so mixing times may be longer than 20 hours (ZHANG; ZHAO; HONG, 2015), although some achieve good results within a few hours (ARAKI; HALLORAN, 2004). Another concern is the formation and entrapment of air bubbles during mixing, which incurs the formation of non-connected pores. Some approaches are available, such as mixing under vacuum (DEVILLE; SAIZ; TOMSIA, 2007).

3.1.2 Slurry freezing

The freezing step is the route's most characteristic stage and is responsible for the most differentiating outcomes related to other methods. The frozen solvent action determines its influence on a final material structure as a template. Hence, the resultant characteristics of solvent crystal growth (mainly shape, size, and alignment) define the material porosity characteristics. These growth characteristics, in turn, are related to the freezing parameters.

Nevertheless, mediating the wanted final results and the obtained crystal structure

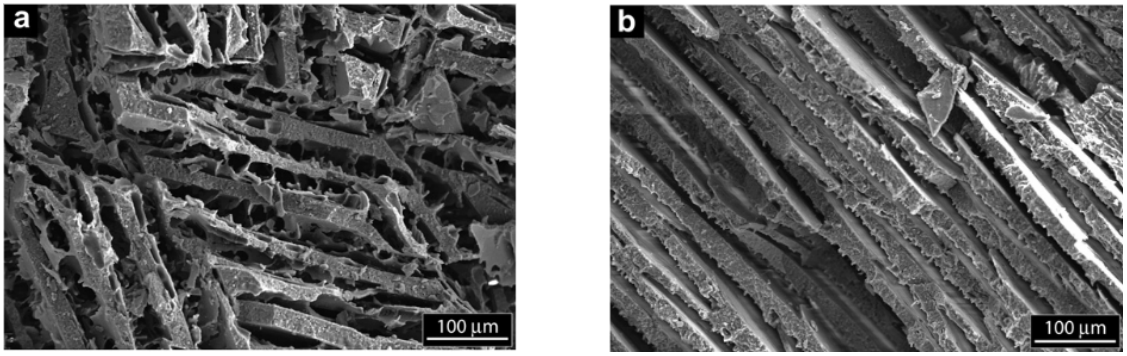

(a) (b)

Figure 3.2 – Ice templated structures obtained with isotropic (a) and anisotropic (b) cooling (DEVILLE; SAIZ; TOMSIA, 2007).

is the mobile interface between growing dendrites, the liquid suspension and concentrated solid regions, called the freezing front. Although solute redistribution by freezing is a well-known phenomenon (UHLMANN; CHALMERS; JACKSON, 1964), the forces governing the interaction in the interface are not well understood and remain subject to research (SCOTTI; DUNAND, 2018). Still, there is a good understanding of the consequences of different front velocities on the formed pore channels and their governing parameters (SHAO et al., 2020). Thus, good control of properties related to that front velocity is attainable.

Freezing direction

An important factor for applications such as acoustics and filtration, pore alignment is related to the cooling gradient direction applied to the poured slurry. The freezing front will start from the cold surface interacting with the slurry, and advance into its bulk, following the cooling gradient. Therefore, the cooling is often divided into isotropic and anisotropic. When the mold containing the liquid slurry is placed in a surrounding cold environment with no specific preferred cooling direction (e.g. a freezer), it is said to be isotropic. Anisotropic cooling will have one or more preferred cooling directions.

Unidirectional freezing, for example, is an anisotropic gradient achieved by placing the slurry-containing mold on top of a cold surface. The resulting geometry is aligned pores following the direction perpendicular to the plate plane, as shown in Fig. 3.2b. Contrasting to these aligned pores, Fig. 3.2a shows the microstructure of a sample subjected to anisotropic cooling, resulting in pores with varying alignments. Many other anisotropic cooling strategies have been proposed, such as radial (TANG et al., 2014; SU; MOK; MCKITTRICK, 2019), bidirectional (BAI et al., 2015), and even using electrical fields (CHENG; ZHAO; WU, 2015). Each of these will generate different pore structures that follow the cooling pattern.

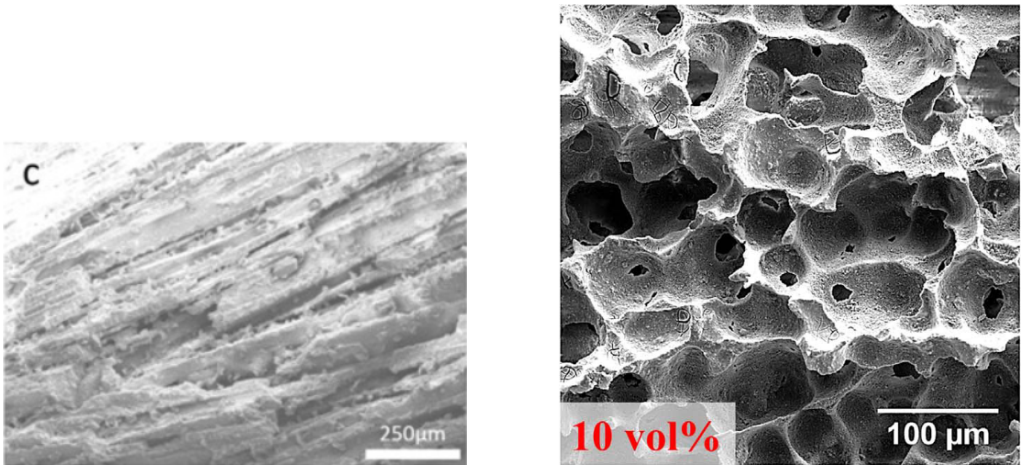

(a) (DONG et al., 2016) (b) (ARAúJO et al., 2018)

Figure 3.3 – Different pore shapes obtained using TBA (a) and camphene (b), respectively.

3.1.2.1 Solvent crystal shape

Different solvents will have varying crystal shapes when solidifying. Once again, as the formed pore channels are replicas of the grown crystals, they will have the crystal shape. Each one will form differently shaped crystals due to the reorganization of its molecules into the solid phase crystals and consequently generate channels with different shapes (DEVILLE, 2008). Some common solvents that generated structures of lamellar pores are water, camphene with dendritic pores, and Tert-Butyl-Alcohol (TBA) with prismatic pores. Visual examples of structures obtained from distinct solvents are given in Fig. 3.3.

3.1.2.2 Freezing related issues

As one might expect, most of the challenges in freeze-casting processing are also related to the freezing step, and this is due to the complex nature of its working principle.

One of the main problems in the context of freeze-casting is the engulfment of particles by the freezing front. Instead of being pushed away by the front, solid particles are entrapped, and dense regions of ceramic material between lamellae arise. These may become simple structures connecting lamellae called bridges (note that bridge formation may have different causes other than engulfment (DEVILLE, 2008)t), but they may form dense regions that interrupt the connections between pores and form irregular zones (LI; LU; WALZ, 2012). Although engulfment may have different causes, one main parameter predictive of engulfment is freezing front velocity. It has been shown to govern not only partially the shape and alignment of the crystals but also the entrapment of solid particles (DEVILLE; SAIZ; TOMSIA, 2007; UHLMANN; CHALMERS; JACKSON, 1964; CORTE, 1962), and it has been shown to exist a critical freezing front velocity v_{cr} above which particle engulfment will take place. The extreme opposite of this situation is forming a planar ice front. For very low freezing front speeds, the formed ice front is planar, and the

solvent freezes pushing the solid content from it without forming lamellae. Few reports of this phenomenon are available, but it has been reported for water-ceramic slurries by Waschkies, Oberacker e Hoffmann (2009), who also traces a clear correlation between lamellae thickness and freezing front velocity.

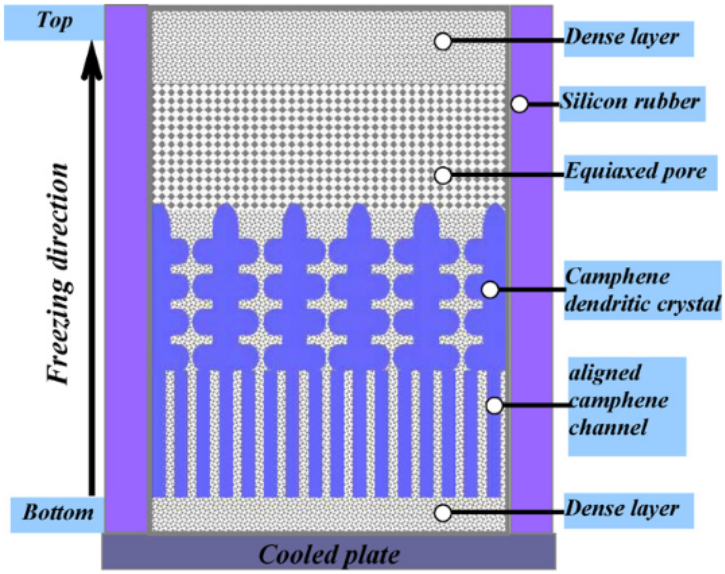

Figure 3.4 – Illustration of the different pore morphology regions created during slurry freezing (HONG et al., 2011).

Although not necessarily a problem, most likely a matter of concern to consider when working with freeze-casting is the porosity/pore morphology distribution throughout the sample dimensions, depending on the freezing direction. The complex thermodynamics of the slurry freezing process creates different freezing regimes inside a sample, frequently resulting in diverse pore structures. This phenomenon is better illustrated by Fig. 3.4. In their study, Hong et al. (2011) investigates the pore structure distribution through the sample height, using a camphene/Al_2O_3 slurry. The sample contains different porosity regions created by the varying cooling gradient. Near the cold plate, a high-temperature gradient is present. Thus the crystal growth is randomly oriented, and the freezing front speed is high enough to engulf most solid particles, creating a dense material region. As the solvent freezes and the freezing front goes farther away from the cold surfaces into the sample bulk, the temperature gradient is smaller, slowing the freezing front and forming a layer with pores aligned to the freezing direction. In this first layer of aligned pores, the still high-temperature gradient enables the nucleation of many crystals, creating straight pores with no dendritic branching allowed due to the pore density. Further ahead, another transition zone occurs from the aligned pores to aligned dendritic pores. This would occur due to the temperature gradient reaching a value low enough where not so many crystals nucleate, allowing the dendrites to grow fully. In Hong et al. (2011), another region on top of the full dendrites region with equiaxed pores formed due to freezing nucleating on the cooled mold wall, although studies with other solvents do not report zones alike (DEVILLE et al., 2009a; DEVILLE et al., 2009b). Finally, different dense layers also cover the bulk

surrounding regions: an open-top associated with a volatile solvent such as camphene will have high evaporation rates in the beginning, forming a slurry with higher solid loading in this regions, and the sample faces that contact the mold walls may have a diminished porosity due to the cooling of the mold that will create the same dense layer effect as that of the initial slurry contact with the cold plate.

This matter of pore structure variation through a given axis was thought not to be a matter of concern for the present study at first, as other studies showed this variation to be constrained to small dimension (≤ 1 mm) regions followed by homogeneous microstructure regions (DEVILLE; SAIZ; TOMSIA, 2007; HONG et al., 2011), and thus these regions with non-homogeneous properties were expected to be eliminated in polishing. As experimental studies advanced, though, such variation proved to be a non-negligible matter for our samples. This will be further discussed in Sec. 5.

3.1.3 Freeze-drying

The following step to freezing is the removal of solvent from the formed green body, which is done by freeze-drying, where the solidified solvent is removed by sublimation. This strategy allows the ceramic structure to be maintained during freezing, whereas any solvent removal that goes through melting would destroy the microstructure. For liquid solvents in ambient pressure and temperature, such as water and DMSO, the process needs to be conducted in very low temperatures and pressures (vacuum) to reach a range where the solvent sublimates. Other volatile solvents such as TBA and Camphene will sublimate in ambient temperature and environment, so it suffices to simply leave the sample resting (in an environment with good air circulation) for a certain amount of time so that the solvent evaporates.

The freeze-drying procedure is straightforward and is not usually mentioned as a focus in research since, generally, a poorly conducted freeze-drying will either destroy a sample or turn its microstructure defects into a non-reproducible one. Hence, a good drying specimen will allow the structure to be consolidated. One commonly mentioned aspect is the necessary time to completely dry the samples, varying around 20 hours (MACCHETTA; TURNER; BOWEN, 2009b; FUKASAWA; ANDO; OHJI, 2002; ARAKI; HALLORAN, 2004).

3.1.4 Sintering/firing

Nearly all ceramic processing techniques need to pass through a sintering phase, where the ceramic particles of the green body will consolidate, reducing the total free energy of the system. The sintering phase may be included the called firing phase. “Firing” refers to the whole heating phase, which may include other process such as additive (e.g. organic binders) burning, but also includes the sintering stage. Firing is a term commonly

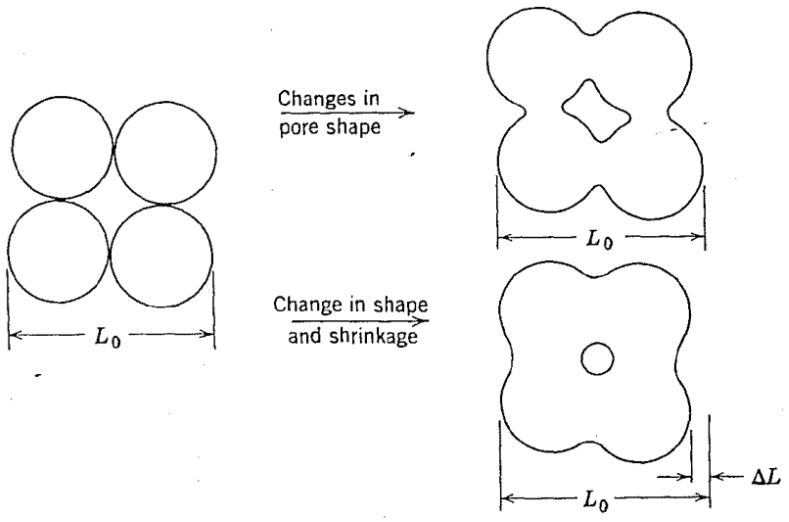

Figure 3.5 – Illustration of pore change in shape with and without densification (KINGERY; BOWEN; UHLMANN, 1976).

used in literature, so it is interesting to point out its existence and its differences regarding the sintering process.

During sintering, two complex atom diffusion processes are available to reduce particle surface free energy: coarsening and densification. The coarsening increases the average surface area of individual grains without filling pores between particles. At the same time, densification is the bonding of particles with the transport of matter into the void spaces between grains. Densification will result in shrinkage of the green body, producing a denser sample with reduced pore quantity and total volume (RAHAMAN, 2017). Even though it changes pore shape and, coarsening will not greatly affect the green body density or volume, opposite to the densification process, which also changes pore shape, but reduces pore volume. The possibility of change in pore shape with or without densification might be unintuitive and is better represented in Fig. 3.5. Both mechanisms will eventually create final samples mechanically stronger than the green body composed of simply compacted ceramic powders. However, denser samples will generally have greater strength. The parameters that control the prevalence of each sintering mechanism are well understood for most ceramic materials, and thus good control of final sample properties can be obtained.

Some approaches are available to the sintering process, but the two most commonly employed can be named: liquid-phased sintering and solid-state sintering. Liquid-phase sintering uses an additive that will melt during sintering, providing a liquid phase to enhance diffusivity of matter into pores. In contrast, solid-state sintering is carried out by heating the green body to a temperature around 50-80 % of the starting powder melting point for a given amount of time, promoting sintering through atomic diffusion (RAHAMAN; FU, 2008).

In the context of freeze-casting, little discussion on sintering is reported. A common practice described during firing stage is having temperature plateaus well below sintering

temperatures during heating, to remove any remaining substances from the slurry, such as binders and dispersants, that were not removed in freeze-drying, though little comment is made about sintering. Another important aspect is the control of densification of the structure since the main goal for freeze-cast ceramics is the production of controlled porosity samples, and elevated densification of samples will result in greater shrinkage of the ceramic as a whole, affecting pore size, a property of interest for many freeze-casting applications. Fukasawa et al. (2001) show that higher sintering temperatures can make small pores coalesce and cease to exist, affecting pore size distribution. Control of densification is mainly done by control of sintering time and temperature.

3.2 Al_2O_3/MgO/Spinel system

Al_2O_3 (alumina) and MgO (magnesia, or periclase for the mineral) are important ceramic materials with diverse applications. Alumina is commonly castable but also used for electronic products as an insulator and an overall good material for applications demanding high mechanical resistance at high temperatures (SURENDRANATHAN, 2020). Magnesia is also a refractory material, with a very high melting point of 2800° Celsius for its dead burned form (SHAND, 2006).

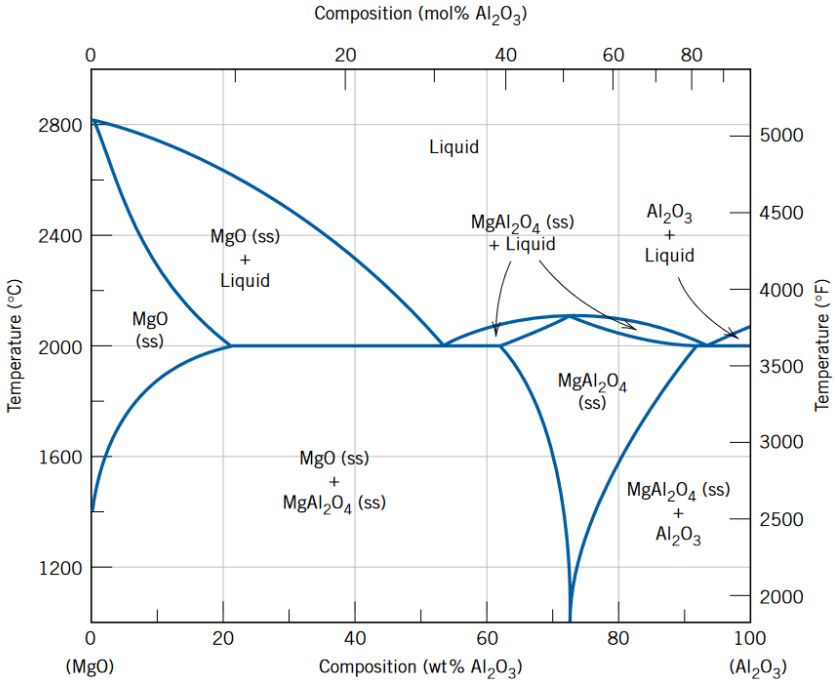

Figure 3.6 – Al_2O_3/MgO phase diagram (CALLISTER; RETHWISCH, 2020).

The two ceramics may also be combined, either for doping (BERRY; HARMER, 1986) or fully mixed in higher proportions as multi-phase (solid solution) ceramic materials. Figure 3.6 shows the phase diagram for the two materials. It can be seen that three well-divided main regions will be formed for different proportions of each ceramic: spinel-rich magnesia, spinel-rich alumina, and pure spinel. The spinel phase, also known as magnesium

aluminate, is a stable phase originating at the solid solution at molar stoichiometry (in weight, the proportion is 71.67 wt % Al_2O_3 and 28.33 wt % MgO (BRAULIO et al., 2011))with various uses. However, with complex fabrication routes (GANESH, 2013). Each of these regions will have different processing and mechanical properties, depending on the proportion of each phase. This clear division in the phase diagram and expected easily detectable property differences motivated the selection of this system for studies in phase composition influence in ceramic sound absorption.

3.3 Archimedes Principle

In the present work, when referring to Archimedes principle porosity assessment, the reference is relative to the method described here, based on the buoyancy force predicted by the Archimedes principle. The method shown here is close to that suggested in ASTM C373-18 (ASTM INTERNATIONAL, 2018), and ASTM B962-15 (ASTM INTERNATIONAL, 2017). Porosity is the ratio between the total pore volume (closed, open or total) and the sample total (apparent) volume that comprises both pore and skeleton volume. To evaluate the open, closed and total porosity, three masses are necessary for the same sample: dry m_d, damp (saturated) m_s, and immerse m_i. The immerse mass m_i is obtained from immersing the sample in deionized water and measuring its mass while immersed (as shown in Fig. 3.7). After lightly removing excess water, the sample's mass is measured again, obtaining saturated mass m_s. Before these measurements are done, the dry sample mass m_d may be surveyed by measuring the sample mass in an open atmosphere while it is dry.

Figure 3.7 – The set-up used to measure immerse mass of a sample.

The equations behind the principle assume buoyancy forces exerted by the air on

the dry sample to be negligible. However, as are the air mass inside closed pores, the dry mass is related to the solid volume V_{solid} (the volume of a sample's skeleton) by

$$m_d = V_{\text{solid}}\rho_s, \tag{3.1}$$

where ρ_s is the density of the dense ceramic material. For the present case, where different phases compose the solid part of the porous ceramic, it is assumed that ρ_s has the value of the prevalent phase.

Assuming that water saturates the open pores in its entirety, the saturated mass m_d is related to open pore volume V_{open} by

$$m_s = m_d + \rho_{\text{H}_2\text{0}}V_{\text{open}}, \tag{3.2}$$

where $\rho_{\text{H}_2\text{0}}$ is water's density. Finally, assuming that the buoyancy partially counteracts the weight measured by immersing the sample, the measured immerse mass m_i is related to the solid volume V_{solid} and closed pore volume V_{closed} by

$$m_i = m_d - \rho_{\text{H}_2\text{0}}(V_{\text{solid}} + V_{\text{closed}}). \tag{3.3}$$

In possession of Eqs. 3.1, 3.2, 3.3, obtaining the equations for each volume is straightforward. The open pore volume is obtained from Eq. 3.2, reaching Eq. 3.4, while Eq. 3.5 for V_{solid} comes from Eq. 3.1.

$$V_{\text{open}} = \frac{m_s - m_d}{\rho_{\text{H}_2\text{0}}}. \tag{3.4}$$

$$V_{\text{solid}} = \frac{m_d}{\rho_s} \tag{3.5}$$

The apparent or total volume V_{total} also has a simple equation, though not as straightforward to reach as the other two volumes, as shown by

$$\begin{aligned} V_{\text{total}} &= \frac{m_s - m_i}{\rho_{\text{H}_2\text{0}}} \\ &= \frac{\{(m_d + \rho_{\text{H}_2\text{0}}V_{\text{open}}) - [m_d - \rho_{\text{H}_2\text{0}}(V_{\text{close}} + V_{\text{solid}})]\}}{\rho_{\text{H}_2\text{0}}} \\ &= V_{\text{open}} + V_{\text{close}} + V_{\text{solid}}. \end{aligned} \tag{3.6}$$

Equation 3.6 gives the closed pore volume by subtracting the volumes of Eqs. 3.4, 3.5. All porosities can then be evaluated using Eqs. 3.1 - 3.6 simply applying them to the porosities ration shown in

$$\phi_{\text{open}} = \frac{V_{\text{open}}}{V_{\text{total}}}, \quad \phi_{\text{close}} = \frac{V_{\text{close}}}{V_{\text{total}}}, \quad \phi_{\text{total}} = \frac{V_{\text{open}} + V_{\text{close}}}{V_{\text{total}}}. \tag{3.7}$$

4 Numerical Studies

4.1 Model calibration

The direct parameter measurement techniques for semi-phenomenological models are presented in Section 2.4. Another way to evaluate these material parameters is model calibration (inverse identification). It consists of the solution of a curve fitting (inverse) problem, where the goal is to fit the results given by an appropriately selected model (e.g. JCAL, Attenborough) to the experimentally obtained results.

Results obtained using this method have been reported for different materials, showing good fit to experimental curves and also close parameter values to parameters measured from other methods (ATALLA; PANNETON, 2005; SHRAVAGE; BONFIGLIO; POMPOLI, 2008; ZIELIńSKI, 2012; BONFIGLIO; POMPOLI, 2013). While many studies present single measurements of the surface impedance of material samples (that suffice in achieving good approximations), a common improvement suggested to this strategy is the use of various measurements varying some parameters of the experimental test setup. This practice provides additional data and thus a reduced uncertainty range in the measures and estimations (CUENCA et al., 2022). Some examples are varying size air gaps backing the sample in an impedance tube (ZIELIńSKI, 2015) and using two impedance tubes, one with an expansion chamber and another without (CUENCA et al., 2022).

One possible division between approaches is the numerical treatment of the fitting problem, as it may be deterministic or statistical. In deterministic methods, fitting is done by variation of the model parameters until an objective cost function is minimised to a desired level using optimisation techniques. Statistical methods are usually combined with deterministic ones, but they use methods such as Bayesian inference that take into account variability, and other statistical measurements of the found estimates and can give a more precise estimation, besides circumventing commonly found issues in deterministic methods such as local minima (CHAZOT; ZHANG; ANTONI, 2012; NISKANEN et al., 2017; CUENCA et al., 2022).

Inversion approaches have also been developed for determining the profiles of inhomogeneous materials, i.e. materials composed of layers with varying parameters (RYCK et al., 2008; RONCEN; FELLAH; OGAM, 2022; FACKLER; XIANG; HOROSHENKOV,

2018). This is a more complicated problem than measuring homogeneous materials due to the combination of different absorption behaviour inside a sample and space dependence of these parameters, so additional information is necessary. This is achieved by using different testing configurations, e.g., measuring surface impedance for different sound wave incidence angles (RYCK et al., 2008), similar to the proposed methods in homogeneous materials. For materials in which the rigid approximation applies to all layers, the problem may be simplified by using the transfer matrix method.

4.1.1 Tested numerical approaches

The strategy used in the present work to evaluate material parameters through model calibration was deterministic. The to-be-minimized cost function is presented by

$$R(\mathbf{a}) = \frac{1}{2}\sum_{\omega}\frac{1}{\sigma_{\text{er}}}|Z^{\text{exp}}(\omega) - Z(\omega,\mathbf{a})|^2, \tag{4.1}$$

where $Z^{\text{exp}}(\omega)$ is the obtained experimental sample surface impedance at frequency ω, $Z(\omega,\mathbf{a})$ is the obtained modelled surface impedance for the vector of model parameters $\mathbf{a}$ at the same frequency and σ_{er} is the standard deviation of the impedance's real and imaginary parts. Most deterministic methods are based on a cost function following this format, varying only sum over other experimental parameters and minor details.

The surface impedance models are non-linear functions of the frequency ω, this is a non-linear regression problem. Different numerical optimisation methods are available to solve this problem, many already implemented in commercial or open-source packages. These may be divided into constrained and unconstrained methods, where constrained will consider mathematical constraints among parameters and bounds for parameter minimum and maximum values, while unconstrained will reach function minima regardless of any previously defined limitation.

A few different approaches were tested. At first, the cost function was written in code, and a complex double variable vector, called Z_{exp}, containing the impedance generated from the JCAL function for a given set of parameters, was created. This generated impedance vector served as the curve to be fitted by whichever method was used. Depending on the results obtained from optimising the cost function with the raw vector, the noise was added to the raw impedance vector (using the "rand" function from MatLab), and optimisation was run again to check the robustness of the algorithm.

Two unconstrained methods were tested in greater depth. The "fminsearch" function available in MatLab (FMINSEARCH,), based on the Nelder-Mead optimization method (NELDER; MEAD, 1965), as it does not depend on objective function derivatives, since it is a direct search method. It is also the method used by Bonfiglio e Pompoli (2013). The other method, one of the most used unconstrained least square methods, the Levenberg-Marquardt method, is the resultant of the work by LEVENBERG (1944) and Marquardt (1963), being the most used approach for the present work. It presents an interpolation

between the Gauss-Newton method and the steepest descent method, better presented in Appendix A.

4.1.1.1 Nelder-Mead

A set of generated noisy data calibrated using the Nelder-Mead method is shown in Fig. 4.1. Noise was generated using the "rand" function from MatLab (MATHWORKS,). For all sets of impedance values shown, values between 0 and 100 were generated using the "rand" function and added to both the real and imaginary parts of impedance data. The calibrated parameters show good agreement with the parameters chosen to generate the data, as shown in Table 1, although there are disagreements in the found and used parameter values. The frequency range is from 50 to 6300 Hz with a step size of 2 Hz.

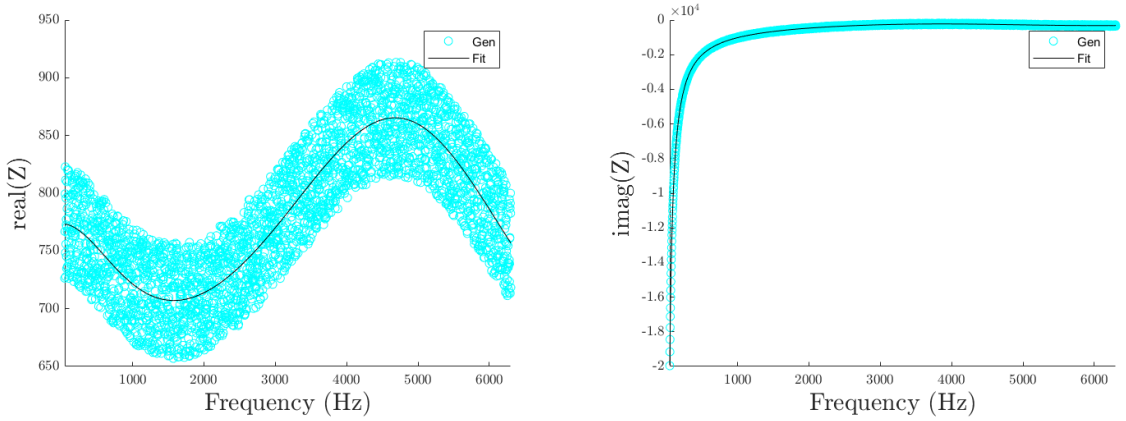

(a) (b)

Figure 4.1 – Generated and calibrated impedance curves resulting from Nelder-Mead ("fminsearch" function) parameter optimisation method, where (a) is the real part and (b) is the imaginary part of such impedance.

	Generated	Initial Guess	Calibrated
ϕ	0.90	0.60	0.90
σ	80000 Nsm^{-2}	200000 Nsm^{-2}	80179 Nsm^{-2}
α_∞	1.30	2	1.30
λ	30.0 μm	50.0 μm	30.0 μm
λ'	100.0 μm	60.0 μm	98.8 μm
k_0'	20.0 $\cdot 10^{-10}$ m^2	10.0 $\cdot 10^{-10}$ m^2	19.9 $\cdot 10^{-10}$ m^2

Table 1 – Generated and calibrated parameters resulting from the Nelder-Mead approach.

Despite the good calibration result shown in Fig. 4.1, the application of this method is also subject to the problems associated with local minimisation techniques, where the sensitivity to initial guess and convergence to local minima can induce different estimation. Global minimisation methods are far more complex than the ones presented in this work and were not tested.

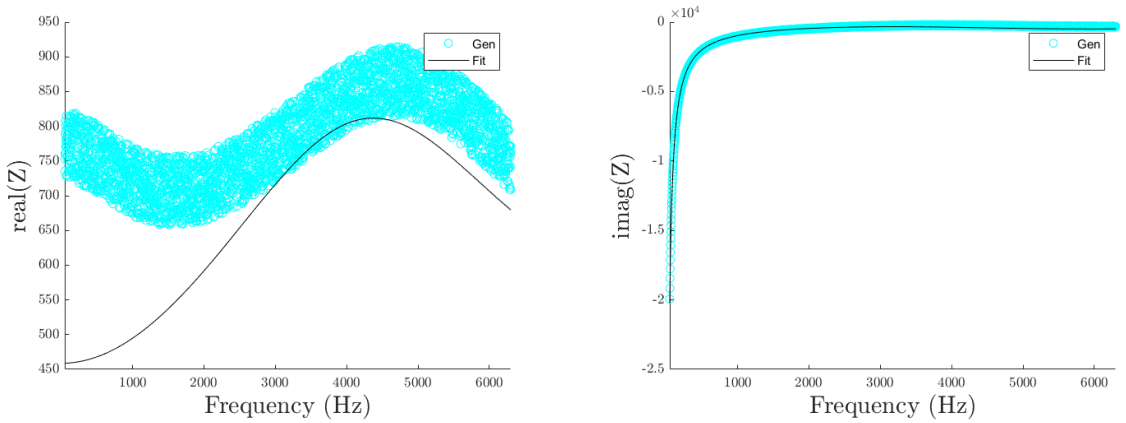

(a) (b)

Figure 4.2 – Incorrect curve fitting obtained from Nelder-Mead optimisation method by changing initial guess, where (a) is the real part and (b) is the imaginary part of the generated and fit impedance.

Both the mentioned issues with the presented optimisation routes are exemplified in Fig. 4.2. By simply changing the value of one initial guess parameter (in this case, the static air flow resistivity from 200000 Nsm^{-2} to 20000 Nsm^{-2}), the obtained fitting curve becomes less accurate, and here the problem of unconstrained methods also makes itself present. The calibrated value of the high-frequency limit of the tortuosity α_∞ is less than one, and the viscous characteristic length λ is nearly the size of molecules (what would characterise a medium impervious to sound). Given the method knows no constraints, it might reach values with no physical meaning yet mathematically fitting. The used and obtained parameters related to Fig. 4.2 are shown in Table 2.

Another aspect worth noting is the "weight" either the real or imaginary component may have on the fitting. In this case, these components' values may vary in order of magnitude for a given sample, as shown in Figs. 4.1 and 4.2. The optimisation methods are more likely to reach minimum cost function values by following the path reducing greater magnitude component, even if the other component reaches non-optimal values in relation to experimental data. One suggestion presented by Zoltowski (1984) is the weighting of the data proportional to the impedance values in the cost function, as shown in Eq. 4.2. This method showed little improvement when tested.

$$R(\mathbf{a}) = \frac{1}{2}\sum_{\omega}\left[\frac{\mathrm{Re}(Z^{\mathrm{exp})} - \mathrm{Re}(Z)}{\mathrm{Re}(Z^{\mathrm{exp}})} + \frac{\mathrm{Im}(Z^{\mathrm{exp}}) - \mathrm{Im}(Z)}{\mathrm{Im}(Z^{\mathrm{exp}})}\right]. \tag{4.2}$$

4.1.1.2 Levenberg-Marquardt

The other unconstrained method tested was Levenberg-Marquardt. A question concerning this and other methods based on the gradient of the cost function is the usage

	Generated	Initial Guess	Calibrated
ϕ	0.90	0.60	0.89
σ	80000 Nsm^{-2}	20000 Nsm^{-2}	66696 Nsm^{-2}
α_∞	1.3	2.0	$8.9{\cdot}10^{-9}$
λ	30.0 μm	50.0 μm	$1.4{\cdot}10^{-3}$ μm
λ'	100.0 μm	60.0 μm	104.9 μm
k_0'	20.0 $\cdot 10^{-10}$ m^2	10.0 $\cdot 10^{-10}$ m^2	40.0 $\cdot 10^{-10}$ m^2

Table 2 – Poorly approached parameters resulting from using the Nelder-Mead method with a "bad" initial guess.

of its second derivative concerning parameters in the called Hessian matrix α_{kl}, given by

$$\alpha_{kl} = \frac{\partial^2 R(\mathbf{a}^2)}{\partial a_k \partial a_l}. \tag{4.3}$$

Aside from the uneasy task of calculating the gradient, it may be either insignificant to the function or destabilise the fitting due to higher sensitivity to noise and outlier points. The suggestion given by Press, Teukolsky e Vetterling (1992) is using only the first derivatives of the cost function, as shown in Eq. 4.4. Also, the matrix is called "Quasi-Hessian" in some studies (WILAMOWSKI; YU, 2010). The usage of both formats was tested.

$$\alpha_{kl} = \sum_{i=1}^{N} \frac{1}{\sigma_{\text{er}}^2} \left[\frac{\partial Z(\omega, \mathbf{a})}{\partial a_k} \frac{\partial Z(\omega, \mathbf{a})}{\partial a_l} \right]. \tag{4.4}$$

This method was used in association with the normalised set of six parameters proposed by Zieliński (2015). These normalised parameters are suggested as a means of optimising parameters within approximately the same scale, in contrast to the regular ones proposed in the original JCAL contributions where the airflow resistivity σ might be of the order of 100000 Nsm^{-2} while the static thermal permeability might oscillate around values of $5 \cdot 10^{-10}$ m^2. They are all "unequivocally" related to porous structure geometry parameters and air properties, i.e. as in the case of six non-normalized JCAL parameters, the parameters proposed by Zieliński (2015) are directly related to pore geometry.

One problem in using these normalised parameters is that some JCAL parameters are related to the normalised ones by equations containing square roots (see Appendix A). Like Nelder-Mead and all unconstrained methods, there are no bounds stopping the algorithm from obtaining negative values for a parameter as long as it reaches a local minimum. Then, if a fitted normalised parameter has a negative value, the actual JCAL parameter will have a complex value or another physical impossibility, which can be a conceptual error. Fitted curves are shown in Fig. 4.3 that represent a very good fit to generated noisy data, but it is achieved with a negative value normalised parameter that incurs in the parameters shown in Table 3.

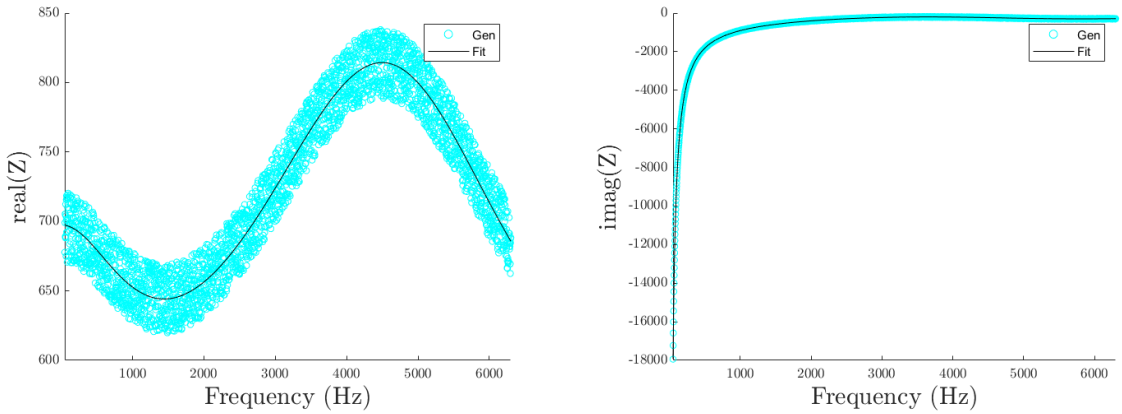

(a) (b)

Figure 4.3 – Generated and calibrated impedance curves resulting from the implemented Levenberg-Marquardt parameter optimisation method, where (a) is the real part and (b) is the imaginary part of such impedance.

	Generated	Initial Guess	Calibrated
ϕ	0.90	1	0.90
σ	80000 Nsm^{-2}	7439.1 Nsm^{-2}	81334 Nsm^{-2}
α_∞	1.3	2.0	3.0
λ	30.0 μm	199.3 μm	76.1i μm
λ'	100.0 μm	141.4 μm	86.7 μm
k_0'	20.0 $\cdot 10^{-10}$ m^2	10.0 $\cdot 10^{-10}$ m^2	18.6 $\cdot 10^{-10}$ m^2

Table 3 – Inconsistent approached parameters resulting from using the Levenberg Marquardt method with an inconsistent initial guess.

Herein it is important to notice that the set of parameters used in the initial guess does not need to be physically consistent, so even though the normalised and regular parameters are all related, the normalised initial guess may represent an inconsistent set of parameters, and the final result may turn out consistent. This is mentioned because, even though the results are not physically accurate, the used initial guess to obtain the results presented in Fig. 4.3 was a vector of ones (the value of every normalised parameter is one), representing an inconsistent set that yields, a good curve fit. This initial guess is used throughout Zieliński (2015), yielding consistent results for both synthetic data and real material samples.

The other aspect being investigated is using a full Hessian as presented in Eq. 4.3 or the approximation presented in Eq. 4.4. As expected, the approximation reached minimum values in fewer iterations than the full version, given the higher values obtained from the first derivatives of the model. This is better seen in Figs. 4.4 and 4.5, where the iterations until the minimum difference between fitting impedance and experimental data are reached. Figure 4.4 shows the steps toward the impedance curve presented in Fig. 4.3a, from the initial guess to the final approximation as presented in Table 3. Using the same initial guess, the curves displayed in Fig. 4.5 are also fitting the same impedance values as Fig. 4.3a, yet the number of iterations (1200 vs 20) is far higher than those

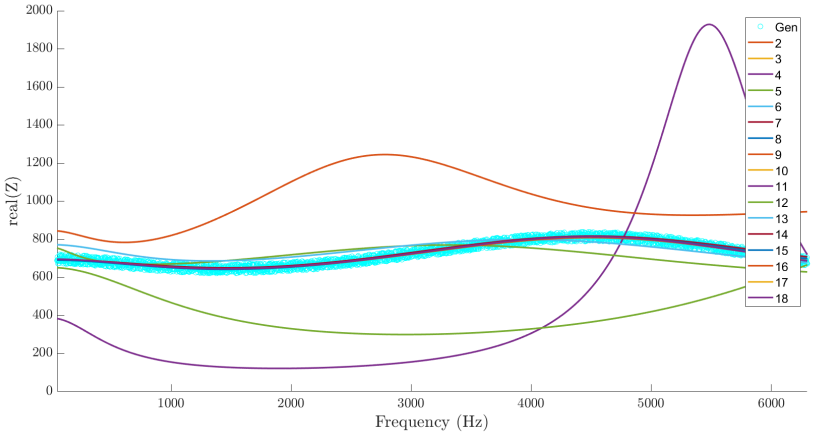

Figure 4.4 – Iterations of the impedance real part using the approximate Hessian.

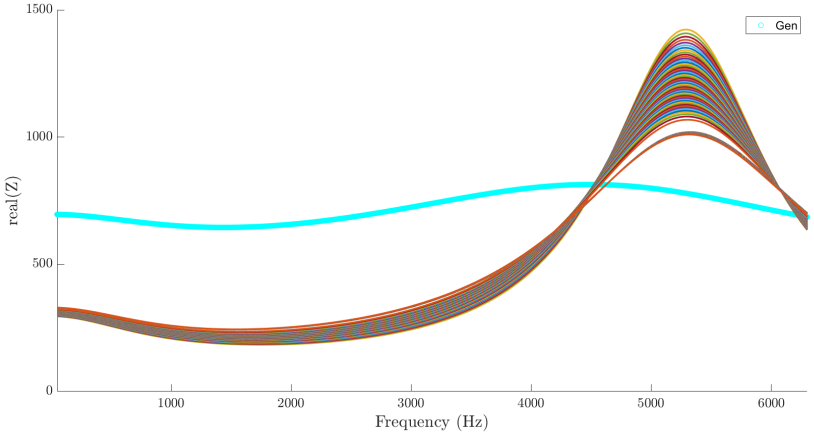

Figure 4.5 – Iterations of the impedance real part using a full Hessian.

necessary for the approximation using the approximate Hessian. It can be seen that the full Hessian has a much lower convergence rate and also an apparent higher sensibility to local minima. Even though the initial results obtained from fitting using approximate Hessian are inconsistent, as presented in Table 3, it is much quicker convergence makes it, a priori, a better implementation of the Levenberg-Marquardt algorithm for the present problem. Using a slightly different initial guess (a vector of normalised parameters with value 0,99 instead of one) allows the method to reach closer parameter values to those used to generate the synthetic data, as shown in Fig. 4.6 and Tab. 4. Henceforth the adopted strategy for all analyses, including experimental ones, was simple trial and error with the initial guess for any given to-be-fitted impedance curve.

Upon discussing the shortcomings of the unconstrained methods presented, one main strategy is available to improve their effectiveness and even constrained methods. This is to evaluate some parameters directly and only fit those not available from direct methods. This is the case, for example, of the work by Panneton e Gros (2005), where the JCA model (which only uses five macroscopical/pore geometry parameters) is fitted to experimental impedance curves of different materials, but only tortuosity and the characteristic lengths are evaluated through the fitting, while porosity and airflow resistivity are measured

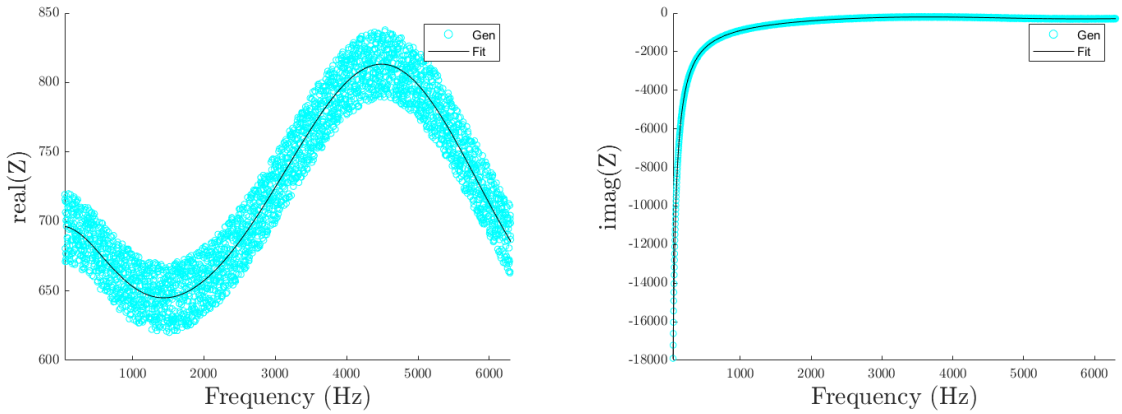

(a) (b)

Figure 4.6 – Consistent approached parameters resulting from the use of the Levenberg Marquardt method with an inconsistent initial guess.

	Generated	Initial Guess	Calibrated
ϕ	0.9	0.99	0.90
σ	80000 Nsm^{-2}	7439 Nsm^{-2}	79876 Nsm^{-2}
α_∞	1.30	1.99	1.30
λ	30.0 μm	201.3 μm	29.9 μm
λ'	100.0 μm	143.4 μm	102.1 μm
k_0'	20.0$\cdot 10^{-10}$ m^2	50.0 $\cdot 10^{-10}$ m^2	20.2 $\cdot 10^{-10}$ m^2

Table 4 – Consistent approached parameters resulting from using the Levenberg Marquardt method with an inconsistent initial guess.

directly. Fixating some parameters will reduce the chance of convergence to incorrect local minima and reduce the necessary number of iterations, besides reducing the problems associated with different magnitude scales.

4.1.1.3 Constrained methods

The Levenberg-Marquardt method is simple, and its implementation allows greater control and insight into the fitting and optimisation procedure. Constrained methods are considerably more complicated to implement, although many of them are readily available and implemented in libraries and toolboxes for different programming languages.

The first functions to be tested belonged to the "Global Optimization Toolbox" from MatLab (GLOBAL...,). Different algorithms are implemented as functions that constitute this library, which aims to provide tools to find global minima for different functions using different and combined routes. The constraints may be linear equality and inequality when such relations exist between parameters. Upper and lower bounds are also available, which are the most interesting to the acoustic impedance fitting since all parameters are bounded. Using the same initial guess to fit the same curve as presented in the tested methods (Fig. 4.1 and 4.3), different functions (that use different algorithms/approaches) from this library were tested to fit the impedance curve. The obtained results are presented in

	Generated	fmincon	MultiStart	PatternSearch	ga
ϕ	0.90	0.90	0.91	0.90	0.93
σ (Nsm^{-2})	80000	80340	84276	84166	155640
α_∞	1.3	1.0	2.2	1.7	1.8
λ (μm)	30.0	22.1	400.0	50.0	98.9
λ' (μm)	100.0	87.6	63.1	60.0	13.0
k_0' (m^2)	$20.0 \cdot 10^{-10}$	$11.1 \cdot 10^{-10}$	$100.0 \cdot 10^{-10}$	$10.0 \cdot 10^{-10}$	$99.6 \cdot 10^{-10}$

Table 5 – Approached parameters resulting from use of different functions from the "Global Optimization Toolbox".

	Generated	L-BFGS-B	Powell	Nelder-Mead	TNC
ϕ	0.9	0.99	0.901	0.99	0.76
σ (Nsm^{-2})	80000	130060	79142	101076	53398
α_∞	1.3	3.6	2.0	1.5	1.3
λ (μm)	30	199.6	66.9	17.9	100.4
λ' (μm)	100	353.3	17.9	81.6	53.9
k_0' (m^2)	$20.0 \cdot 10^{-10}$	$1.0 \cdot 10^{-10}$	$382.6 \cdot 10^{-10}$	$100.0 \cdot 10^{-10}$	$1.0 \cdot 10^{-10}$

Table 6 – Approached parameters resulting from use of different algorithms inside the "minimize" function from "scipy.optimize" package.

Table 5 with the respectively used functions. The imposed bounds were:

- Lower bound: $\phi \geq 0.1$, $\sigma \geq 1000$ Nsm^{-2}, $\alpha_\infty \geq 1$, $\lambda \geq 10$ μm, $\lambda' \geq 10$ μm, $k_0' \geq 1 \cdot 10^{-10}$

It can be seen from Table 5 that most fits make good approximations for the porosity and airflow resistivity parameters and poor ones for the others (tortuosity, characteristic lengths and static thermal permeability). Besides the difference in scale that jeopardises the precision of approximations, there is also the matter of function sensitivity to each parameter, i.e. influence a change of parameter value has on the outcome of the function, and in this case, the impedance curve. This will be briefly discussed in Section 4.2.

The other functions tested belong to the "scipy" library for Python programming language, specifically the "minimize" function inside the "optimize" package (SCIPY...,). Opposed to the Global Optimization toolbox, this function only finds local minima, although possessing the possibility to establish bounds and constraints. Inside the "minimize" function, diverse implemented algorithms are available (for greater insight into some of these, Andrei (2022) presents the full equations and development for them). The obtained approximations using different algorithm options are shown in Table 6. The results obtained are not as accurate as those presented in Table 5, but it is worth noting that once again, those results that converge to close values seem to reach better approximations for the porosity and airflow resistivity, while other parameters have poor estimations. Once again, this may be related to the sensitivity aspects of the model associated with the minimisation algorithms employed.

4.2 Sensitivity analysis

Different sound absorption curves were plotted for individually varying parameters to understand the behaviour of the JCAL impedance function and the influence of variation of each parameter over the obtained sound absorption. While one parameter was varied, the others were kept constant to isolate the individual influence of each one. Figure 4.7 shows the obtained absorption curves for variation of each parameter. Table 7 shows the range of varied parameters and the values of the parameters kept constant. The ranges were chosen from physical limitations to parameter values and their expected ranges. Porosity, for example, from the definition, must have a value between zero and one. The tortuosity high-frequency limit must have a value higher than one. The characteristic lengths must have values that reflect porous media pervious to sound propagation ($\geq 10\,\mu$m (ALLARD; ATALLA, 2009)). Both air flow resistivity and static thermal permeability ranges were determined from literature reports, the same for the upper bounds of the characteristic lengths and tortuosity ranges.

Notice that, for consistency maintenance in the used parameters, the varying values λ are accompanied by varying values of λ', always kept higher. Other factors and relations between parameters, such as those proposed in Johnson, Koplik e Dashen (1987),Champoux e Allard (1991), Lafarge et al. (1997), and Berryman (1980), since these are specified for "common" porous materials or specific cases such as in the relation proposed by Berryman (1980), limited to rigid spheres.

value/range	ϕ	σ	α_∞	λ	λ'	k_0'
ϕ	0.05 - 0,95	0.7	0.7	0.7	0.7	0.7
σ (Nsm^{-2})	5000	100-2e6	5000	5000	5000	500000
α_∞	2	2	1-3.5	2	2	2
λ (μm)	20	20	20	10-1000	10	20
λ' (μm)	50	50	50	15-1005	20-1005	50
k_0' (m^2)	$50{\cdot}10^{-10}$	$50{\cdot}10^{-10}$	$50{\cdot}10^{-10}$	$50{\cdot}10^{-10}$	$50{\cdot}10^{-10}$	1.5 - $100{\cdot}10^{-10}$

Table 7 – Used parameters and the variation range of each specific parameter.

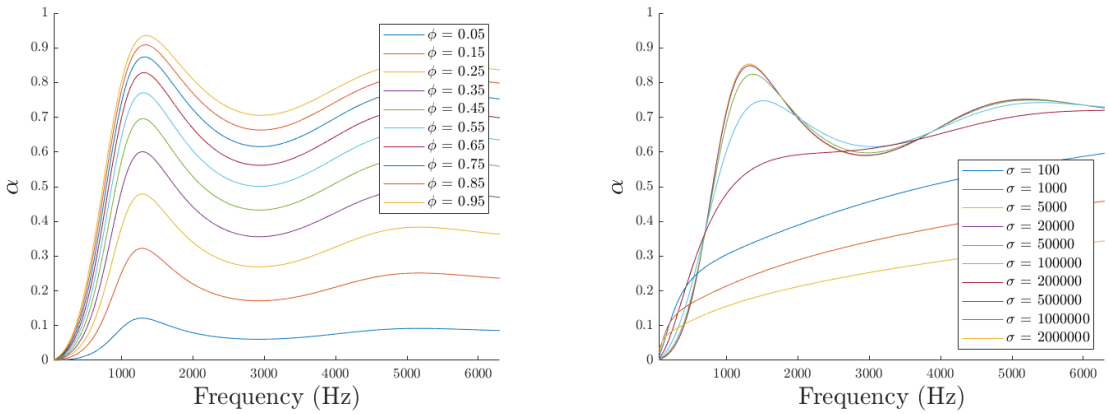

(a) ϕ

(b) σ

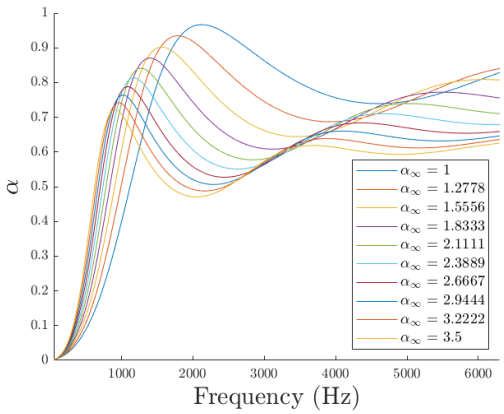

(c) α_∞

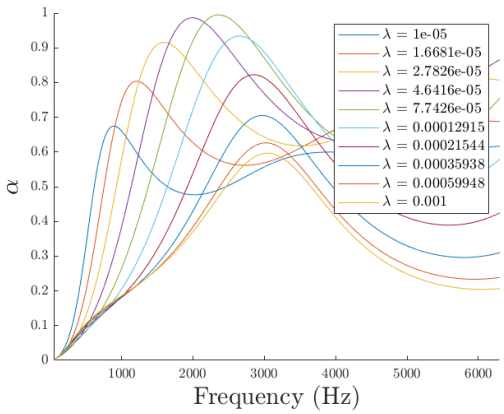

(d) λ

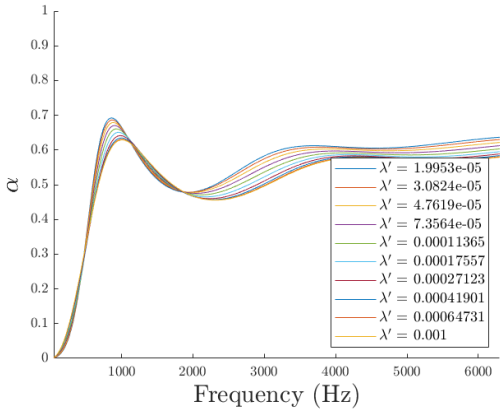

(e) λ'

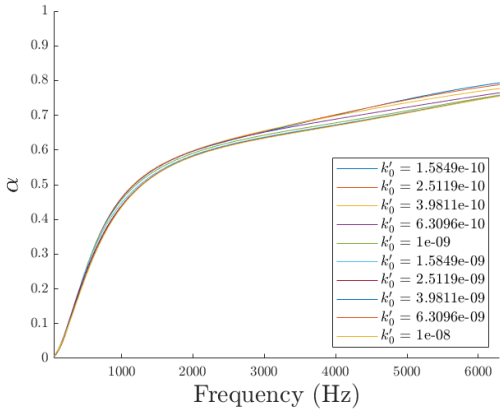

(f) k_0'

Figure 4.7 – Sound absorption curves for varying parameters, namely (a) porosity, (b) air flow resistivity, (c) high-frequency limit of the tortuosity, (d) viscous characteristic length, (e) thermal characteristic length, (f) static thermal permeability.

From Fig. 4.7 is seen that parameters related to thermal effects, thermal characteristic length λ' and static thermal permeability k_0' will exert little influence in the final absorption curves. Contrasting, porosity ϕ, and static air flow resistivity σ exert great influence in all the studied frequency ranges. Tortuosity α_∞ has an intermediate effect in the final curve, mainly dislocating the absorption peaks to smaller frequencies as it gets higher. It is also interesting to notice that apart from porosity, no parameter has a

permanently proportional relation to sound absorption, that is, maximising or minimising it will not mean the absorption coefficient will match this behaviour. For each parameter, there are optimum values for different frequency ranges that maximise sound absorption.

In comparison, Ouisse et al. (2012) presents a full sensitivity analysis for the JCA model for each parameter in relation to the sound absorption coefficient and the imaginary and real parts of impedance. Though no study has been conducted on static thermal permeability due to the choice of model, the author finds that for different frequency ranges, the model has different sensitivities to each parameter. Nevertheless, the bounds used in that study for the parameters are smaller than those presented in Fig. 4.7 (e.g. $0,7 \leq \phi \leq 0,99$), and the author does find that up to frequencies of 100 Hz, porosity exerts the most influence, while for higher frequencies airflow, resistivity is the most defining feature jointly with characteristic viscous length. This is a fundamental conclusion for inverse characterization purposes. Other more recent studies such as those by Magliacano et al. (2020) and (TRINH; GUILLEMINOT; PERROT, 2021) use more refined techniques such as Monte-Carlo to analyse sensitivity to parameters in specific models (models reflecting a specific porous material geometry with varying characteristics such as pore width) and also optimize certain material geometries.

4.3 Multilayer systems

In order to evaluate multilayer systems, a routine was implemented in MatLab with the equations necessary to obtain the surface impedance of a multilayer system. To test this code, a comparison is made with the first example shown in section 11.7.1 of Allard e Atalla (2009). It is the impedance of a sound absorber composed of a sheet of glass wool bonded to a layer of plastic foam, taken from the experimental results from Rebillard et al. (1992). Each layer height and the parameters necessary for the JCA model are given for both materials. The implemented routine has JCA and JCAL models embedded, but for this case, the JCA model was used since it is the model used at the original reference.

Figure 4.8a shows the impedance ratio plots of the original study compared to those obtained with our implemented model, and Fig. 4.8b shows comparison of their respective sound absorption coefficients. The surface impedances (real and imaginary parts) were normalized to the atmosphere air impedance. Therefore, the values might vary slightly since there was no available information on the atmospheric conditions at testing. Despite this, both results seem to match, showing the appropriate behaviour of the implemented routine.

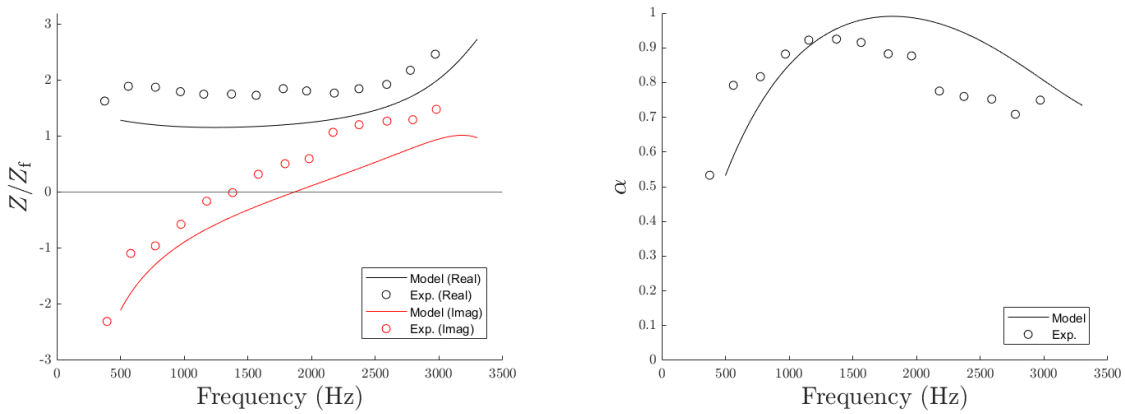

(a) (b)

Figure 4.8 – (a) Impedance ratios shown in Allard e Atalla (2009) and those obtained with the presented model, (b) their respective sound absorptions.

As mentioned, the performance of an absorber may be improved by the use of different materials stacked/bonded. Indeed, studies show that a multilayer system may have equal or improved sound absorption compared to its individual constituents with the same thickness and even show routes to optimize this approach (TANNEAU; CASIMIR; LAMARY, 2006; YAMAMOTO et al., 2008; MAHASARANON et al., 2012). This enhancement is, of course, resultant of changes in the surface impedance of the sample. The porous ceramic samples produced in this work are acoustically characterised mostly through impedance measurements. That freeze-casting fabrication may generate inhomogeneous microstructures, and this modified behaviour in impedance could be present. It could be detrimental to model calibration methods necessary to describe the material acoustical properties.

Additional to the testing comparing results shown in Fig. 4.8, generated multilayer systems were fitted using single-layer models. This short experiment was motivated by the sequence in which characterization procedures were conducted on produced samples. There was a possibility of obtaining graded porosity systems from the freeze-casting process (as discussed in Sec. 3.1.2.2) and the effects this grading exert on sound absorption were likely to be measured before the pore structure was evaluated using material characterization methods such as SEM, given these methods were mostly destructive. Since the acoustic characterization of final samples was mostly reliant on single-layer model curve fitting, it was likely that eventually graded systems would be initially evaluated using single-layer models. For this reason, numerical testing was conducted, fitting multilayer systems with single-layer models, with the intention of understanding possible effects of such a practice.

Using some methods presented in Section 4.1, we wanted to investigate what effects would fit a given multilayer material impedance with a single-layer model. For that, a three-layer system was heuristically determined. It is a small dense layer at the bottom, similar to that expected from unidirectional frozen freeze-cast samples, followed by a high porosity central layer and a top layer with intermediate properties, approximately

reproducing the microstructure found in studies such as Hong et al. (2011). The used properties for each layer are shown in Table 8

	Layer 1	Layer 2	Layer 3
ϕ	0.6	0.8	0.2
σ Nsm^{-2}	900000	300000	1100000
α_∞	1.2	1.1	1.7
λ (μm)	50	150	20
λ' (μm)	90	200	30
k_0' (m^2)	$15{\cdot}10^{-10}$	$20{\cdot}10^{-10}$	$5{\cdot}10^{-10}$
Height (mm)	10	8	2

Table 8 – Studied multilayer system properties.

The impedance curves were generated for this system, and the calibration methods presented in Section 4.1.1 were tested. First, the unconstrained methods (Nelder-Mead and Levenberg-Marquardt) were used. For various initial guesses, both methods resulted in physically inconsistent parameters, such as porosities (much) higher than one and negative characteristic lengths. Due to this apparent ineptitude of unconstrained methods when applied to this case, the "fmincon" function from the Global Optimization Toolbox was used with bounds to every parameter.

While this route did find parameters within appropriate bounds (as expected) shown in Table 9, the fitted parameters were mostly minimised or maximised within the allowed bounds, except for the airflow resistivity σ. Figure 4.9 shows the generated and fitted impedance curves . It can be seen that the found porosity for a single-layer material is greater than all individual layers, while the resistivity is smaller than that of all layers. It can be expected from parameter sensitivity as shown in Section 4.2

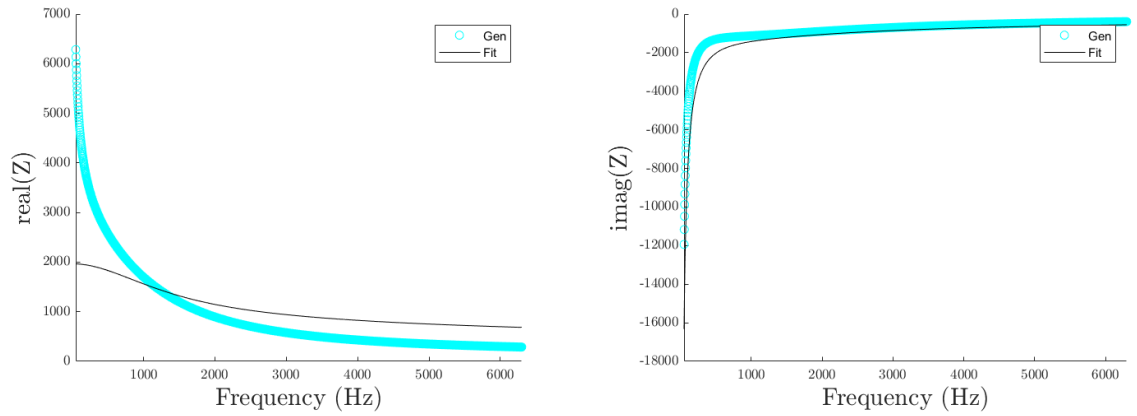

(a) (b)

Figure 4.9 – Real (a) and imaginary (b) parts of the generated and fitted impedance of the defined multilayer system.

Though the errors in parameter approximation are plentiful and its explanations are various, an interesting remark that may be done with certainty from the references and

	ϕ	σ (Nsm^{-2})	α_∞	λ (μm)	λ' (μm)	k_0' (m^2)
Fit	0.99	218860	1	400	400	$1 \cdot 10^{-10}$

Table 9 – Parameters found through the fitting of the multilayer impedance curves.

numerical results presented is that the use of inverse methods applied to multilayer will likely result in a mix of over and underestimation of different parameters. This is simply because the bonding of layers will cause impedance variations (increase and decrease) of both parts of impedance in different frequency bands, as well explained at Allard e Atalla (2009), and fitting algorithms will end up varying the parameters with a greater influence of impedance in these bands often minimising parameters or maximising it within bounds since the values obtained from multilayer systems can be greater than that attainable from single materials.

5 Experimental investigation

5.1 Acoustic measurements

The produced sample's surface impedance and sound absorption coefficient were measured using the SW466 impedance tube from BSWA (shown in Fig. 5.1). The experimental setup comprises two diameter tubes ($\varnothing = 30$ mm and $\varnothing = 60$ mm), a loudspeaker, an amplifier, an acquisition board, four microphones, and the VA-Lab4 software to acquire the data. The impedance measurements were performed following ISO 10534-2 standard (INTERNATIONAL ORGANIZATION FOR STANDARDIZATION, 1998).

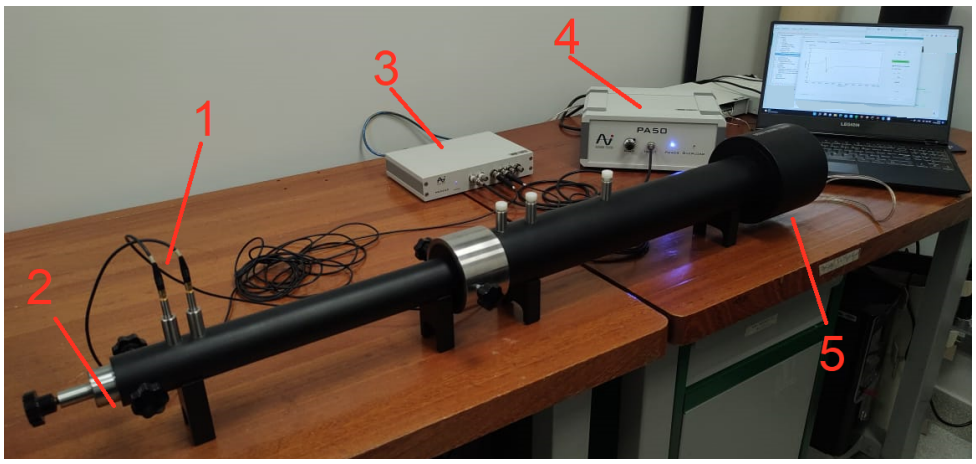

Figure 5.1 – Used impedance tube for acoustics measurements, where (1) is are the microphones, (2) is the sample holder, (3) is the acquisition board, (4) is the amplifier, and (5) is the sound source.

The microphones were calibrated using a CA115 114 dB sound level calibrator before each measurement, and background noise was measured. A thorough description of the methodology used and its steps can be found in Mendes (2020). All measurements were performed with no gap behind the sample, i.e. with a rigid backing condition.

5.2 Sample production

Two main ceramic samples were produced, one using camphene as a solvent and the other using DMSO. The use of two different solvents investigates the different obtained

pore morphologies and the consequent changes in sound absorption behavior. This choice of solvents, nevertheless, impacts directly on the cost of the process. Compared to deionized water (another viable solvent for freeze-casting), the same mass of DMSO is 4-5 times more expensive, while camphene may be up to 10 times the price of water. Still in the matter of cost and scalability of the process, the freezing and freeze-drying process of large batches and pieces of freeze-cast ceramics can turn its fabrication route very costly when compared to other process of production of porous ceramics. Therefore, large scale production of freeze-cast ceramics can be challenging and is likely not an immediate choice for the production of porous ceramics for acoustic purposes, though unique pore morphologies obtained from freeze-casting may prove to be worth the higher cost of production, besides the continuos research dedicated to this method that may eventually decrease its cost.

Going back to the production method used, additional to the change in the used solvent, the DMSO-based samples were prepared with a different array of parameters (varying temperature and solid loading) from that used for camphene-based samples (varying ceramic ratio). Table 10 shows the tested parameter variations of each group.

	DMSO	Camphene
Freezing Temperature	$-130°C$,$-150°C$,$-170°C$	$\sim -180°C$
Ceramics (Al_2O_3 wt%/MgO wt%)	72/28	60/40; 72/28; 90/10
Solid loading (solid vol%/liquid vol%)	80/20 ; 70/30	80/20

Table 10 – Evaluated parameter variation according to sample type.

The initial analysis proposed for the camphene samples was a study to understand the possible influence of ceramic phase composition on sound absorption performance. Therefore, every parameter was kept constant except by starting powder proportion. The three chosen concentrations (60/40, 72/28, 90/10, in weight) were chosen with the aim of obtaining three different final phase compositions. As it may be verified in Fig. 3.6, these three chosen compositions are in three different regions of the phase diagram and, considering a sintering temperature above 1000 °C, are expected to yield: a magnesium oxide spinel-rich composition, a nearly pure spinel composition, and an aluminum oxide spinel-rich composition.

For the DMSO-based samples, the investigation was focused on the freeze-casting parameter variation, in search of changes in parameters whose relation to acoustic performance is well established. In this case, the starting powder proportion was kept, while varying process parameters.

One of the main challenges of the ceramics production process was the sample's size and volume because, in most studies presented in the literature, the unidirectional samples freezing produces were relatively small diameter and commonly a small height, e.g. $\varnothing = 8$ mm,$h = 16$ mm in Fu et al. (2008), and simple pore structure analysis in (DEVILLE; SAIZ; TOMSIA, 2007; FU et al., 2008; GHOSH et al., 2016; LEE et al., 2007; FUKUSHIMA et al., 2010). One of the issues with producing larger and thicker samples is

mentioned in Sec. 3.1.1.2. The green body produced after freeze-drying has little structural strength, and even with additives, large samples are subject to greater tension on the formed microstructure. Thus producing a sample from start to end without breakage was one of the main questions in the sample production phase, and the samples necessary for acoustic evaluation need to have at least $\varnothing = 30$ mm to fit the sample holder, as shown in Sec. 5.1.

Though we managed to produce $\varnothing = 30$ mm samples, the $\varnothing = 60$ mm samples necessary to evaluate the low-frequency behavior of the material using the available acoustic equipment were unfeasible in practice. The relatively large disks were fragile and placing such large green bodies on supports for sintering could lead them to fractures due to imperfections in the supports. Additionally, it is an economically complicated procedure, both in matters of spent raw materials (solvent and ceramic powders, mainly) and time. The freeze-drying time necessary for each camphene $\varnothing = 30$ mm sample was approximately one week. A sample with double the diameter could take even longer, besides the lessened quantity of samples that can fit inside the sintering oven, requiring more firing rounds. Therefore, all the studied samples were $\varnothing = 30$ mm, reducing the frequency range available for characterisation to 1000 Hz-6300 Hz.

5.2.1 Camphene-based samples

The first samples produced were those using camphene as a solvent. For the monoliths production, the used powders were CT3000SG α-Al_2O_3 (99.8 wt %/ Almatis Brazil) and MgO ($\geq$ 99 % trace metals basis, -325 mesh, Sigma Aldrich). The dispersant was Texaphor 963 (Cognis, Southampton Hampshire, UK, now called EFKA FA 4663) and the solvent was camphene (95 wt% /Sigma Aldrich). After weighing the necessary amounts of each system component, a solution containing camphene and Texaphor was prepared at 60° Celsius. After verifying the full dissolution of the dispersant in the solvent, alumina was added under vigorous stirring. Once the alumina powder was sufficiently dispersed, maintaining the stirring, MgO was added. The solution was kept under stirring for 15 min. after including both solid components to promote adequate dispersion in the solvent. The slurry preparation was performed using a closed vessel to avoid significant loss of solvent since camphene is very volatile, and when heated it will evaporate, losing liquid mass at high rates. An interesting detail is that different dispersant concentrations were necessary depending on the starting powder proportion to maintain the slurries with low viscosities. To keep the systems similar, a final Texaphor 963 concentration of 6 wt% (related to the total solid mass) was evaluated experimentally.

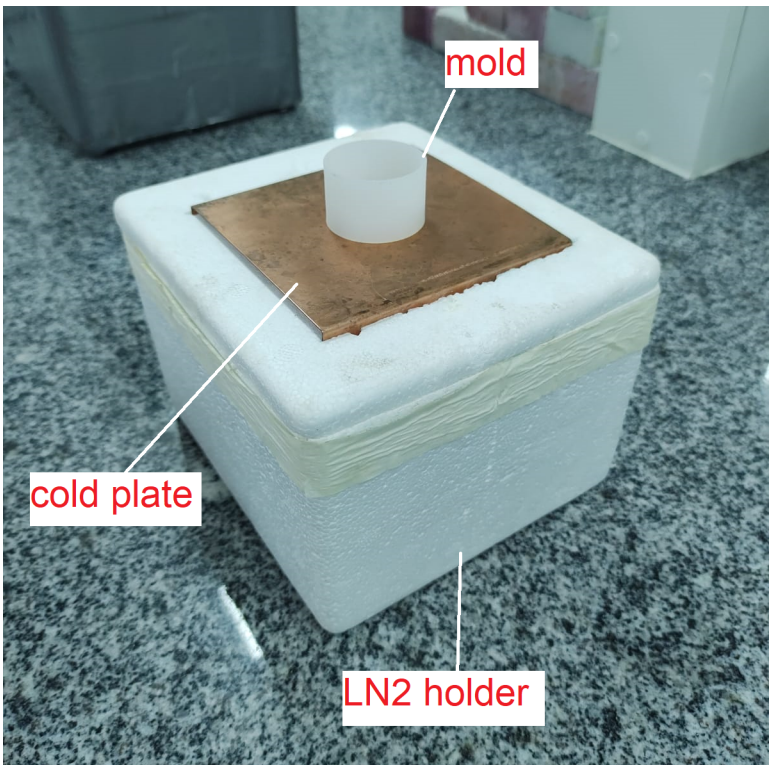

Figure 5.2 – Controlled temperature freeze-casting setup for camphene samples.

After mixing the materials, the suspension was poured inside a pre-heated PTFE (Teflon) mold on top of a refrigerated copper plate. In the freezing setup shown in Fig. 5.2, the cold plate is U-shaped and was partially immersed in liquid nitrogen to maintain its temperature. Following complete solidification, the slurry was demolded and left resting for seven days in the open air for complete camphene sublimation. After the sublimation, the green bodies were sintered at 1300°C for 2 hours, with a heating rate of 5°C/min.

5.2.2 DMSO-based samples

Between the production period of camphene-based samples and DMSO-based samples, the freezing set-up was improved, as shown in Fig. 5.3, now allowing temperature control inside a given temperature range.

The starting powders were the same as those used for the camphene-based samples. The dispersant used citric acid (Sigma Aldrich, 99,5 %) and the solvent was DMSO (Dinamica). The solvent and dispersant were mixed at ambient temperature using magnetic stirring until dissolution was observed, then the starting powders were added under vigorous stirring and mixed for approximately 25 min. The dispersant was used at 2 wt% of total solid mass. After initial mixing, the slurry passed through an ultrasound bath for 10 min. to help reduce possible agglomerates formed during the initial addition to the solution. Subsequent to the bathing process, the slurry is stirred again for an additional 15 min. Finally, it was poured inside a mold placed on top of the cold copper at a controlled temperature. When the sample was completely frozen, it was demolded and set in a sample

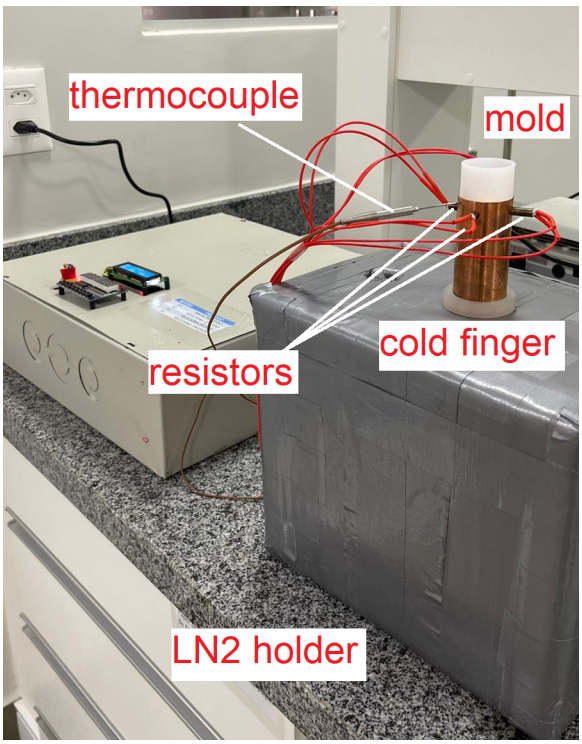

Figure 5.3 – Controlled temperature freeze-casting setup.

holder for the freeze-drying process. Finally, the green body was sintered with a heating rate of $3,5$ °C/min to 1300 °C, where the temperature was held for 2 h. Sintered samples were polished (sanded) to reach the dimensions appropriate to the impedance tube testing and to maintain a constant height between samples. After sanding, all samples were cleaned in an ultrasound bath using acetone and deionized water before testing to ensure possible pore obstructions created during polishing were undone. This process was conducted several times using the combinations of different temperatures and concentrations shown in Tab. 10 until enough samples of each parameter combination were obtained to conduct characterization.

5.3 Camphene-based samples material characterization

Diverse material characterisation methods were used on the produced samples to understand the relationship between microstructure and acoustic performance. SEM images were obtained using FEI Quanta 450, and diffraction patterns were obtained using Shimadzu XRD-6000.

5.3.1 Porosity and acoustic measurements

For every sample batch, the first characterisation method to be applied at them was the Archimedes principle, due to its non-destructive nature and immediate insight given on final pore structure characteristics, besides the expected direct correlation between

porosity and sound absorption. Following this analysis, impedance tube testing was the second to be conducted, searching for the sample's physical behaviour central to the present investigation. Thus, the results of both these methods will be presented together to give a holistic approach to interpreting the results.

The measured porosity of the first evaluated camphene samples is shown in Fig. 5.4a, and the measured sound absorption coefficient is shown in Fig. 5.4b. For all samples, the coefficient remains low throughout the evaluated frequency range, which is contradictory considering that all samples presented open porosity above 60%. This inconsistency had a few possible causes. The first would be an overly small average pore size and pore throat size. This would mean that most of the porous material layer was impervious to sound propagation, resulting in a lower sound absorption coefficient. This phenomenon was evaluated using methods such as mercury porosimetry, which gives a distribution of pore (entrance) size (GIESCHE, 2006), that were unavailable and usually turned the sample unusable for other characterisation methods. The second possible cause is the dense layer covering the outside of the sample. As mentioned in 3.1.2.2, dense material layers are formed during freezing. Since the planar faces of the samples were not polished in this first evaluation, the sample side facing the loudspeaker might have been dense, diminishing its sound absorption.

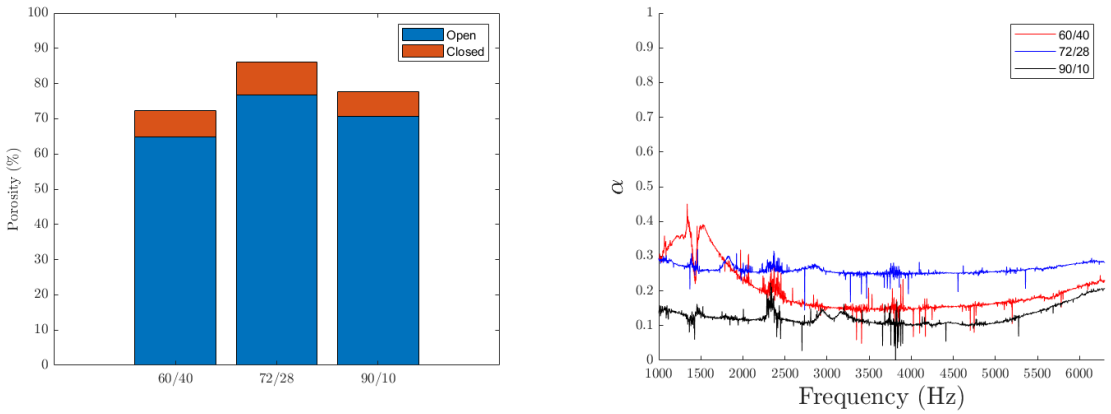

(a) (b)

Figure 5.4 – Porosity (a) and sound absorption coefficient (b) measurements of the first camphene samples to be tested with impedance tube.

Although no information was readily available on dense layers of material or even porosity distribution throughout the sample at the time the first camphene samples were being studied, as mentioned in Sec. 3.1.2.2. Some reports show that the initially formed dense layer is restricted to a relatively short height. Hong et al. (2011) produces alumina samples using camphene as a solvent and obtains dense layers with lengths $\leq 500\mu$m, even for samples produced using liquid nitrogen cooling. To solve the issue of dense layers covering a higher porosity bulk of the material, all samples from this point onward were polished and later cleansed in ultrasound solvent baths. This sequence allowed for greater certainty of the "accessibility" of higher porosity bulk to the incoming planar sound waves.

In addition, it also ensured an improved precision in sample height, which was controlled simply by mold sizing - a difficult task, given the hardly predictable densification behaviour of the samples during firing.

The measured sound absorption coefficients for the properly polished samples are shown in Fig. 5.5. A clear improvement in sound absorption performance can be seen throughout the analysed frequency range with all samples reaching upwards of 60% around 3000 Hz and 5000 Hz. Notice that, as in Fig. 5.4, each curve presents the sound absorption coefficient measured for samples in each of the three compositions. This simple practice was necessary to obtain the best performance from every produced sample.

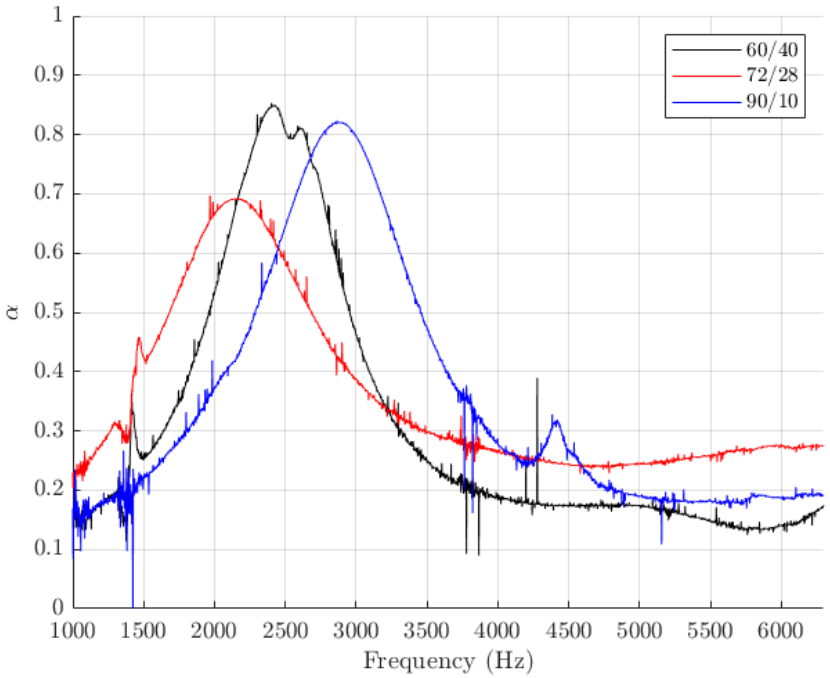

Figure 5.5 – Sound absorption coefficient (α) measurements of the polished camphene samples.

Since the influence of dense layers was verified, we checked other possible varying pore morphology effects. The freezing gradient applied to the samples was unidirectional, and the variation in pore morphology was likely in the freezing direction. Hence, a simple verification evaluated the sample's sound absorption with its bottom facing towards the sound source. The absorption curves shown in Fig. 5.5 are done with the top-up (the surface opposed to the cold source during freezing is considered top). Figure 5.6 shows the obtained absorption curves for both top and bottom facing the impedance tube loudspeaker (the sound absorption obtained for the top facing the loudspeaker is shown in blue in all plots, while the sound absorption obtained for the bottom facing the loudspeaker is represented by the solid lines). Despite possible uncertainty and error associated with measurements, the curves obtained for each side are quite different from one another. Considering that absorption peaks have similar magnitudes and occur in close frequencies, even if a graded pore structure is present for such samples, it is expected that the difference

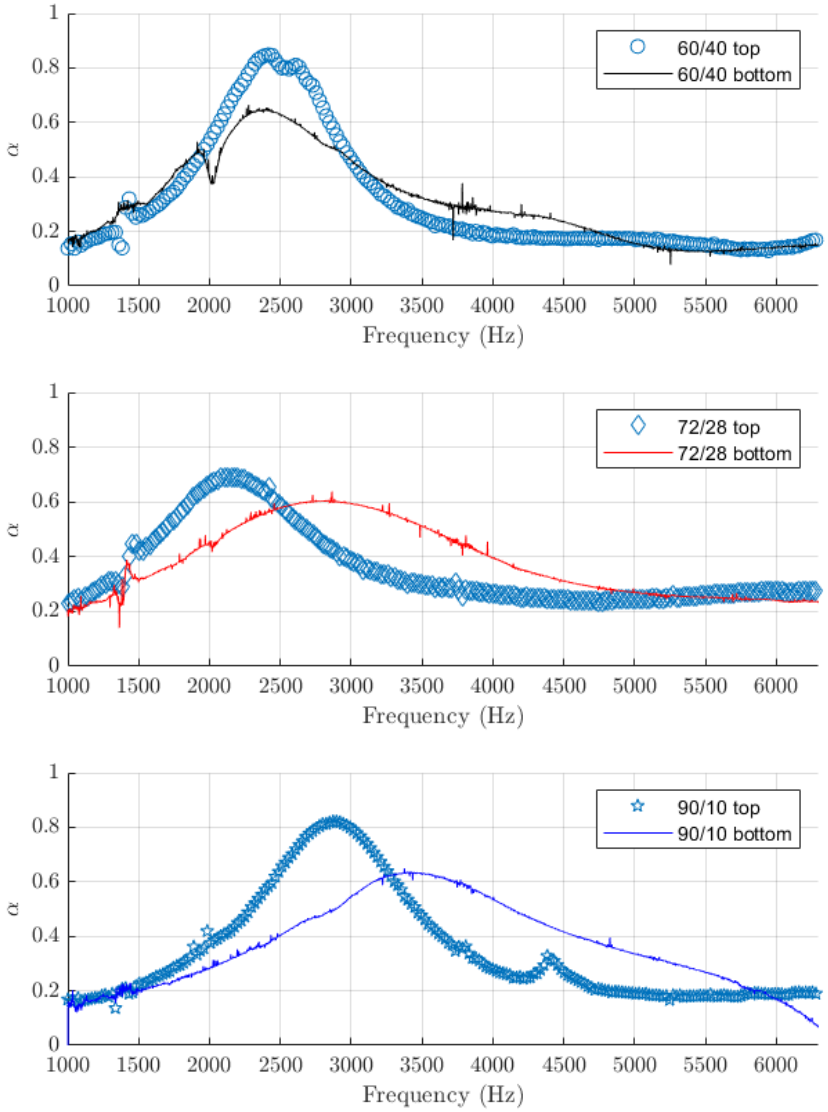

Figure 5.6 – Sound absorption coefficient (α) measurements of the camphene samples for top and bottom facing the sound source.

is not so significant and that application of inversion methods will not be significantly jeopardised.

At this point, we may evaluate the experimentally obtained impedance curves and consequently perform inverse characterisation. Though at initial testing impedance data was not registered due to operator error, the same samples were retested, and impedance curves were measured. Figure 5.6 shows the experimental and calibrated impedance curves for imaginary and real parts. For this calibration, the Levenberg-Marquardt method was used with heuristically varied initial guesses to fit the curves appropriately. To evaluate the quality of the fit, an average relative error function is defined as

$$\text{error} = \frac{1}{n}\sum_{i=1}^{n}\frac{|Z_{\text{fit}}(i) - Z_{\text{exp}}(i)|}{|Z_{\text{exp}}(i)|}, \tag{5.1}$$

for a given n quantity of evaluated frequency points.

	ϕ	α_∞	σ (Nsm^{-2})	λ (μm)	λ' (μm)	k_0' (m^2)	error (%)
60/40	17.54	2.037	7844	112.5	247.8	$462.7{\cdot}10^{-10}$	14.5
72/28	17.17	1.523	39037	52.58	92.61	$3.313{\cdot}10^{-10}$	19.21
90/10	22.14	2.297	7837	103.9	178.4	$23.55{\cdot}10^{-10}$	20.22

Table 11 – Obtained calibrated model parameters and relative errors for the camphene samples.

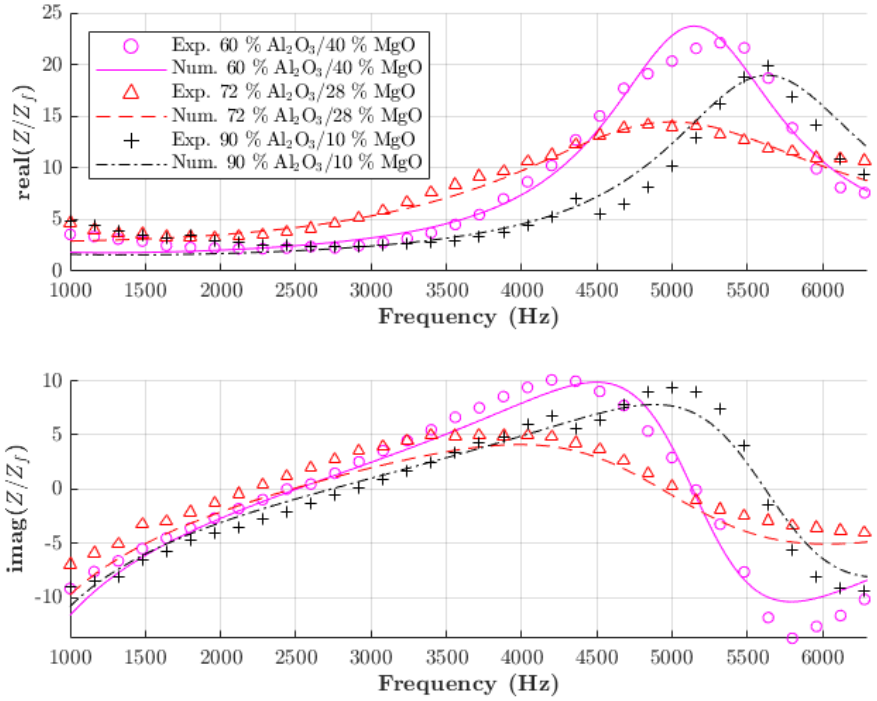

Figure 5.7 – Experimentally and numerically obtained surface impedance ratios for the evaluated camphene samples.

The estimated parameters and the average relative errors between fitted and experimental impedance, following Eq. 5.1, are shown in Table 11. It is noticeable the large disagreement between estimated porosity through Archimedes principle shown in Fig. 5.4a and that estimated from the inverse method. Although there is an error between the fit and experimental curves, even assuming the estimated parameters are within the error range of the impedance fitting, all porosities found through the acoustical method are much smaller than that evaluated with Archimedes principle. One possible explanation is the pore characteristic size. In Archimedes principle, small pores with characteristic sizes ≤ 1 μm are also measured as open porosity, even if these are not previous to sound propagation (JAOUEN; GOURDON; GLé, 2020). Assuming that most pores have small (≤ 1 μm) openings, it is reasonable to assume that acoustic measurements will "detect" a lessened porosity.

Another interesting aspect of the fitted parameters is the high tortuosity found for all samples. Although they are not necessarily above expected bounds for common

granular materials (BOUTIN; GEINDREAU, 2008), it still has a high value compared to other common materials. This is possibly due to the non-negligible closed porosity in the final sample, as shown in Fig. 5.4a. Close pores will interrupt the pore channels of interconnected porosity, creating more complex paths. Such relation is observed in both experimental (MAHASARANON et al., 2012) and numerical studies (CHENG et al., 2021).

Though no certain comments can be done on pore characteristic lengths and sizes without proper size distribution evaluation through methods such as mercury porosimetry, it is interesting to notice that the "72/28" sample is that with the smallest fitted characteristic lengths and highest static air flow resistivity. This behaviour is in line with that expected from a material with smaller pore openings, as it has been shown that smaller openings might result in greater airflow resistivity (ZIELIńSKI, 2016), and from the definition, a smaller opening will result in smaller characteristic lengths. It can be assumed that the "72/28" produced the smallest average pore size from all samples.

5.3.2 Phase formation

The XRD method was used to determine the phase quantity present in each sample and further evaluate the influence phase composition may have on the produced samples. This technique is destructive since it is a powder diffraction method, where parts of the sample are cut and ground to achieve the powder form. Figure 5.8 presents the x-ray diffraction patterns obtained for the final produced samples and those of the starting powders. All samples contain pronounced peaks corresponding to the starting powder and spinel phases, showing that the spinel phase was produced. It might not have been a complete reaction for the whole bulk of the samples since the "72/28" sample was expected to reach a nearly complete transition from corundum and periclase to spinel. Rietveld refinement was performed on the diffraction patterns using MAUD software for a more objective valuation of the present phase quantities. The yielded composition is shown in Table 12.

Section 3.2 explained the molar stoichiometric ratio between alumina and MgO ceramics. The mixture is fully converted to the spinel phase in an ideal scenario. Additionally, for compositions apart from this ratio, the predominant final sample phase other than spinel would be either MgO for mixtures below stoichiometry or Al_2O_3 for samples above stoichiometry. As it can be noticed from Table 12, this assumption follows a certain tendency. The "72/28" sample was supposed to have the higher spinel content with little remains of the other two phases. The other two compositions are within expectations, though the high corundum content in the "60/40" sample is odd since all corundum should have been consumed in the spinel phase transition. Only a "90/10" composition seems to yield predicted compositions, having consumed all periclase, forming spinel, while maintaining a high corundum content. The obtained phases may be explained by two

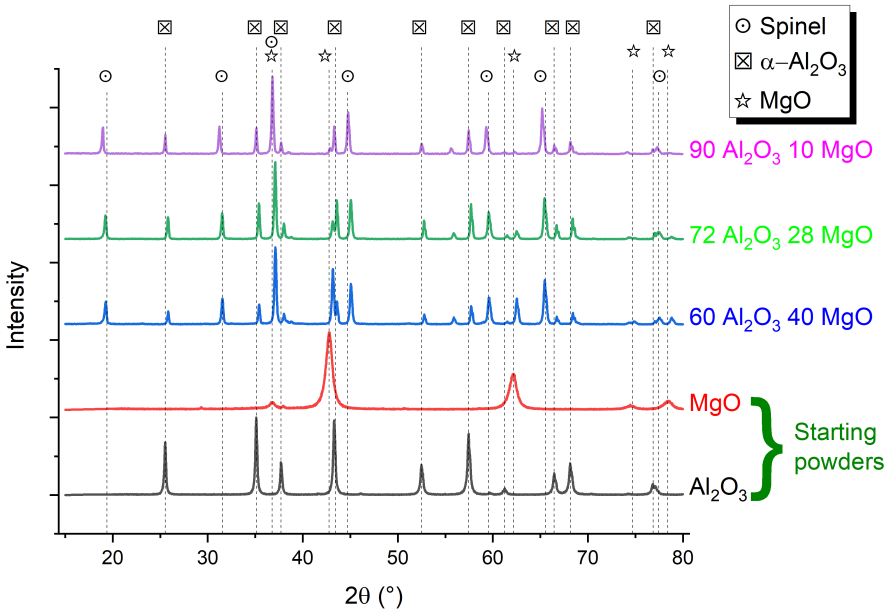

Figure 5.8 – Diffraction patterns of the final camphene samples and its corresponding starting powders.

pre-sintering factors, poor mixing and raw powder settling. Both are manifestations of the same problem: separated powders in the suspension when pouring. In the mixing phase, the powders were added separately. Though under vigorous stirring, it is still possible that parts of the suspension did not attain the appropriate blend, causing concentration distributions through the sample. Settling (decantation) is a cause pointed out by Araújo et al. (2018) to a similar phase composition issue, and that may likely affect the sample during freezing since both powders have different densities/grain sizes and freezing does not occur immediately after pouring, giving time for settling to occur. The other possible explanation, non-excluding the two previous, is insufficient sintering time. The established sintering temperature was enough to produce the spinel phase, although the time may have been insufficient to provide enough energy for phase transition throughout the bulk.

Independent of the reasons behind these final compositions, they make any association with the calibrated acoustic parameters difficult. One possible valuation, though, is that both Fig. 5.4a and Table 12 show the sample with greatest Al_2O_3 composition to be also that with the highest interconnected porosity. This is expected since sintering of magnesia-rich spinel compositions has been shown to achieve greater densification than alumina-rich spinel (and thus less pore connectivity) (GANESH, 2013) and doped corundum samples achieve greater density than pure ones for the same sintering conditions (BERRY; HARMER, 1986).

	α-Al_2O_3 (wt%)	MgO (wt%)	$MgAl_2O_4$ (wt%)
60/40	21,94 ± 0,00	19,19 ± 0,70	58,87 ± 1,25
72/28	39,46 ± 0,00	8,23 ± 0,00	54,23 ± 1,76
90/10	84,23 ± 0,00	0,00 ± 0,00	15,77 ± 0,28

Table 12 – Phase compositions of the samples estimated with Rietveld refinement.

5.3.3 SEM images

The final conducted analysis of the samples was SEM imaging. This analysis aimed to evaluate formed pore morphology, i.e. check for the formation of expected dendritic structure and approximate values on pore dimensions. Figures 5.9a, 5.9b, 5.9c show a section of the specimen cut perpendicular to the freezing direction. It can be seen that for all fabricated concentrations, it seems the pore size has approximately the same dimensions, with pore entrance diameters around 30 μm, indicating that the parameters kept constant for all samples (solid loading and freezing temperature)and greater control on pore size than the composition. Nevertheless, the geometry of the pores varies a lot among the presented images, besides also varying greatly internally, demanding large and complex geometry REV for any effort in modelling the structure for microstructure-based modelling. One element that is also seen likely related to the found characteristic lengths is the presence of channels with lengths greater than 100 μm can be seen in all cuts, which could explain the high values in fitted characteristic lengths for all samples.

Figure 5.9d shows the longitudinal cut of the "90/10" sample. This image clearly shows two distinct effects resulting from process parameters: the formation of dendritic pore channels, resulting from the camphene solvent freezing; and pore alignment, indicating the success of unidirectional freezing in its proposed intent of generating aligned pore channels.

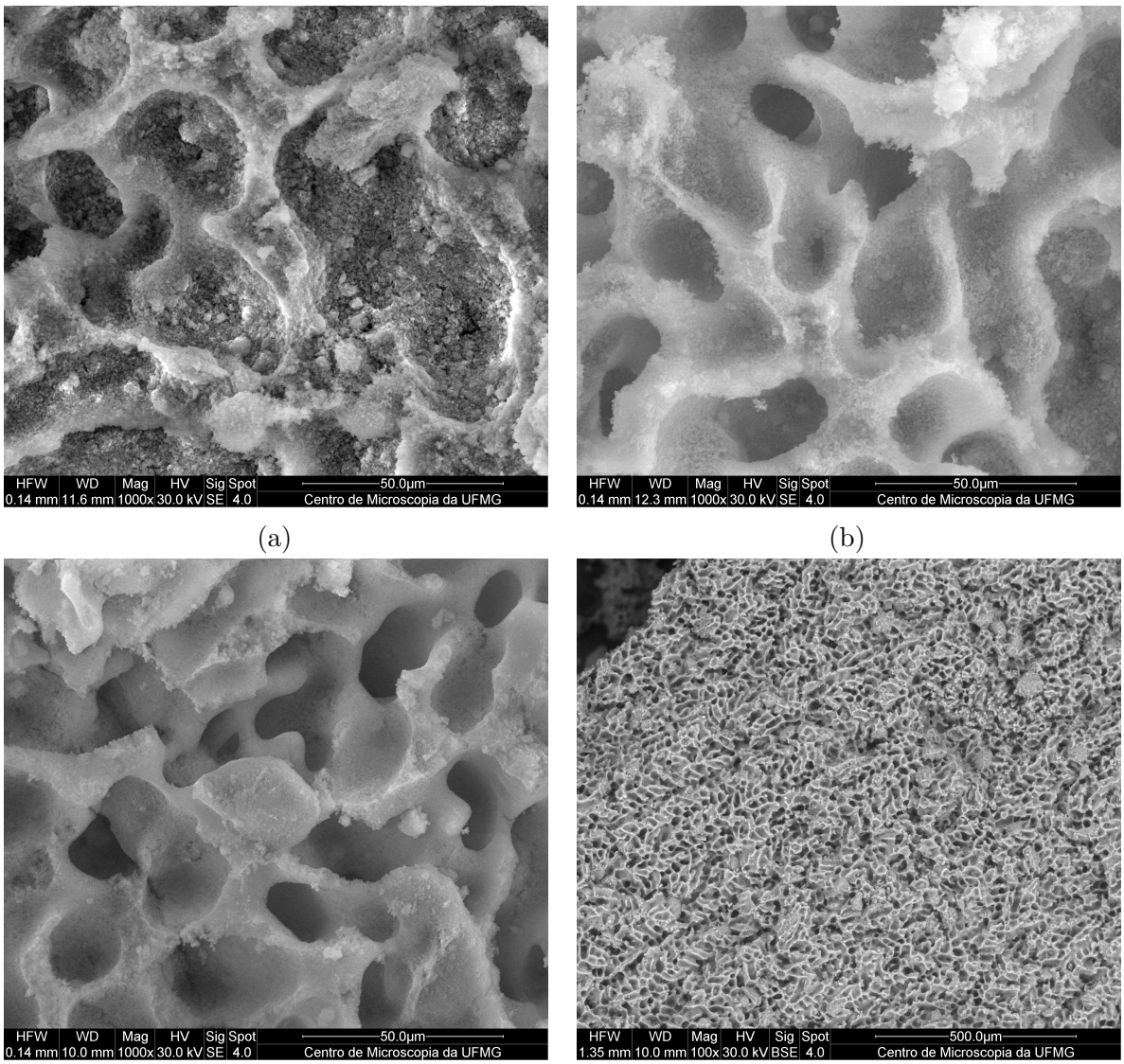

Figure 5.9 – SEM images taken from the camphene samples, with (a) 60/40, (b) 72/28, (c) 90/10 and (d) a longitudinal cut of the bulk of 90/10

One final observation resulting from SEM characterization is the presence of ceramic agglomerates in all samples. The shown structures in Fig. 5.10 were found for every sample analyzed on the microscope, possibly due to poor mixing during slurry preparation, where insufficient shear forces generated in the magnetic stirring were unable to separate naturally formed agglomerates of the starting powders. These can be seen to change the microstructure, forcing the dendritic pore channels to grow around them. Acoustically, this can be associated with the higher tortuosity found for all samples once the pore channels have more complex paths forced to go around them.

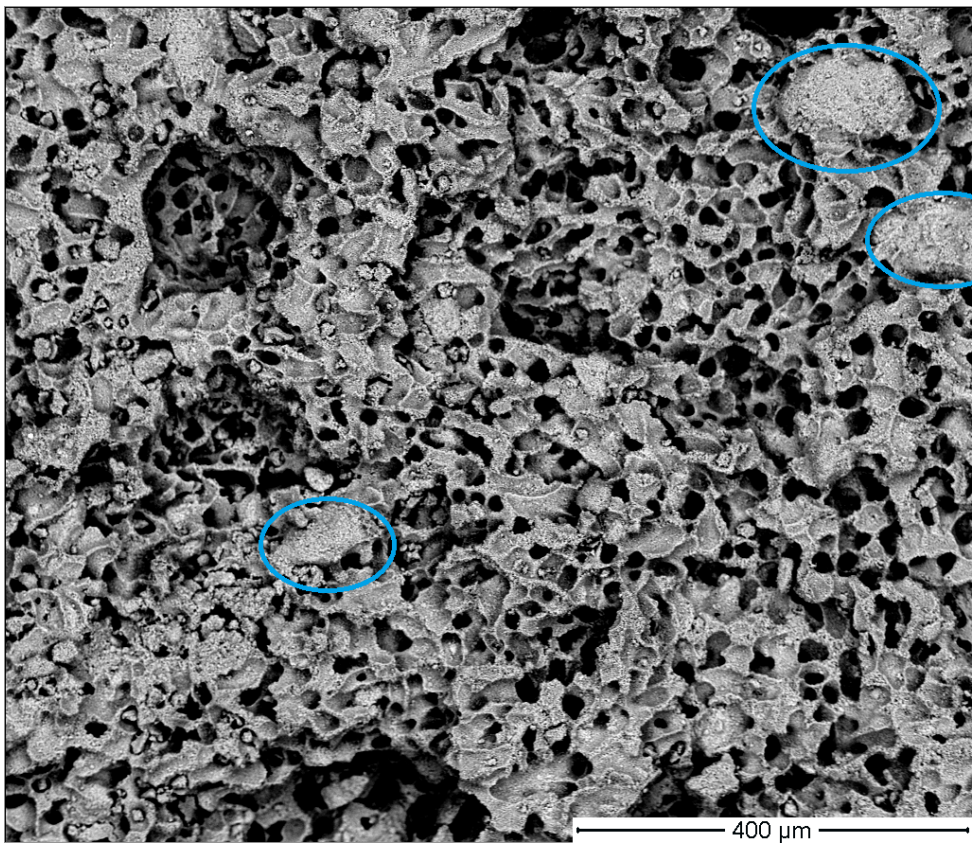

Figure 5.10 – Example of solid agglomerates (marked in blue) found in all samples.

5.4 DMSO-based samples material characterisation

5.4.1 Porosity/acoustic measurements

As presented in Tab. 10, two different solid loadings were tested for the DMSO-based samples associated with three controlled different freezing temperatures. The measured porosities for all DMSO-based samples are shown in Fig. 5.11 (notice that now error bars marking the standard deviations of each quantity are present, as for these samples multiple measurements were done to test the reliability of the Archimedes Principle method). By comparing Figs. 5.11a and 5.11b is noticed that the "70/30" samples all have open and total porosity values nearly 10 % smaller than those of the "80/20" samples. The total porosity is closely related to the solid loading, with the total solid loading practically equal to the obtained final porosity. Further investigation is necessary to investigate the limits of this linear relation between solid loading and final porosity. Another noticeable behaviour is the apparent independence (i.e. very low sensitivity) of final porosity from freezing temperature, given the porosities remained close for all temperatures in both solid loadings.

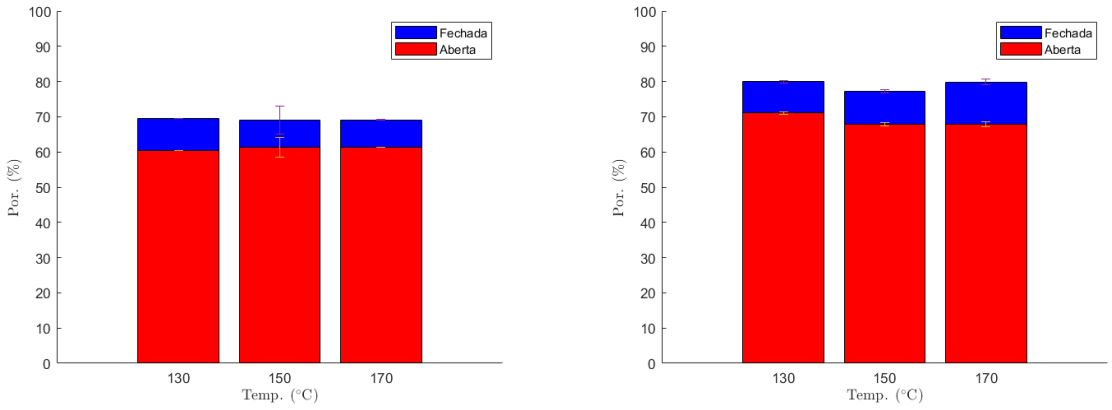

Figure 5.11 – Porosity measurements for the DMSO samples, (a) 70/30 solid loading and (b) 80/20 solid loading.

A factor that may impact impedance measurements is the gap between the sample's lateral sides and its holder inside the impedance tube. Such a gap may create side "leaking", which will influence the sound absorption, possibly creating double porosity effects (JAOUEN; GOURDON; GLé, 2020), and consequently, an (erroneously) improved absorption coefficient. The same procedure performed on the camphene-based samples was conducted on the DMSO-based samples, but with an added final step in which the samples were also wrapped in adhesive tape to mitigate the leaking effect, as shown in Fig. 5.12 and promote a tight fit of the sample in its holder. Though compression of the sample's bulk is an issue for poroelastic materials, given the studied sample's elevated hardness, the adverse effects caused by compression are minimum.

Figure 5.12 – A wrapped sample.

The absorption curves were measured upon properly evaluating the absorption coefficient and are shown in Fig. 5.13. Compared to the camphene samples, the sound absorption coefficient of the DMSO samples has more homogeneous values through the evaluated frequency range. Also, its values are kept relatively high for all frequencies instead of having pronounced peaks in specific regions while achieving low values for the rest of

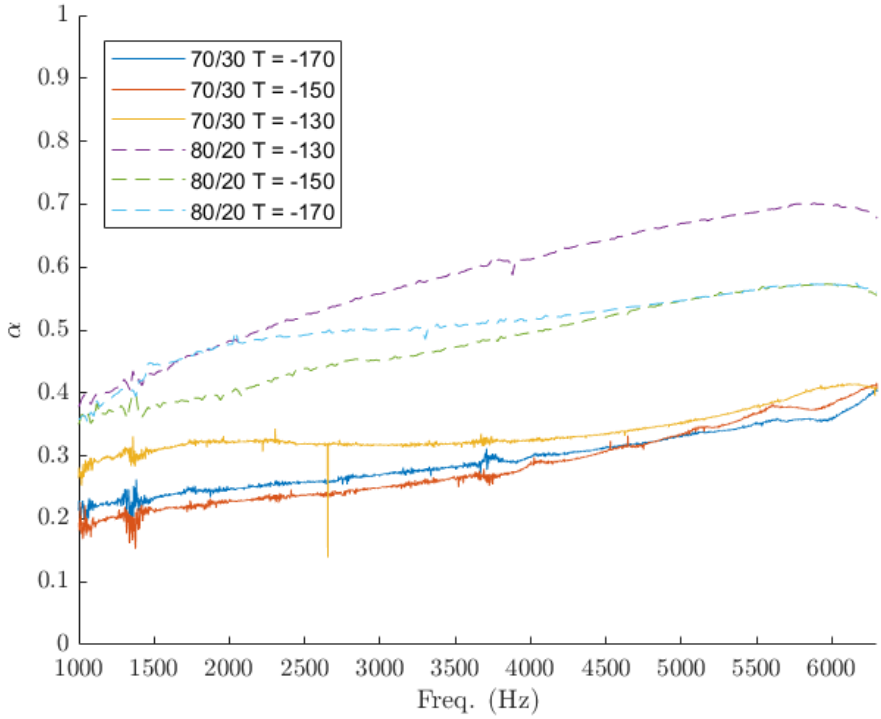

Figure 5.13 – Sound absorption coefficient α for all DMSO-based samples.

the tested frequencies. This continuity on the evaluated parameter applies to all samples, each within its average values. In this case, a clear correlation between a freeze-casting processing parameter and acoustic parameter overall performance is visible. The decrease in solid loading resulted in a decreased sample porosity, and the average sound absorption coefficient is higher for smaller porosities. This was predicted in Section 4.2, where it was shown that all JCAL parameters were kept constant, and a decrease in porosity results in an increase in sound absorption coefficient. For this DMSO-based system, it is thus confirmed that a decrease in solid loading will lead to enhanced sound absorption.

Another arguably visible influence is of freezing temperature. For both solid loadings, "80/20" and "70/30", it can be seen that the highest freezing temperature $T_f = 130°C$ yields the highest valued sound absorption coefficient curves. Different studies have shown a direct pore size dependence on freezing temperature (XU; WANG, 2016; ARAúJO et al., 2018), indicating that lower freezing temperatures will result in smaller average pore sizes due to a greater quantity of nucleated solid crystals resulting from an elevated temperature gradient. Associated with that is the relation between characteristic lengths and sound absorption coefficient pointed out in Section 4.2, where up to a certain value, an increase in viscous characteristic length will increase absorption values, while the increased thermal characteristic length is detrimental, though with little impact. An increase in average pore size will result in increased values of the characteristic lengths, as may be expected from Eqs. 2.27, 2.28, and therefore improved absorption coefficient values. Therefore, in the same way, camphene-based samples were analysed in both orientations relative to the freezing direction (top or bottom facing the sound source, or "top-up"/"bottom-up" for simplicity),

DMSO-based samples were also tested to check for possible grading in sample porosity characteristics. Plots of the curves for both sample orientations and all samples are shown in Fig. 5.14. Two interesting features are seen in these plots, a large difference between absorption behaviour depending on sample orientation, and such difference is reduced for higher solid loading samples. These results indicate a graded pore structure inside the bulk of each sample, and such grading is likely less pronounced for higher solid-loading samples.

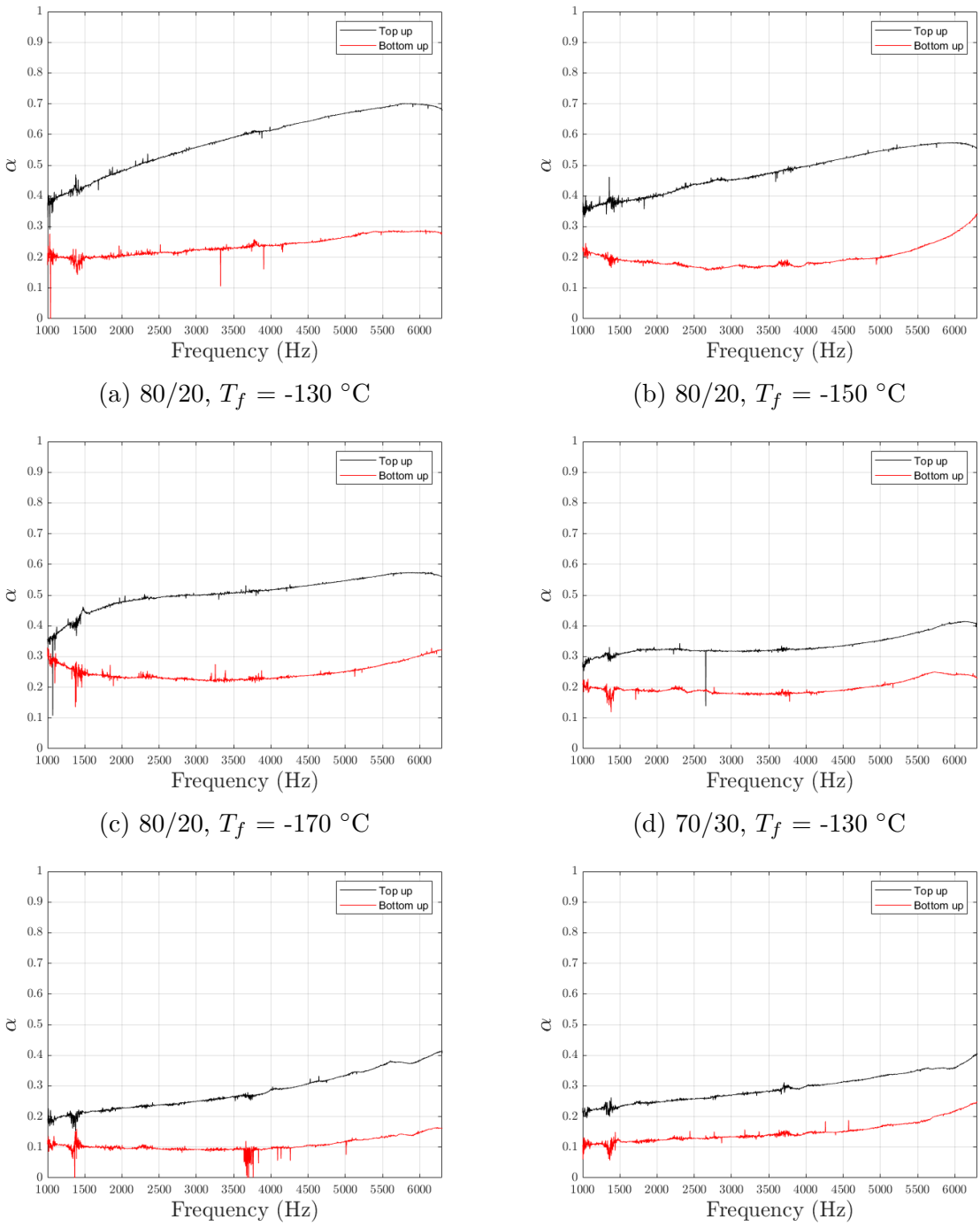

(a) 80/20, T_f = -130 °C

(b) 80/20, T_f = -150 °C

(c) 80/20, T_f = -170 °C

(d) 70/30, T_f = -130 °C

(e) 70/30, T_f = -150 °C

(f) 70/30, T_f = -170 °C

Figure 5.14 – Comparison between the sound absorption coefficients of DMSO-based samples with different orientations.

Despite the good evidence of graded porosity through the sample and seeking

further evidence on the correlation of fabrication parameters, inverse characterization was performed on the obtained impedance curves. For the DMSO-based samples, this model calibration was particularly difficult, and by using deterministic methods, nearly all samples resulted in inconsistent or senseless (complex or negative valued) parameter values. Again, using the "fmincon" function from MatLab's Global Optimization Toolbox, inverse characterisation was performed, and the found parameters and the average relative error (Eq. 5.1) are shown in Table 13. This inverse characterisation was performed on the impedance curves obtained for top-up configuration. The behaviour commented in Section 4.2 of minimizing/maximizing parameters by the used constrained optimization methods to try to match impedance values, especially prevalent in the case of not reachable by single layer models, is seen. Nevertheless, interestingly for the samples whose porosity is not found to be the upper established bound, the porosities follow the same trend of porosity measured using the Archimedes principle, where higher solid loadings will result in reduced porosities. The airflow resistivity is also very high for all samples, regardless of the type of sample or the behavior of the fit applied to its impedance. Although this might be related to the actual physical properties of the samples, as pointed out by Ouisse et al. (2012), the air flow resistivity parameter exerts great influence in impedance values for low and high-frequency ranges. To better understand these trends, the impedance of these samples and the fitted impedance is necessary.

	ϕ	σ (Nsm^{-2})	α_∞	λ (μm)	λ' (μm)	k_0' (m^2)	error (%)
80/20 T_f = -130 °C	0.99	376930	1	15.78	15.78	$999.9{\cdot}10^{-10}$	3.25
80/20 T_f = -150 °C	0.60	415890	2.75	78.10	282.09	$14.1{\cdot}10^{-10}$	7.55
80/20 T_f = -170 °C	0.70	377250	1	17.25	164.08	$9.9{\cdot}10^{-10}$	9.1
70/30 T_f = -130 °C	0.31	442480	1.06	10.48	400	$5.7{\cdot}10^{-10}$	10.58
70/30 T_f = -150 °C	0.99	1977100	1	10.00	10	$100.0{\cdot}10^{-10}$	12.95
70/30 T_f = -170 °C	0.28	548150	1	400.00	400	$1.0{\cdot}10^{-10}$	8.88

Table 13 – Found parameters from inverse characterization applied to DMSO-based samples.

Figure 5.15 shows the experimental and numerically fitted normalized impedance curves relative to Tab. 13. For all presented impedance curves, the fit curves again match the trends of the experimental points and have a decent agreement in value. Going back to the issue of very high fitted resistivities and the fit porosity apparent agreement with the physically measured porosities, Fig. 5.16 shows the effect of variation of the parameter ϕ on the surface impedance according to the JCAL model, while Fig. 5.17 presents the influence of resistivity σ. Though the influence of porosity in the imaginary part of the impedance is low, it clearly raises the values of the real part throughout the evaluated frequency range as it gets lower. The resistivity, on the other hand, raises the real part's average value as it gets higher while lowering the imaginary part's average value. It can also be seen that the impedance trend (smoothly going from higher modules for both parts to lower modules with no peaks) found in the experimental values is also closer to that found for higher resistivity values. Thus, the obtained fitted values are likely resulting from

a combination of the trends set by these parameters, while the experimentally obtained high impedance values through the frequency ranges may be interpreted as indicative of lower effective porosities and higher resistivities.

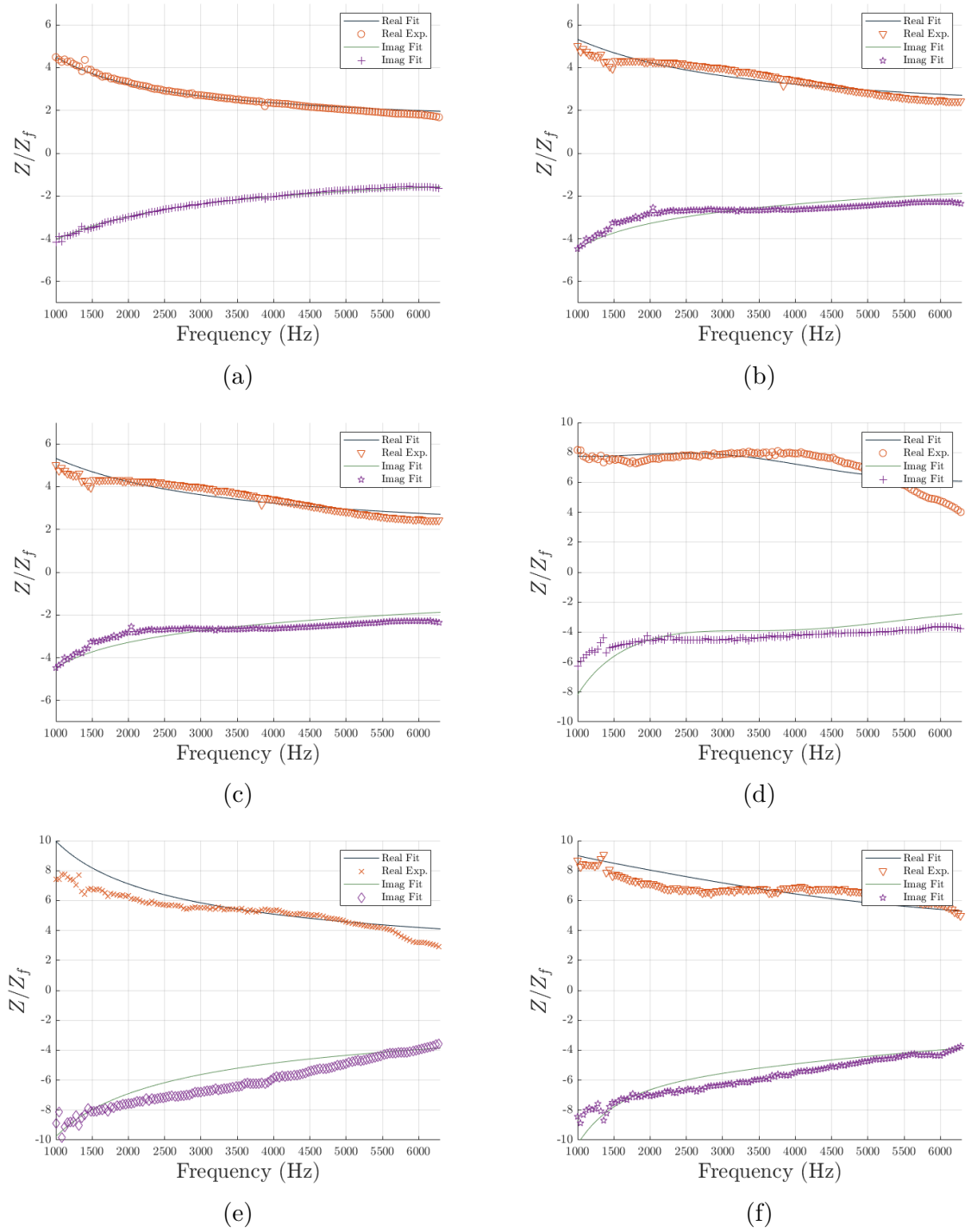

Figure 5.15 – Experimental and numerically fit impedance curves of the DMSO-based samples, where the sample‘s solid loading and freezing temperature are (a)80/20, T= -130 °C, (b)80/20, T= -150 °C, 80/20, T= -170 °C, (d) 70/30, T= -130 °C, (e) 70/30, T= -150 °C, (f) 70/30, T= -170 °C.

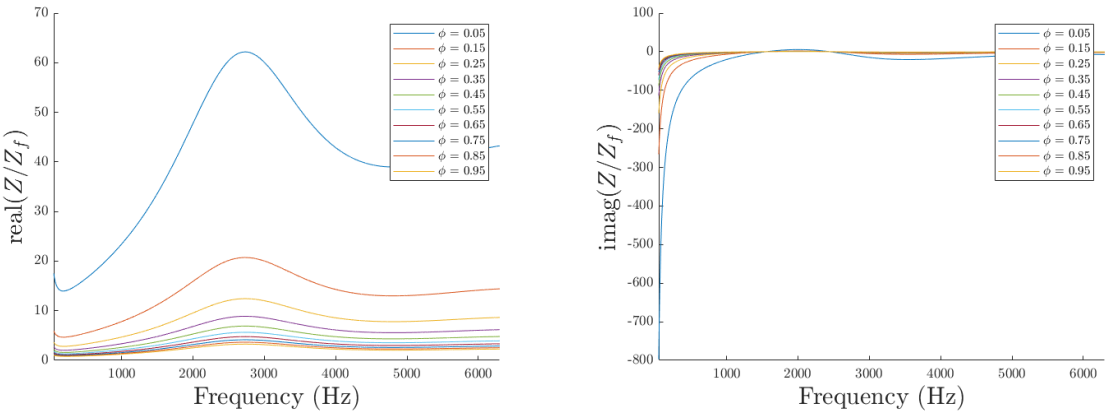

(a) (b)

Figure 5.16 – The influence of varying porosity ϕ on the (a) real and (b) imaginary part of impedance using the JCAL model.

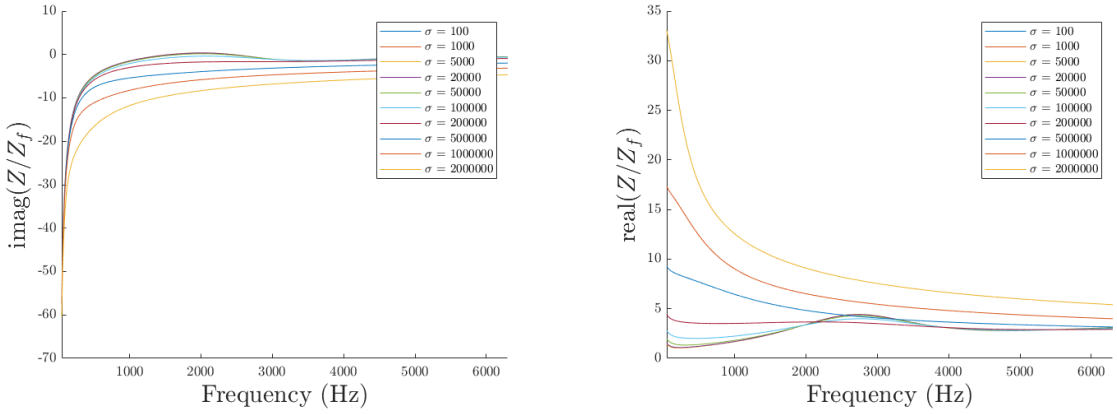

(a) (b)

Figure 5.17 – The influence of varying air flow resistivity σ on the (a) real and (b) imaginary part of impedance using the JCAL model.

5.4.2 SEM and μ-CT experimental results

For the DMSO samples, in addition to the conventional samples, we obtained μ-CT images for some of the samples. A picture of a sample set for characterization using this method is shown in Fig. 5.19. μ-CT is a powerful method that extracts images of a sample's microstructure using x-ray and reconstructs the structure from these images, giving both two-dimensional cuts of the microstructure and three-dimensional reconstructions of the evaluated volume. Unfortunately, not all samples could be characterized by these image methods, though the main results obtained are presented.

Figure 5.18 shows the SEM images from the top surfaces (perpendicular to freezing direction) of three different samples, all built using "80/20" solid loading, each one for a different temperature. Notice that most images present a blurring effect inside the pore regions. The studied ceramics are poor electrical conductors and need to have their

surface covered by a very reduced thickness layer of conducting material (e.g. gold) via sputtering in the metalization process. For our samples, carbon was used as conducting material for metalization. The blurring effect is owing to the pore depth that stems from the metalization of its internal walls, causing charge accumulation in those regions and disrupting the obtained images. Whereas the outer surfaces are clear in the images, only the internal walls are blurred.

In Fig. 5.18, it can be seen that the formed pores are lamellar, contrasting to the structures found in Chu et al. (2015), where honeycomb geometries were obtained. This may be due to the material employed in this work (Chu et al. use a polymer) and the lower solid loading used in their study. Nonetheless, it can be seen that at some points of the pores, sharp hexagon-like geometries are formed, indicating that the solid crystals formed in our samples are similar to those formed in their study. These found pore geometries are complex and varying, aspects that certainly influence all acoustic parameters apart from porosity.

Additionally, pore entrance size measurements can be seen in Figs. 5.18a, 5.18b, 5.18c. For all three samples, pores with entrances around 50 μm height can be seen, while their width can be much longer. Another noticeable aspect of all samples is the rugosity in pore walls. Rough pore surfaces have been studied using idealized slit geometries representing roughness, and though some studies show little influence of idealized rough geometries over parameters used in Eq. 2.22 (CORTIS et al., 2003), other studies show that pore roughness may affect directly specific parameters (SONG et al., 2017) or overall sound absorption performance (ACHDOU; AVELLANEDA, 1992; ZIELINSKI et al., 2020). Therefore it is expected that this characteristic for all samples influenced the presented absorption coefficients.

Proceeding to the μ-CT images, Fig. 5.20d shows the reconstructed transversal cut of the 80/20 T_f = -130 °C sample. This method consists on the production of multiple x-ray images from different angles of a sample. The obtained images are computationally processed, producing transverse "slices" of the sample's microstructure in three planes. As seen in Fig. 5.20d, a very interesting feature is the graded porosity structure. This was not visible from SEM images due to their reduced area of focus, but the tomography images allow the visualization of the whole sample microstructure (despite a reduced resolution compared to SEM).

This grading is more clearly visible in the transversal cuts taken perpendicular to the freezing direction. Here, a dense bottom layer can be seen (Fig. 5.20a), followed by an intermediate porosity mid-section (Fig. 5.20b) a high porosity top (Fig. 5.20c). It is interesting to notice the lamellar structure in Figs. 5.20b, 5.20c that closely resembles the pore shapes seen in Fig. 5.18d.

Additional to the imaging done using μ-CT, the Amira-Avizo software (SCIENTIFIC,) was used to further analyze the obtained structures. This software enables the

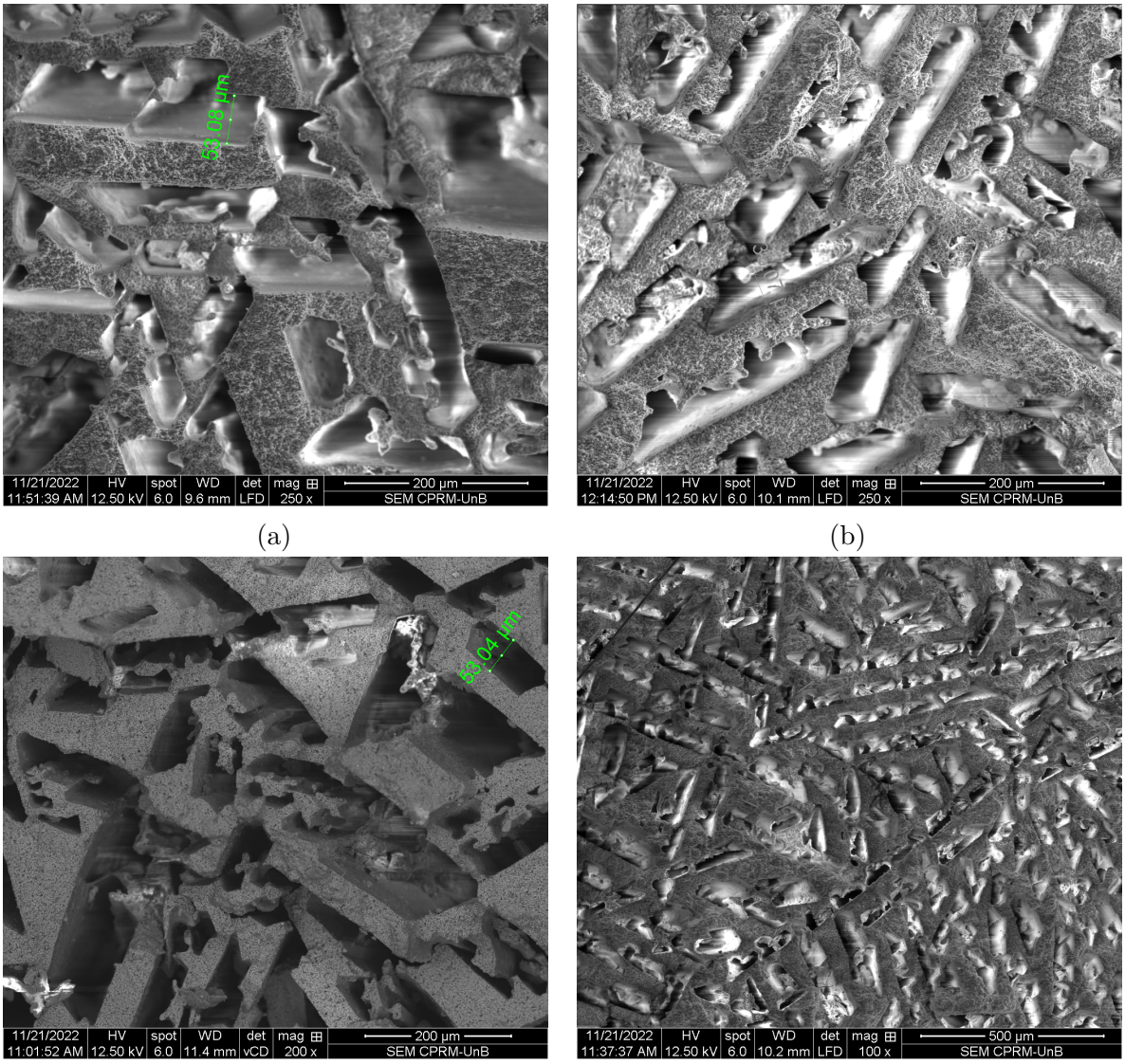

(a) (b)

(c) (d)

Figure 5.18 – SEM images from the DMSO-based samples top surfaces (a) T_f = -130 °C, (b) T_f = -150 °C, (c) T_f = -170 °C, (d) wide view/T_f = -150 °C.

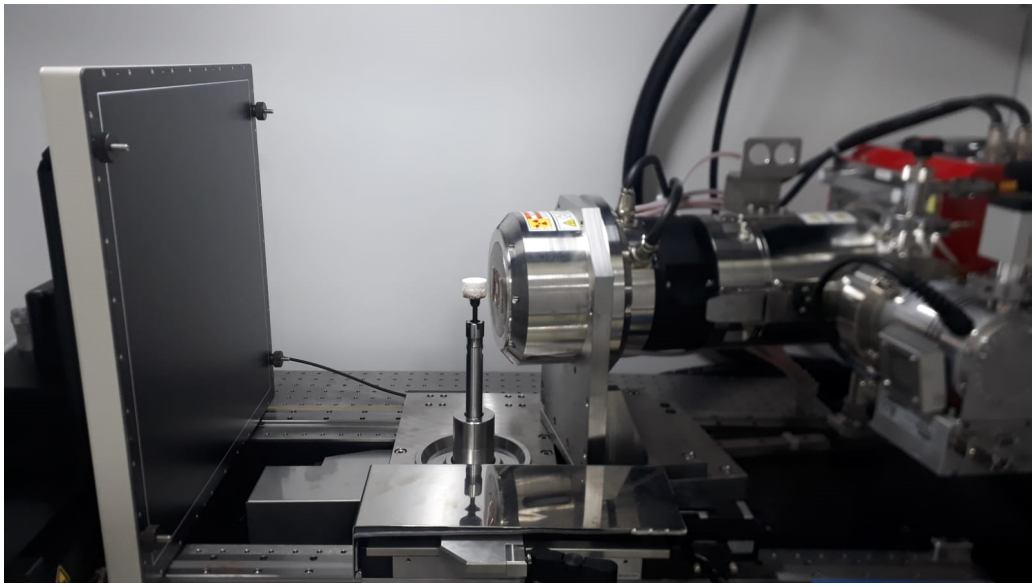

Figure 5.19 – Sample positioned inside μ-CT for analysis.

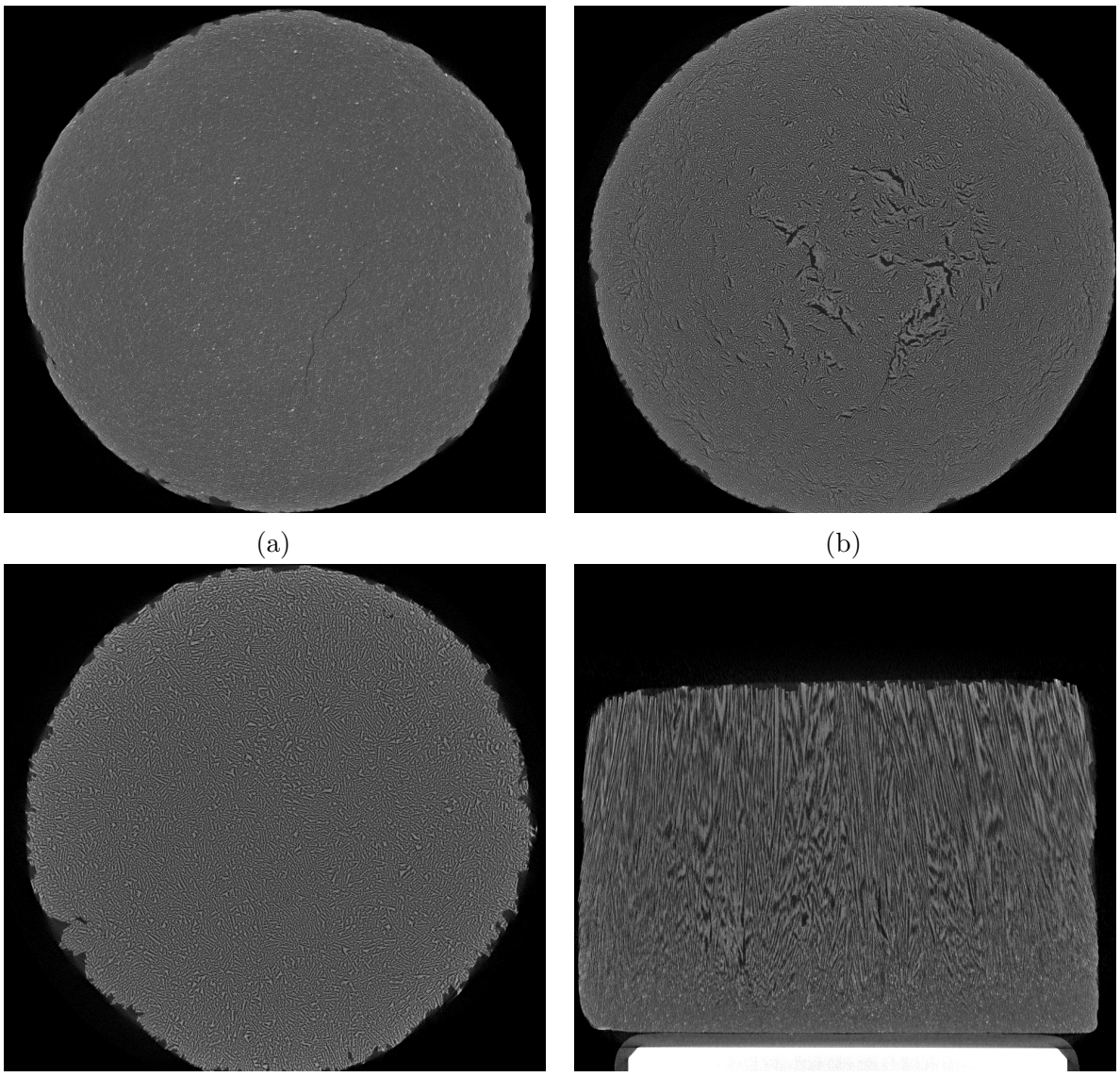

Figure 5.20 – μ-CT images from the DMSO-based samples top surfaces (a) dense bottom, (b) intermediate porosity middle region, (c) High porosity top, (d) Full sample transversal slice.

user to generate digital three-dimensional solid models of samples from the reconstructed image slices. These generated models can then be used to perform different simulations on the material structure.

For our study, we used the XPoreNetworkModelling Extension of the Amira-Avizo software. This extension enables the user to evaluate parameters related to fluid flow through porous media, mainly permeability, and tortuosity. The equations and methods used to obtain such properties, and further descriptions of the extension are presented in Annex A. These analyses made available by the extension are performed on the three-dimensional models generated for the pore channels. In order to obtain the models, the generated slices are subjected to "thresholding", where limits for pixel clarity value are established as representing either material or void. Then, the information obtained from these slices is computed as a solid. From thresholding only it is already possible to obtain

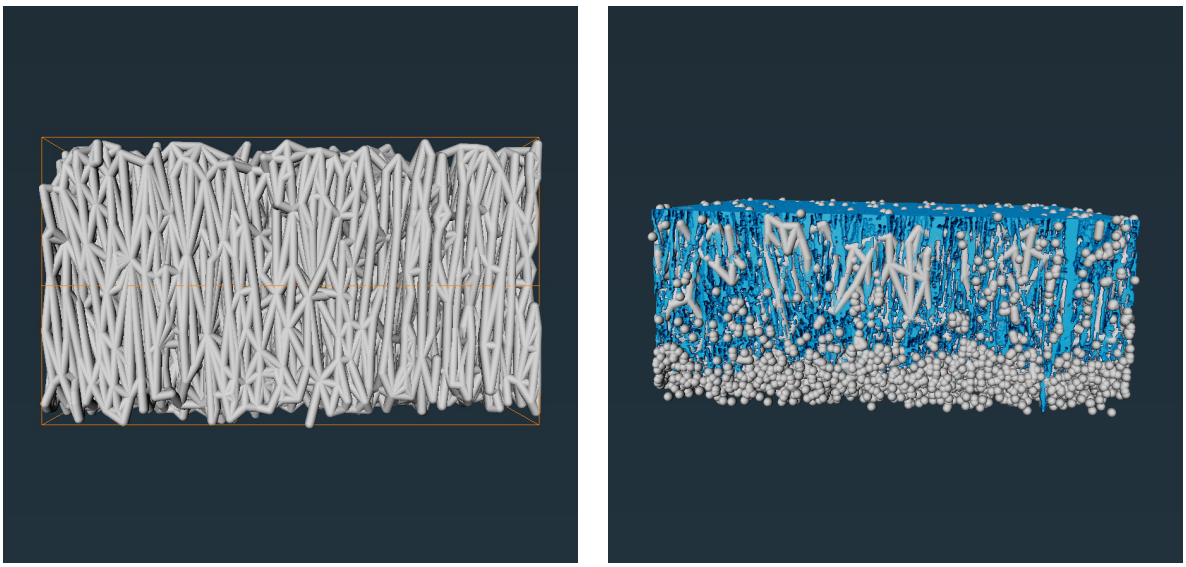

(a) (b)

Figure 5.21 – (a) The generated pore network model for the top layer and (b) the generated pore network model superimposed over the original bottom pore channels model.

an estimate of the sample porosity, where the software computes the ratio between the volume occupied by material and by void inside the total model volume. A bounding box may be used to properly enclose the total volume.

Figure 5.21 shows the generated models used for flow parameter evaluation. As the microstructure grading is made clear in the whole sample image (Fig. 5.20d), we divided the sample into three layers to study their properties. The approximate division in height and the generated pore channel models are shown in Fig. 5.22. Mainly for the bottom layer, it is noticeable that towards the base the pores get more scarce, as the density of the material increases.

To show the pore network model generated using the mentioned extension, Fig. 5.21 shows the generated pore network model for the top layer and also for the bottom layer. These show a limitation of the software, that is, it models pores as spheres and connections between them as cylinders. These spheres and cylinders will have dimensions representative of the pore morphology, though they are limited geometrically, thus affecting the accuracy of the generated model. In Fig. 5.21b it can be seen that isolated pores not connected to the pore network are represented by spheres and are plentiful in the bottom region since it is a nearly dense region; whereas Fig. 5.21a shows an intricate network of cylinders and fewer spheres, indicating its improved connectivity and also its greater porosity.

Table 14 presents the parameters measured by the extension to which layer. It can be seen that the porosity gradually decreases with similar porosities for the top and mid regions, as expected. Permeability also decreases for each layer, though tortuosity is measured to be the lowest in the middle region. This might be related to pore geometry

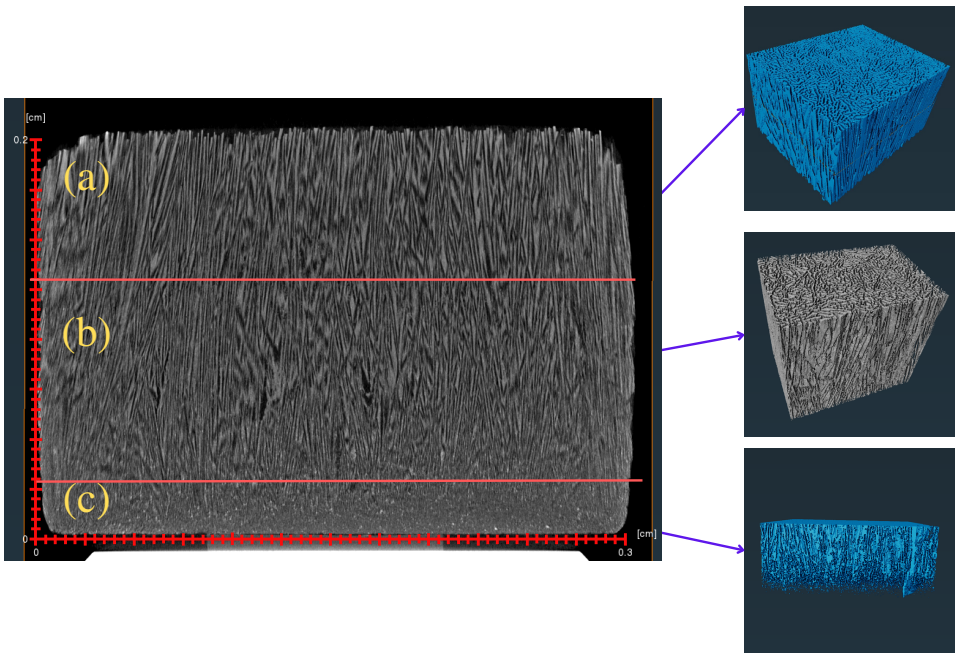

Figure 5.22 – μ-CT transversal cut of the 80/20 T_f =-130 °C sample with the generated pore channels models using Amira Avizo software, where (a) is the top layer with greater porosity, (b) the intermediate porosity layer and (c) the dense bottom.

Layer	Porosity	Permeability (μm^2)	Tortuosity
Top	0.66	7.7678	1.250
Mid	0.51	4.3783	1.196
Bottom	0.22	0.05848	1.311

Table 14 – Modelled pore network model parameters.

Layer	λ (μm)	λ' (μm)	k_0' (m^2)
Top	150	200	$20{\cdot}10^{-10}$
Mid	150	200	$20{\cdot}10^{-10}$
Bottom	20	30	$5\cdot10^{-10}$

Table 15 – Heuristically defined parameters for the modelled material sample.

differences between top and mid regions, nonetheless, it may be simply computational differences given the small differences between found values. Notice that permeability is given in μm^2. To calculate the impedance using this data, this permeability was converted to resistivity using Eq. 2.26.

To model the impedance and sound absorption of the material using the modeled pore channels, an approximate division in height was done to the total sample height: it was measured as having a total height $h = 20$ mm, so both the top and midsection were divided as having $h = 9$ mm and the bottom layer to have $h = 2$ mm. In order to model this material sample using JCAL model, the left parameters (characteristic lengths and static thermal permeability) were heuristically defined and are shown in Tab. 15.

Finally, the obtained impedance and sound absorption coefficients are shown in Fig. 5.23. It is clear that the absorption coefficient has lower values than those obtained

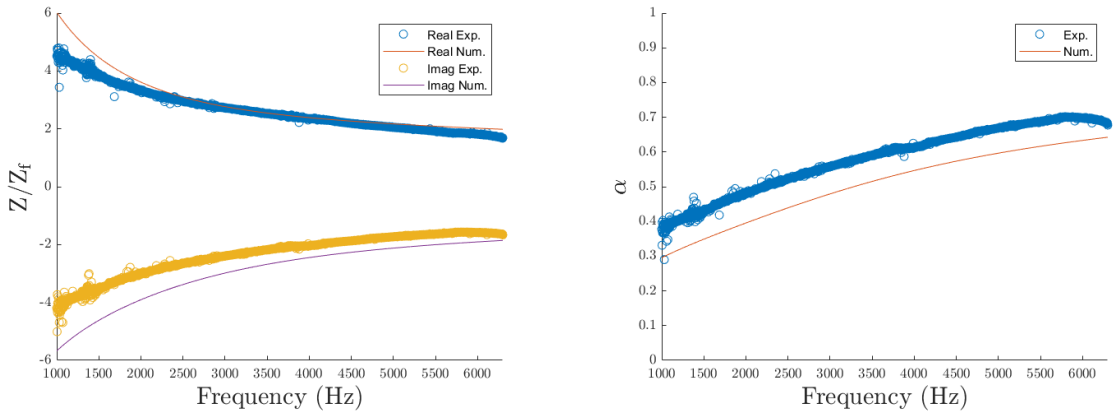

(a) (b)

Figure 5.23 – Experimentally obtained and model estimated (a) impedance curves and (b) sound absorption coefficient curves for the 80/20, T_f = -130 °C sample.

experimentally for all the evaluated frequencies. In spite of this difference in value, the general trend of the curves is the same: no clear peak in the evaluated frequency range with growth in coefficient value from start to finish. The impedance curves also present same behavior for both model-based and experimental curves, besides having close values. As discussed in Sec. 5.3.1, these impedance values are likely related to the very high resistivity and relatively low porosities of these samples. Here, the disagreement between experimental and numerical curves can have various different origins, the simpler explanations being related to accuracy of the parameter values through software models, or to the approximations done in such an estimation.

An interesting explanation to this disagreement, though, might be double porosity effects on sound absorption. This type of structure is constituted by materials with continuous interfaces between regions of pore channels with high contrast in pore size and permeability, and it has been shown to improve acoustic absorption in different frequency ranges (SGARD et al., 2005). Besides the very complex pore structure obtained for the produced samples already shown, pores of different dimensions are visible in some points of samples, as seen in Fig. 5.20b. These contrasting pore morphologies inside the sample microstructure may cause pressure diffusion effects (the main mechanism related to changes caused by double-porosity in absorption coefficient) and consequently affect the absorption behavior of the samples. For this hypothesis to be tested, future studies are necessary related to pore size distribution and produced pore morphology grading.

Finally, for comparison purposes, the properties shown in Tables 14 and 15 were used to obtain the sound absorption coefficient of idealised equivalent single material samples, that is, the properties of each individual layer were used as if it were from a material layer with the same height as the total sample height (h = 20 mm) and then applied to calculate the absorption coefficient α of these idealised samples. This was done to verify whether the pore structure grading had an overall positive effect in raising the absorption coefficient value when compared to a material with the same set of properties

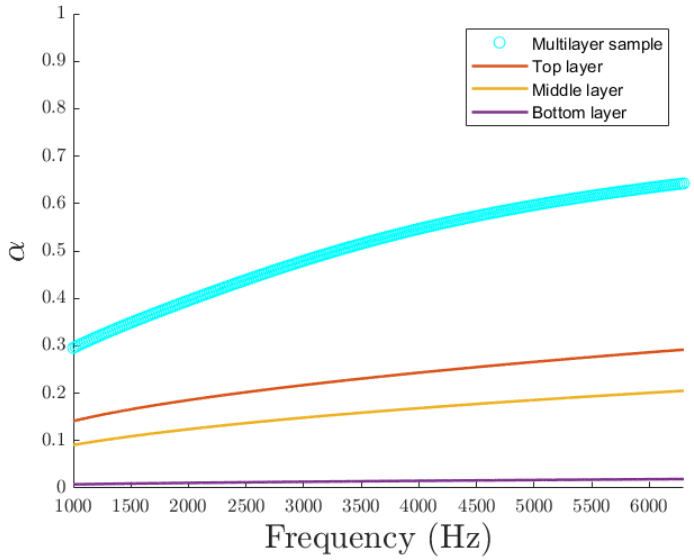

Figure 5.24 – Comparison between sound absorption coefficient of the graded structure and equivalent samples with the properties of measured individual layers.

as the top, bottom or middle layer. Figure 5.24 shows the absorption coefficient curves for each equivalent sample. It can be seen that throughout the studied frequency range, the sound absorption of the graded porosity sample has greater values than the individual isolated layers. More interesting, the idealized sample using bottom layer properties has extremely low values for the absorption, due mainly to its extremely high air flow resistivity of it.

6 Conclusion

6.0.1 Dissertation conclusions

Porous ceramic materials have recently gained greater attention as a sound absorption solution for their unique characteristics combined with good sound absorption coefficients. In this sense, in the present work porous ceramic samples were produced and their acoustic properties were studied, aiming at adding to the pool of options for absorbers. Acoustic characterization was done using the JCAL model, which was studied theoretically, numerically and experimentally.

Freeze-casting was chosen as the route for fabrication of porous ceramics due to is versatility in attainable final sample characteristics and control of porosity/pore morphology through process parameter variation. For the same starting powders in different ratios, two solvents were used. For both solvents, ceramic samples were successfully produced and achieved good sound absorption coefficients in all cases. Control of some of the material related characteristics, mainly for the camphene-based samples, fell short from expectations, with phase formation turning out different from planned.

Using mainly inverse characterization methods associated to the surface impedance of different samples evaluated experimentally, analysis of sample microstructure relation to acoustic parameters was performed. The relations between fitted parameter and sample properties (mainly phase composition) for the camphene-based samples were not clear, besides the fitted porosities having values $\phi \approx 0.20$, while direct measurements showed $\phi \approx 0.65$. In the case of DMSO-based samples, no fitting using the JCAL model was achieved for most samples, though evident relations were found between freeze-casting parameters and final acoustic absorption performance. The clearest relation was the lower solid loading resulting in overall higher sound absorption coefficients. Additionally, it was also shown that the DMSO-based samples had a graded-porosity microstructure and it was also shown that this grading resulted in improved sound absorption coefficients when compared to single layer materials with properties equal to that of the individual graded-sample layers.

Therefore, the originally proposed goals were achieved. Porous ceramics samples were produced and have been shown to be a promising class of absorbers. Additionally, different categories of theoretical models were presented and the widely used JCAL model

was given deeper review. Finally, the relations discussed between fabrication parameters and acoustic behavior are a starting point for future studies in deeper understanding and optimization of porous ceramics.

6.0.2 Suggestion for Future Works

Some suggestions for future works are:

1. Produce a study dedicated to the economic viaibility of employment of freeze-casting to produce ceramic porous sound absorbers;
    - Study options to decrease process cost and improve scalability, e.g. cheaper solvents, lower necessary sintering temperatures;
2. Evaluate thermal properties such as shock resistance, and isolation of the produced samples;
3. Produce samples using different freezing gradient alignments (e.g. radial, multi-directional) and verify influence over sound absorption properties;
4. Study of mechanical resistance characteristic of ceramic samples produced following the route proposed in the present work;
5. Direct characterization of acoustic parameters of produced samples using methods found in literature;

References

ACHDOU, Y.; AVELLANEDA, M. Influence of pore roughness and pore-size dispersion in estimating the permeability of a porous medium from electrical measurements. *Physics of Fluids A: Fluid Dynamics*, v. 4, n. 12, p. 2651–2673, 1992. Disponível em: <https://doi.org/10.1063/1.858523>. Citado na página 72.

ALLARD, J. F. *Propagation of Sound in Porous Media*. Springer Netherlands, 1993. Disponível em: <https://doi.org/10.1007/978-94-011-1866-8>. Citado na página 5.

ALLARD, J. F.; ATALLA, N. *Propagation of Sound in Porous Media: Modelling Sound Absorbing Materials*. [S.l.]: John Wiley & Sons, Ltd, 2009. Citado 17 vezes nas páginas xi, xii, 1, 10, 11, 13, 14, 15, 17, 21, 22, 24, 25, 46, 48, 49, and 51.

ALLARD, J. F. et al. Evaluation of tortuosity in acoustic porous materials saturated by air. *Review of Scientific Instruments*, v. 65, n. 3, p. 754–755, 1994. Disponível em: <https://doi.org/10.1063/1.1145097>. Citado na página 20.

ANDREI, N. *Modern numerical nonlinear optimization*. [S.l.]: Springer International Publishing AG, 2022. Citado na página 45.

ARAKI, K.; HALLORAN, J. W. Room-temperature freeze casting for ceramics with nonaqueous sublimable vehicles in the naphthalene-camphor eutectic system. *Journal of the American Ceramic Society*, v. 87, p. 2014–2019, 2004. ISSN 00027820. Citado 2 vezes nas páginas 28 and 32.

ARAúJO, G. T. et al. Preparation of al2o3 and mgal2o4-based samples with tailored macroporous structures. *Ceramics International*, v. 44, n. 1, p. 580–587, 2018. ISSN 0272-8842. Disponível em: <https://www.sciencedirect.com/science/article/pii/S0272884217321570>. Citado 6 vezes nas páginas 7, 27, 28, 30, 62, and 67.

ASTM INTERNATIONAL. *ASTM C522-03*: Standard test method for airflow resistance of acoustical materials. West Conshohocken, PA, 2016. Citado na página 19.

ASTM INTERNATIONAL. *ASTM B962-15*: Standard test methods for density of compacted or sintered powder metallurgy (pm) products using archimedes' principle. West Conshohocken, PA, 2017. Citado na página 35.

ASTM INTERNATIONAL. *ASTM C373-18*: Standard test methods for determination of water absorption and associated properties by vacuum method for pressed ceramic tiles and glass tiles and boil method for extruded ceramic tiles and non-tile fired ceramic whiteware products. West Conshohocken, PA, 2018. Citado na página 35.

ATALLA, Y.; PANNETON, R. Inverse acoustical characterization of open cell porous media using impedance tube measurements. *Canadian Acoustics - Acoustique Canadienne*, v. 33, p. 11–24, 2005. ISSN 07116659. Citado 4 vezes nas páginas 16, 21, 22, and 37.

ATTENBOROUGH, K. Acoustical characteristics of rigid fibrous absorbents and granular materials. *The Journal of the Acoustical Society of America*, Acoustical Society of America (ASA), v. 73, n. 3, p. 785–799, mar. 1983. Disponível em: <https://doi.org/10.1121/1.389045>. Citado na página 5.

ATTENBOROUGH, K. Acoustical characteristics of rigid fibrous absorbents and granular materials. *The Journal of the Acoustical Society of America*, v. 73, n. 3, p. 785–799, 1983. Disponível em: <https://doi.org/10.1121/1.389045>. Citado na página 9.

BAI, H. et al. Bioinspired large-scale aligned porous materials assembled with dual temperature gradients. *Science Advances*, v. 1, n. 11, p. e1500849, 2015. Disponível em: <https://www.science.org/doi/abs/10.1126/sciadv.1500849>. Citado na página 29.

BERANEK, L. L. Acoustic impedance of porous materials. *The Journal of the Acoustical Society of America*, v. 13, p. 248–260, 1 1942. ISSN 0001-4966. Disponível em: <http://asa.scitation.org/doi/10.1121/1.1916172>. Citado na página 18.

BERANEK, L. L. Acoustical properties of homogeneous, isotropic rigid tiles and flexible blankets. *The Journal of the Acoustical Society of America*, v. 19, n. 4, p. 556–568, 1947. Disponível em: <https://doi.org/10.1121/1.1916521>. Citado 2 vezes nas páginas 4 and 18.

BERRY, K. A.; HARMER, M. P. Effect of mgo solute on microstructure development in al2o3. *Journal of the American Ceramic Society*, v. 69, p. 143–149, 2 1986. ISSN 0002-7820. Disponível em: <https://onlinelibrary.wiley.com/doi/10.1111/j.1151-2916.1986.tb04719.x>. Citado 2 vezes nas páginas 34 and 62.

BERRYMAN, J. G. Confirmation of biot's theory. *Applied Physics Letters*, v. 37, n. 4, p. 382–384, 1980. Disponível em: <https://doi.org/10.1063/1.91951>. Citado na página 46.

BIOT, M. A. Theory of propagation of elastic waves in a fluid-saturated porous solid. i. low-frequency range. *The Journal of the Acoustical Society of America*, v. 28, n. 2, p. 168–178, 1956. Citado na página 2.

BIOT, M. A. Theory of propagation of elastic waves in a fluid-saturated porous solid. ii. higher frequency range. *The Journal of the Acoustical Society of America*, v. 28, n. 2, p. 179–191, 1956. Disponível em: <https://doi.org/10.1121/1.1908241>. Citado na página 2.

BONFIGLIO, P.; POMPOLI, F. Inversion problems for determining physical parameters of porous materials: Overview and comparison between different methods. *Acta Acustica united with Acustica*, v. 99, p. 341–351, 5 2013. ISSN 16101928. Citado 3 vezes nas páginas 21, 37, and 38.

BOTTERMAN, B. et al. Characterizing and modelling the sound absorption of wood wool cement boards (wwcb). In: . [S.l.: s.n.], 2016. Citado na página 21.

BOULVERT, J. et al. Optimally graded porous material for broadband perfect absorption of sound. *Journal of Applied Physics*, v. 126, n. 17, p. 175101, 2019. Disponível em: <https://doi.org/10.1063/1.5119715>. Citado na página 9.

BOUTIN, C.; GEINDREAU, C. Estimates and bounds of dynamic permeability of granular media. *The Journal of the Acoustical Society of America*, v. 124, n. 6, p. 3576–3593, 2008. Disponível em: <https://doi.org/10.1121/1.2999050>. Citado na página 61.

BRAULIO, M. A. et al. Spinel-containing alumina-based refractory castables. *Ceramics International*, Elsevier Ltd, v. 37, p. 1705–1724, 2011. ISSN 02728842. Citado na página 35.

BROWN, R. J. S. Connection between formation factor for electrical resistivity and fluid-solid coupling factor in biot's equations for acoustic waves in fluid-filled porous media. *GEOPHYSICS*, v. 45, n. 8, p. 1269–1275, 1980. Disponível em: <https://doi.org/10.1190/1.1441123>. Citado na página 19.

BRUNEAU, M.; POTEL, C. *Materials and acoustics handbook*. [S.l.]: ISTE, 2009. Citado na página 22.

CALLISTER, W. D.; RETHWISCH, D. G. *Materials science and engineering: An introduction*. [S.l.]: Wiley, 2020. Citado 2 vezes nas páginas xi and 34.

CAO, L. et al. Fire-resistant and hierarchically structured elastic ceramic nanofibrous aerogels for efficient low-frequency noise reduction. *Nano Letters*, American Chemical Society, v. 22, p. 1609–1617, 2 2022. ISSN 15306992. Citado na página 6.

CARLESSO, M. et al. Near-net-shaped porous ceramics for potential sound absorption applications at high temperatures. *Journal of the American Ceramic Society*, v. 96, n. 3, p. 710–718, 2013. Disponível em: <https://ceramics.onlinelibrary.wiley.com/doi/abs/10.1111/jace.12160>. Citado na página 5.

CHAMPOUX, Y.; ALLARD, J. Dynamic tortuosity and bulk modulus in air-saturated porous media. *Journal of Applied Physics*, v. 70, n. 4, p. 1975–1979, 1991. Disponível em: <https://doi.org/10.1063/1.349482>. Citado 4 vezes nas páginas 6, 13, 16, and 46.

CHAMPOUX, Y. et al. Air-based system for the measurement of porosity. *The Journal of the Acoustical Society of America*, v. 89, p. 910–916, 2 1991. ISSN 0001-4966. Disponível em: <http://asa.scitation.org/doi/10.1121/1.1894653>. Citado na página 18.

CHAZOT, J.-D. et al. Acoustical and mechanical characterization of poroelastic materials using a bayesian approach. *The Journal of the Acoustical Society of America*, Acoustical Society of America (ASA), v. 131, p. 4584–4595, 6 2012. ISSN 0001-4966. Citado na página 37.

CHEN, J. et al. Sound absorption performance of a lightweight ceramic foam. *Ceramics International*, v. 46, n. 14, p. 22699–22708, 2020. ISSN 0272-8842. Disponível em: <https://www.sciencedirect.com/science/article/pii/S0272884220316795>. Citado na página 5.

CHEN, Y. et al. Porous ceramics: Light in weight but heavy in energy and environment technologies. *Materials Science and Engineering: R: Reports*, v. 143, p. 100589, 2021. ISSN 0927-796X. Disponível em: <https://www.sciencedirect.com/science/article/pii/S0927796X20300474>. Citado 3 vezes nas páginas 1, 3, and 26.

CHENG, Y. et al. The influence of closed pore ratio on sound absorption of plant-based polyurethane foam using control unit model. *Applied Acoustics*, Elsevier Ltd, v. 180, p. 108083, 2021. ISSN 1872910X. Disponível em: <https://doi.org/10.1016/j.apacoust.2021.108083>. Citado na página 61.

CHENG, Z. et al. Structure control of hydroxyapatite ceramics via an electric field assisted freeze casting method. *Ceramics International*, v. 41, n. 7, p. 8599–8604, 2015. ISSN 0272-8842. Disponível em: <https://www.sciencedirect.com/science/article/pii/S0272884215004745>. Citado na página 29.

CHEVILLOTTE, F. et al. Microstructure based model for sound absorption predictions of perforated closed-cell metallic foams. *The Journal of the Acoustical Society of America*, Acoustical Society of America (ASA), v. 128, n. 4, p. 1766–1776, out. 2010. Disponível em: <https://doi.org/10.1121/1.3473696>. Citado na página 12.

CHU, Y. et al. Preparation of poly (l-lactic acid) with aligned structures by unidirectional freezing. *Polymers for Advanced Technologies*, v. 26, p. 606–612, 2015. ISSN 10991581. Citado na página 72.

CORTE, A. E. Vertical migration of particles in front of a moving freezing plane. *Journal of Geophysical Research (1896-1977)*, v. 67, n. 3, p. 1085–1090, 1962. Disponível em: <https://agupubs.onlinelibrary.wiley.com/doi/abs/10.1029/JZ067i003p01085>. Citado na página 30.

CORTIS, A. et al. Influence of pore roughness on high-frequency permeability. *Physics of Fluids*, v. 15, n. 6, p. 1766–1775, 2003. Disponível em: <https://aip.scitation.org/doi/abs/10.1063/1.1571545>. Citado na página 72.

COX, T.; D'ANTONIO, P. *Acoustic Absorbers and Diffusers*. CRC Press, 2016. Disponível em: <https://doi.org/10.1201/9781315369211>. Citado 5 vezes nas páginas 1, 14, 15, 18, and 22.

CUENCA, J. et al. Deterministic and statistical methods for the characterisation of poroelastic media from multi-observation sound absorption measurements. *Mechanical Systems and Signal Processing*, v. 163, 2022. ISSN 10961216. Citado na página 37.

CUIYUN, D. et al. Sound absorption characteristics of a high-temperature sintering porous ceramic material. *Applied Acoustics*, v. 73, n. 9, p. 865–871, 2012. ISSN 0003-682X. Disponível em: <https://www.sciencedirect.com/science/article/pii/S0003682X12000217>. Citado na página 5.

DELANY, M.; BAZLEY, E. Acoustical properties of fibrous absorbent materials. *Applied Acoustics*, v. 3, n. 2, p. 105–116, 1970. ISSN 0003-682X. Disponível em: <https://www.sciencedirect.com/science/article/pii/0003682X70900319>. Citado 3 vezes nas páginas 5, 8, and 18.

DEVILLE, S. Freeze-casting of porous ceramics: A review of current achievements and issues. *Advanced Engineering Materials*, v. 10, n. 3, p. 155–169, 2008. Disponível em: <https://onlinelibrary.wiley.com/doi/abs/10.1002/adem.200700270>. Citado 3 vezes nas páginas 4, 28, and 30.

DEVILLE, S. et al. In situ x-ray radiography and tomography observations of the solidification of aqueous alumina particle suspensions - part i: Initial instants. *Journal of the American Ceramic Society*, Blackwell Publishing Inc., v. 92, p. 2489–2496, 2009. ISSN 15512916. Citado na página 31.

DEVILLE, S. et al. In situ x-ray radiography and tomography observations of the solidification of aqueous alumina particles suspensions. part ii: Steady state. *Journal of the American Ceramic Society*, Blackwell Publishing Inc., v. 92, p. 2497–2503, 2009. ISSN 15512916. Citado na página 31.

DEVILLE, S. et al. Freeze casting of hydroxyapatite scaffolds for bone tissue engineering. *Biomaterials*, v. 27, n. 32, p. 5480–5489, 2006. ISSN 0142-9612. Disponível em: <https://www.sciencedirect.com/science/article/pii/S0142961206005801>. Citado na página 27.

DEVILLE, S. et al. Ice-templated porous alumina structures. *Acta Materialia*, v. 55, p. 1965–1974, 4 2007. ISSN 13596454. Citado 6 vezes nas páginas xi, 28, 29, 30, 32, and 53.

DONG, S. et al. Preparation of tubular hierarchically porous silicate cement compacts via a tert-butyl alcohol (tba)-based freeze casting method. *Chemical Engineering Journal*, v. 295, p. 530–541, 2016. ISSN 1385-8947. Disponível em: <https://www.sciencedirect.com/science/article/pii/S1385894716302534>. Citado na página 30.

DONG, X. et al. Multi-functional mullite fiber-based porous ceramics with a multilevel pore structure assembled by alumina platelets and mullite whiskers. *Ceramics International*, Elsevier BV, 9 2022. ISSN 02728842. Citado na página 6.

DOUTRES, O. et al. Effect of the microstructure closed pore content on the acoustic behavior of polyurethane foams. *Journal of Applied Physics*, v. 110, n. 6, p. 064901, 2011. Disponível em: <https://doi.org/10.1063/1.3631021>. Citado na página 9.

DU, Z. et al. Highly porous silica foams prepared via direct foaming with mixed surfactants and their sound absorption characteristics. *Ceramics International*, Elsevier Ltd and Techna Group S.r.l., v. 46, p. 12942–12947, 2020. ISSN 02728842. Disponível em: <https://doi.org/10.1016/j.ceramint.2020.02.063>. Citado na página 5.

DU, Z. et al. The sound absorption performance of the highly porous silica ceramics prepared using freeze casting method. *Journal of the American Ceramic Society*, v. 103, n. 10, p. 5990–5998, 2020. Disponível em: <https://ceramics.onlinelibrary.wiley.com/doi/abs/10.1111/jace.17300>. Citado na página 6.

DUPONT, T. et al. Acoustic methods for measuring the porosities of porous materials incorporating dead-end pores. *Journal of the Acoustical Society of America*, v. 133, 2013. ISSN 2136-2145. Disponível em: <https://hal.archives-ouvertes.fr/hal-01001818>. Citado na página 12.

EOM, J.-H. et al. Processing and properties of macroporous silicon carbide ceramics: A review. *Journal of Asian Ceramic Societies*, v. 1, n. 3, p. 220–242, 2013. ISSN 2187-0764. Disponível em: <https://www.sciencedirect.com/science/article/pii/S2187076413000523>. Citado 3 vezes nas páginas xi, 1, and 4.

FACKLER, C. J. et al. Bayesian acoustic analysis of multilayer porous media. *The Journal of the Acoustical Society of America*, v. 144, n. 6, p. 3582–3592, 2018. Disponível em: <https://doi.org/10.1121/1.5083835>. Citado 2 vezes nas páginas 37 and 38.

FAHY, F.; GARDONIO, P. 1 - waves in fluids and solid structures. In: FAHY, F.; GARDONIO, P. (Ed.). *Sound and Structural Vibration (Second Edition)*. Second edition. Oxford: Academic Press, 2007. p. 1–73. ISBN 978-0-12-373633-8. Disponível em: <https://www.sciencedirect.com/science/article/pii/B9780123736338500053>. Citado na página 10.

FMINSEARCH. Disponível em: <https://www.mathworks.com/help/matlab/ref/fminsearch.html>. Citado na página 38.

FRANK, G. et al. A novel production method for porous sound-absorbing ceramic material for high-temperature applications. *International Journal of Applied Ceramic Technology*, v. 8, n. 3, p. 646–652, 2011. Disponível em: <https://ceramics.onlinelibrary.wiley.com/doi/abs/10.1111/j.1744-7402.2009.02479.x>. Citado na página 5.

FU, Q. et al. Freeze-cast hydroxyapatite scaffolds for bone tissue engineering applications. *Biomedical Materials*, v. 3, n. 2, p. 025005, apr 2008. Disponível em: <https://dx.doi.org/10.1088/1748-6041/3/2/025005>. Citado 3 vezes nas páginas 4, 27, and 53.

FUJI, M. et al. Effects of surfactants on the microstructure and some intrinsic properties of porous building ceramics fabricated by gelcasting. *Ceramics International*, v. 32, n. 7, p. 797–802, 2006. ISSN 0272-8842. Disponível em: <https://www.sciencedirect.com/science/article/pii/S0272884205001835>. Citado na página 5.

FUKASAWA, T. et al. Filtering properties of porous ceramics with unidirectionally aligned pores. *Journal of the Ceramic Society of Japan*, p. 627–631, 2002. ISSN 0914-5400. Citado 2 vezes nas páginas 26 and 32.

FUKASAWA, T. et al. Synthesis of porous ceramics with complex pore structure by freeze-dry processing. *Journal of the American Ceramic Society*, American Ceramic Society, v. 84, p. 230–232, 2001. ISSN 00027820. Citado na página 34.

FUKUSHIMA, M. et al. Fabrication and properties of ultra highly porous silicon carbide by the gelation-freezing method. *Journal of the European Ceramic Society*, v. 30, p. 2889–2896, 10 2010. ISSN 09552219. Citado na página 53.

GANESH, I. A review on magnesium aluminate (mgal ₂ o ₄) spinel: synthesis, processing and applications. *International Materials Reviews*, v. 58, p. 63–112, 2 2013. ISSN 0950-6608. Disponível em: <http://www.tandfonline.com/doi/full/10.1179/1743280412Y.0000000001>. Citado 2 vezes nas páginas 35 and 62.

GASSER, S. et al. Absorptive properties of rigid porous media: Application to face centered cubic sphere packing. *The Journal of the Acoustical Society of America*, v. 117, n. 4, p. 2090–2099, 2005. Disponível em: <https://doi.org/10.1121/1.1863052>. Citado na página 9.

GAUDILLERE, C.; SERRA, J. M. Freeze-casting: Fabrication of highlyporous and hierarchical ceramic supports for energy applications. *Boletin de la Sociedad Espanola de Ceramica y Vidrio*, SECV, v. 55, p. 45–54, 2016. ISSN 21730431. Disponível em: <http://dx.doi.org/10.1016/j.bsecv.2016.02.002>. Citado na página 2.

GHOSH, D. et al. A comparison of microstructure and uniaxial compressive response of ice-templated alumina scaffolds fabricated from two different particle sizes. *Ceramics International*, Elsevier Ltd, v. 42, p. 16138–16147, 11 2016. ISSN 02728842. Citado na página 53.

GIESCHE, H. Mercury porosimetry: A general (practical) overview. In: . [S.l.: s.n.], 2006. v. 23, p. 9–19. ISSN 09340866. Citado na página 57.

GLOBAL Optimization Toolbox. MathWorks. Disponível em: <https://www.mathworks.com/products/global-optimization.html>. Citado na página 44.

HE, C. et al. Enhanced sound absorption properties of ceramics with graphene oxide composites. *ACS Omega*, v. 6, p. 34242–34249, 12 2021. ISSN 2470-1343. Disponível em: <https://pubs.acs.org/doi/10.1021/acsomega.1c03362>. Citado na página 6.

HONG, C. et al. Functionally graded porous ceramics with dense surface layer produced by freeze-casting. *Ceramics International*, v. 37, p. 3717–3722, 2011. ISSN 02728842. Esse aqui tem dimensões aproximadas da camada densa de material, além de mostrar a estrutura formada pelo freeze-casting
. Citado 5 vezes nas páginas xi, 31, 32, 50, and 57.

INTERNATIONAL ORGANIZATION FOR STANDARDIZATION. *ISO 10534-2*: Acoustics — determination of sound absorption coefficient and impedance in impedance tubes — part 2: Transfer-function method. Geneva, CH, 1998. Citado na página 52.

INTERNATIONAL ORGANIZATION FOR STANDARDIZATION. *ISO 9053-1*: Acoustics — determination of airflow resistance — part 1: Static airflow method. Geneva, CH, 2018. Citado 3 vezes nas páginas xi, 19, and 20.

INTERNATIONAL ORGANIZATION FOR STANDARDIZATION. *ISO 9053-2*: Acoustics — determination of airflow resistance — part 2: Alternating airflow method. Geneva, CH, 2020. Citado na página 19.

JAOUEN, L. *Characterization of the tortuosity of acoustical porous materials*. Matelys, 2021. Disponível em: <https://apmr.matelys.com/Parameters/Characterization/Acoustics/HFLimitOfTortuosity.html>. Citado na página 20.

JAOUEN, L. et al. Estimation of all six parameters of johnson-champoux-allard-lafarge model for acoustical porous materials from impedance tube measurements. *The Journal of the Acoustical Society of America*, Acoustical Society of America, v. 148, p. 1998–2005, 2020. ISSN 0001-4966. Citado 3 vezes nas páginas 22, 60, and 66.

JIA, C. et al. Highly compressible and anisotropic lamellar ceramic sponges with superior thermal insulation and acoustic absorption performances. *Nature Communications*, v. 11, p. 1–13, 2020. ISSN 20411723. Citado na página 6.

JOHNSON, D. L. Equivalence between fourth sound in liquid he ii at low temperatures and the biot slow wave in consolidated porous media. *Applied Physics Letters*, v. 37, p. 1065–1067, 1980. ISSN 00036951. Citado na página 20.

JOHNSON, D. L. et al. Theory of dynamic permeability and tortuosity in fluid-saturated porous media. *Journal of Fluid Mechanics*, Cambridge University Press, v. 176, p. 379–402, 1987. Citado 6 vezes nas páginas 6, 13, 14, 15, 20, and 46.

JOHNSON, D. L. et al. Tortuosity and acoustic slow waves. *Phys. Rev. Lett.*, American Physical Society, v. 49, p. 1840–1844, Dec 1982. Disponível em: <https://link.aps.org/doi/10.1103/PhysRevLett.49.1840>. Citado na página 19.

JOHNSON, D. L.; SEN, P. N. Multiple scattering of acoustic waves with application to the index of refraction of fourth sound. *Phys. Rev. B*, American Physical Society, v. 24, p. 2486–2496, Sep 1981. Disponível em: <https://link.aps.org/doi/10.1103/PhysRevB.24.2486>. Citado na página 15.

KINGERY, W. D. et al. *Introduction to ceramics*. 2nd. ed. [S.l.]: Wiley-Blackwell, 1976. Citado 2 vezes nas páginas xi and 33.

KIRCHHOFF, G. Ueber den einfluss der wärmeleitung in einem gase auf die schallbewegung. *Annalen der Physik*, v. 210, n. 6, p. 177–193, 1868. Disponível em: <https://onlinelibrary.wiley.com/doi/abs/10.1002/andp.18682100602>. Citado na página 8.

KOH, Y. H. et al. Freezing dilute ceramic/camphene slurry for ultra-high porosity ceramics with completely interconnected pore networks. *Journal of the American Ceramic Society*, v. 89, p. 3089–3093, 2006. ISSN 00027820. Citado na página 27.

LAFARGE, D. et al. Characteristic dimensions and prediction at high frequencies of the surface impedance of porous layers. *The Journal of the Acoustical Society of America*, v. 93, n. 5, p. 2474–2478, 1993. Disponível em: <https://doi.org/10.1121/1.405868>. Citado na página 21.

LAFARGE, D. et al. Dynamic compressibility of air in porous structures at audible frequencies. *The Journal of the Acoustical Society of America*, v. 102, n. 4, p. 1995–2006, 1997. Disponível em: <https://doi.org/10.1121/1.419690>. Citado 6 vezes nas páginas 6, 13, 15, 16, 21, and 46.

LECLAIRE, P. et al. Determination of the viscous characteristic length in air-filled porous materials by ultrasonic attenuation measurements. *The Journal of the Acoustical Society of America*, Acoustical Society of America (ASA), v. 99, p. 1944–1948, 4 1996. ISSN 0001-4966. Citado na página 20.

LECLAIRE, P. et al. Porosity measurement by comparison of air volumes. *Review of Scientific Instruments*, v. 74, p. 1366–1370, 3 2003. ISSN 0034-6748. Disponível em: <http://aip.scitation.org/doi/10.1063/1.1542666>. Citado na página 18.

LEE, E. J. et al. Highly porous hydroxyapatite bioceramics with interconnected pore channels using camphene-based freeze casting. *Materials Letters*, v. 61, p. 2270–2273, 5 2007. ISSN 0167577X. Citado na página 53.

LEVENBERG, K. A method for the solution of certain non-linear problems in least squares. *Quarterly of Applied Mathematics*, Brown University, v. 2, n. 2, p. 164–168, 1944. ISSN 0033569X, 15524485. Disponível em: <http://www.jstor.org/stable/43633451>. Citado na página 38.

LI, W. L. et al. Freeze casting of porous materials: Review of critical factors in microstructure evolution. *International Materials Reviews*, v. 57, p. 37–60, 2012. ISSN 09506608. Citado 2 vezes nas páginas 28 and 30.

MACCHETTA, A. et al. Fabrication of ha/tcp scaffolds with a graded and porous structure using a camphene-based freeze-casting method. *Acta Biomaterialia*, v. 5, n. 4, p. 1319–1327, 2009. ISSN 1742-7061. Disponível em: <https://www.sciencedirect.com/science/article/pii/S1742706108003590>. Citado na página 27.

MACCHETTA, A. et al. Fabrication of ha/tcp scaffolds with a graded and porous structure using a camphene-based freeze-casting method. *Acta Biomaterialia*, Acta Materialia Inc., v. 5, p. 1319–1327, 2009. ISSN 17427061. Disponível em: <http://dx.doi.org/10.1016/j.actbio.2008.11.009>. Citado na página 32.

MAGLIACANO, D. et al. Computation of dispersion diagrams for periodic porous materials modeled as equivalent fluids. *Mechanical Systems and Signal Processing*, v. 142, p. 106749, 2020. ISSN 0888-3270. Disponível em: <https://www.sciencedirect.com/science/article/pii/S0888327020301357>. Citado na página 48.

MAHASARANON, S. et al. The effect of continuous pore stratification on the acoustic absorption in open cell foams. *Journal of Applied Physics*, v. 111, 4 2012. ISSN 00218979. Citado 2 vezes nas páginas 49 and 61.

MAREZE, P. H. *Análise da influência da microgeometria na absorção sonora de materiais porosos de estrutura rígida*. 2013. Tese (Doutorado). Citado 2 vezes nas páginas 8 and 15.

MARQUARDT, D. W. An algorithm for least-squares estimation of nonlinear parameters. *Journal of the Society for Industrial and Applied Mathematics*, Society for Industrial and Applied Mathematics, v. 11, n. 2, p. 431–441, 1963. ISSN 03684245. Disponível em: <http://www.jstor.org/stable/2098941>. Citado na página 38.

MATHWORKS. *rand*. Disponível em: <https://www.mathworks.com/help/matlab/ref/rand.html>. Citado na página 39.

MECHEL, F. Extending the absorption formulae of delaney and bazley to low frequencies.; [ausweitung der absorberformel von delany und bazley zu tiefen frequenzen.]. *Acustica*, v. 35, n. 3, p. 210 – 213, 1976. Cited by: 62. Disponível em: <https://www.scopus.com/inward/record.uri?eid=2-s2.0-0016965042&partnerID=40&md5=46a8dcc382ec4d0338641685c995a543>. Citado 2 vezes nas páginas 5 and 8.

MENDES, C. O. B. *CARACTERIZAÇÃO ACÚSTICA DE AMOSTRAS CONFECCIONADAS COM A FIBRA EXTRAÍDA DO PSEUDOCAULE DA BANANEIRA (Musa spp.)*. 2020. Tese (Doutorado) — Universidade de Brasília. Citado na página 52.

MIKI, Y. Acoustical properties of porous materials-modifications of delany-bazley models-. *Journal of the Acoustical Society of Japan (E)*, v. 11, n. 1, p. 19–24, 1990. Citado na página 8.

NELDER, J. A.; MEAD, R. A simplex method for function minimization. *The Computer Journal*, Oxford University Press (OUP), v. 7, n. 4, p. 308–313, jan. 1965. Disponível em: <https://doi.org/10.1093/comjnl/7.4.308>. Citado na página 38.

NISKANEN, M. et al. Deterministic and statistical characterization of rigid frame porous materials from impedance tube measurements. *The Journal of the Acoustical Society of America*, Acoustical Society of America (ASA), v. 142, p. 2407–2418, 10 2017. ISSN 0001-4966. Citado 2 vezes nas páginas 21 and 37.

OLNY, X.; PANNETON, R. Acoustical determination of the parameters governing thermal dissipation in porous media. *The Journal of the Acoustical Society of America*, Acoustical Society of America (ASA), v. 123, p. 814–824, 2 2008. ISSN 0001-4966. Citado na página 21.

OUISSE, M. et al. On the sensitivity analysis of porous material models. *Journal of Sound and Vibration*, v. 331, p. 5292–5308, 2012. Disponível em: <https://hal.archives-ouvertes.fr/hal-02300228>. Citado 2 vezes nas páginas 48 and 69.

PANNETON, R.; GROS, E. A missing mass method to measure the open porosity of porous solids. *Acta Acustica united with Acustica*, v. 91, n. 2, p. 342 – 348, 2005. Cited by: 22. Disponível em: <https://www.scopus.com/inward/record.uri?eid=2-s2.0-17044385042&partnerID=40&md5=818759c130167969891abcf20bfa6151>. Citado 2 vezes nas páginas 18 and 43.

PANNETON, R.; OLNY, X. Acoustical determination of the parameters governing viscous dissipation in porous media. *The Journal of the Acoustical Society of America*, Acoustical Society of America (ASA), v. 119, p. 2027–2040, 4 2006. ISSN 0001-4966. Citado na página 21.

PAPA, E. et al. Synthesis of porous hierarchical geopolymer monoliths by ice-templating. *Microporous and Mesoporous Materials*, v. 215, p. 206–214, 2015. ISSN 1387-1811. Disponível em: <https://www.sciencedirect.com/science/article/pii/S1387181115003121>. Citado na página 4.

PIERCE, A. *Acoustics: An Introduction to Its Physical Principles and Applications*. Springer International Publishing, 2019. ISBN 9783030112141. Disponível em: <https://books.google.com.br/books?id=MAGfDwAAQBAJ>. Citado na página 10.

PRESS, W. H. et al. *Numerical recipes in c the Art of Scientific Computing Second Edition*. [S.l.]: Cambridge University Press, 1992. Citado 2 vezes nas páginas 41 and 97.

QIN, K. et al. Recent advances in ice templating: From biomimetic composites to cell culture scaffolds and tissue engineering. *Journal of Materials Chemistry B*, Royal Society of Chemistry, v. 9, p. 889–907, 1 2021. ISSN 20507518. Citado na página 26.

RAHAMAN, M. N. *Ceramic Processing and Sintering*. CRC Press, 2017. Disponível em: <https://doi.org/10.1201/9781315274126>. Citado 2 vezes nas páginas 28 and 33.

RAHAMAN, M. N.; FU, Q. Manipulation of porous bioceramic microstructures by freezing of suspensions containing binary mixtures of solvents. *Journal of the American Ceramic Society*, v. 91, n. 12, p. 4137–4140, 2008. Disponível em: <https://ceramics.onlinelibrary.wiley.com/doi/abs/10.1111/j.1551-2916.2008.02795.x>. Citado 2 vezes nas páginas 4 and 33.

REBILLARD, P. et al. The effect of a porous facing on the impedance and the absorption coefficient of a layer of porour material. *Journal of Sound and Vibration*, v. 156, n. 3, p. 541–555, 1992. ISSN 0022-460X. Disponível em: <https://www.sciencedirect.com/science/article/pii/0022460X9290743H>. Citado na página 48.

REN, L. et al. Fabrication of gradient pore tio2 sheets by a novel freeze–tape-casting process. *Journal of the American Ceramic Society*, v. 90, n. 9, p. 3001–3004, 2007. Disponível em: <https://ceramics.onlinelibrary.wiley.com/doi/abs/10.1111/j.1551-2916.2007.01833.x>. Citado na página 2.

REN, S. et al. Manufacturing and semi-analytical modeling of environment-friendly sound absorbent porous glasses. *Applied Acoustics*, v. 185, p. 108444, 2022. ISSN 0003-682X. Disponível em: <https://www.sciencedirect.com/science/article/pii/S0003682X21005387>. Citado na página 9.

RIES, H.-C. et al. On the performance of porous sound absorbent ceramic lining in a combustion chamber test rig. *Volume 4: Ceramics; Concentrating Solar Power Plants; Controls, Diagnostics and Instrumentation; Education; Electric Power; Fans and Blowers*, American Society of Mechanical Engineers, v. 4, p. 1–6, 6 2013. Disponível em: <https://asmedigitalcollection.asme.org/GT/proceedings/GT2013/55188/San%20Antonio,%20Texas,%20USA/247224>. Citado na página 2.

RONCEN, R. et al. Addressing the ill-posedness of multi-layer porous media characterization in impedance tubes through the addition of air gaps behind the sample: Numerical validation. *Journal of Sound and Vibration*, Elsevier Ltd, v. 520, p. 116601, 2022. ISSN 10958568. Disponível em: <https://doi.org/10.1016/j.jsv.2021.116601>. Citado 2 vezes nas páginas 37 and 38.

RYCK, L. D. et al. Reconstruction of material properties profiles in one-dimensional macroscopically inhomogeneous rigid frame porous media in the frequency domain. *The Journal of the Acoustical Society of America*, v. 124, p. 1591–1606, 2008. ISSN 0001-4966. Esse é o artigo em que ele aborda diferentes caminhos para obter mais informação para as medidas.
. Citado 2 vezes nas páginas 37 and 38.

RYMANSAIB, Z. et al. Ultrasonic transducers made from freeze-cast porous piezoceramics. *IEEE Transactions on Ultrasonics, Ferroelectrics, and Frequency Control*, Institute of Electrical and Electronics Engineers Inc., v. 69, p. 1100–1111, 2022. ISSN 15258955. Citado 2 vezes nas páginas 2 and 26.

SALISSOU, Y.; PANNETON, R. Pressure/mass method to measure open porosity of porous solids. *Journal of Applied Physics*, v. 101, 2007. ISSN 00218979. Citado na página 18.

SCHEIDEGGER, A. E. *The Physics of Flow Through Porous Media (3rd Edition)*. University of Toronto Press, 1974. ISBN 9781487582395. Disponível em: <http://www.jstor.org/stable/10.3138/j.ctvfrxmtw>. Citado na página 14.

SCIENTIFIC, T. F. *Amira-Avizo Software*. Thermo Fisher Scientific. Disponível em: <https://cases.amira-avizo.com/>. Citado na página 72.

SCIPY.OPTIMIZE.MINIMIZE. Disponível em: <https://docs.scipy.org/doc/scipy/reference/generated/scipy.optimize.minimize.html>. Citado na página 45.

SCOTTI, K. L.; DUNAND, D. C. Freeze casting – a review of processing, microstructure and properties via the open data repository, freezecasting.net. *Progress in Materials Science*, v. 94, p. 243–305, 2018. ISSN 0079-6425. Disponível em: <https://www.sciencedirect.com/science/article/pii/S007964251830001X>. Citado 4 vezes nas páginas xi, 2, 27, and 29.

SGARD, F. et al. On the use of perforations to improve the sound absorption of porous materials. *Applied Acoustics*, v. 66, n. 6, p. 625–651, 2005. ISSN 0003-682X. Innovative Applications of Materials for Acoustic Purposes. Disponível em: <https://www.sciencedirect.com/science/article/pii/S0003682X04001768>. Citado na página 77.

SHAND, M. A. *The Chemistry and Technology of Magnesia*. John Wiley & Sons, Inc., 2006. Disponível em: <https://doi.org/10.1002/0471980579>. Citado na página 34.

SHAO, G. et al. Freeze casting: From low-dimensional building blocks to aligned porous structures—a review of novel materials, methods, and applications. *Advanced Materials*, Wiley-VCH Verlag, v. 32, 4 2020. ISSN 15214095. Citado na página 29.

SHIRAHATTI, U. S.; MUNJAL, M. L. Acoustic characterization of porous ceramic tiles. *Noise Control Engineering Journal*, Institute of Noise Control Engineering (INCE), v. 28, n. 1, p. 26, 1987. Disponível em: <https://doi.org/10.3397/1.2827678>. Citado na página 4.

SHRAVAGE, P. et al. Hybrid inversion technique for predicting geometrical parameters of porous materials. *The Journal of the Acoustical Society of America*, v. 123, p. 3284–3284, 5 2008. ISSN 0001-4966. Disponível em: <http://asa.scitation.org/doi/10.1121/1.2933653>. Citado na página 37.

SMITH, C. D.; PARROTT, T. L. Comparison of three methods for measuring acoustic properties of bulk materials. *The Journal of the Acoustical Society of America*, v. 74, n. 5, p. 1577–1582, 1983. Disponível em: <https://doi.org/10.1121/1.390119>. Citado na página 22.

SOFIE, S. W. Fabrication of functionally graded and aligned porosity in thin ceramic substrates with the novel freeze–tape-casting process. *Journal of the American Ceramic Society*, v. 90, n. 7, p. 2024–2031, 2007. Disponível em: <https://ceramics.onlinelibrary.wiley.com/doi/abs/10.1111/j.1551-2916.2007.01720.x>. Citado na página 26.

SOLTANI, P.; NOROUZI, M. Prediction of the sound absorption behavior of nonwoven fabrics: Computational study and experimental validation. *Journal of Sound and Vibration*, v. 485, p. 115607, 2020. ISSN 0022-460X. Disponível em: <https://www.sciencedirect.com/science/article/pii/S0022460X20304387>. Citado na página 9.

SONG, S. Y. et al. Modeling of roughness effects on acoustic properties of micro-slits. *Journal of Physics D: Applied Physics*, Institute of Physics Publishing, v. 50, 5 2017. ISSN 13616463. Citado na página 72.

STINSON, M. R. The propagation of plane sound waves in narrow and wide circular tubes, and generalization to uniform tubes of arbitrary cross-sectional shape. *The Journal of the Acoustical Society of America*, v. 89, n. 2, p. 550–558, 1991. Disponível em: <https://doi.org/10.1121/1.400379>. Citado na página 11.

STUDART, A. R. et al. Processing routes to macroporous ceramics: A review. *Journal of the American Ceramic Society*, v. 89, n. 6, p. 1771–1789, 2006. Disponível em: <https://ceramics.onlinelibrary.wiley.com/doi/abs/10.1111/j.1551-2916.2006.01044.x>. Citado 2 vezes nas páginas 1 and 3.

SU, F. Y. et al. Radial-concentric freeze casting inspired by porcupine fish spines. *Ceramics*, MDPI, v. 2, p. 161–179, 3 2019. ISSN 25716131. Citado na página 29.

SURENDRANATHAN, A. O. *An introduction to ceramics and refractories*. [S.l.]: CRC Press, an imprint of Taylor et Francis, 2020. Citado na página 34.

TAKAHARA, H. The sound absorption characteristics of particulate porous ceramic materials. *Applied Acoustics*, v. 41, n. 3, p. 265–274, 1994. ISSN 0003-682X. Disponível em: <https://www.sciencedirect.com/science/article/pii/0003682X94900760>. Citado 2 vezes nas páginas 4 and 5.

TANG, Y. et al. Novel freeze-casting fabrication of aligned lamellar porous alumina with a centrosymmetric structure. *Journal of the European Ceramic Society*, Elsevier Ltd, v. 34, p. 4077–4082, 2014. ISSN 09552219. Disponível em: <http://dx.doi.org/10.1016/j.jeurceramsoc.2014.05.040>. Citado 2 vezes nas páginas 2 and 29.

TANNEAU, O. et al. Optimization of multilayered panels with poroelastic components for an acoustical transmission objective. *The Journal of the Acoustical Society of America*, v. 120, n. 3, p. 1227–1238, 2006. Disponível em: <https://doi.org/10.1121/1.2228663>. Citado na página 49.

TARNOW, V. Measurement of sound propagation in glass wool. *Journal of the Acoustical Society of America*, v. 97, p. 2272–2281, 1995. ISSN NA. Citado na página 21.

THUNEBERG, E. Superfluidity. In: BASSANI, F. et al. (Ed.). *Encyclopedia of Condensed Matter Physics*. Oxford: Elsevier, 2005. p. 128–133. ISBN 978-0-12-369401-0. Disponível em: <https://www.sciencedirect.com/science/article/pii/B0123694019007105>. Citado na página 20.

TRINH, V. et al. On the sensitivity of the design of composite sound absorbing structures. *Materials & Design*, v. 210, p. 110058, 2021. ISSN 0264-1275. Disponível em: <https://www.sciencedirect.com/science/article/pii/S0264127521006134>. Citado na página 48.

TSAI, Y. Nonlinear least-squares analyses of complex impedance and admittance data for solid electrolytes. *Solid State Ionics*, v. 7, p. 129–139, 9 1982. ISSN 01672738. Disponível em: <https://linkinghub.elsevier.com/retrieve/pii/0167273882900066>. Citado na página 97.

UHLMANN, D. R. et al. Interaction between particles and a solid-liquid interface. *Journal of Applied Physics*, v. 35, n. 10, p. 2986–2993, 1964. Disponível em: <https://doi.org/10.1063/1.1713142>. Citado 2 vezes nas páginas 29 and 30.

USMAN, M. A.; KHAN, A. Y. Candle soot particles-modified macroporous monoliths for efficient separation of floating oil/water and stable emulsions. *Colloids and Surfaces A: Physicochemical and Engineering Aspects*, Elsevier B.V., v. 619, p. 126492, 2021. ISSN 18734359. Disponível em: <https://doi.org/10.1016/j.colsurfa.2021.126492>. Citado na página 2.

UTSUNO, H. et al. Transfer function method for measuring characteristic impedance and propagation constant of porous materials. *The Journal of the Acoustical Society of America*, v. 86, n. 2, p. 637–643, 1989. Disponível em: <https://doi.org/10.1121/1.398241>. Citado na página 22.

VIJAYAN, S. et al. Freeze gelcasting of hydrogenated vegetable oil-in-aqueous alumina slurry emulsions for the preparation of macroporous ceramics. *Journal of the European Ceramic Society*, v. 34, n. 16, p. 4347–4354, 2014. ISSN 0955-2219. Disponível em: <https://www.sciencedirect.com/science/article/pii/S0955221914003823>. Citado na página 2.

WANG, F. et al. Porous si3n4 fabrication via volume-controlled foaming and their sound absorption properties. *Journal of Alloys and Compounds*, v. 727, p. 163–167, 2017. ISSN 0925-8388. Disponível em: <https://www.sciencedirect.com/science/article/pii/S0925838817326087>. Citado na página 5.

WANG, W. et al. A novel fabrication approach for improving the mechanical and sound absorbing properties of porous sound-absorbing ceramics. *Journal of Alloys and Compounds*, Elsevier Ltd, v. 695, p. 2477–2482, 2 2017. ISSN 09258388. Citado na página 5.

WASCHKIES, T. et al. Control of lamellae spacing during freeze casting of ceramics using double-side cooling as a novel processing route. *Journal of the American Ceramic Society*, v. 92, n. s1, p. S79–S84, 2009. Disponível em: <https://ceramics.onlinelibrary.wiley.com/doi/abs/10.1111/j.1551-2916.2008.02673.x>. Citado na página 31.

WILAMOWSKI, B. M.; YU, H. Improved computation for levenberg–marquardt training. *IEEE Transactions on Neural Networks*, Institute of Electrical and

Electronics Engineers (IEEE), v. 21, n. 6, p. 930–937, jun 2010. Disponível em: <https://doi.org/10.1109%2Ftnn.2010.2045657>. Citado na página 41.

XIE, Y. et al. High temperature and high strength y2zr2o7 flexible fibrous membrane for efficient heat insulation and acoustic absorption. *Chemical Engineering Journal*, Elsevier B.V., v. 416, p. 128994, 2021. ISSN 13858947. Disponível em: <https://doi.org/10.1016/j.cej.2021.128994>. Citado na página 6.

XU, T.; WANG, C.-A. Control of pore size and wall thickness of 3-1 type porous pzt ceramics during freeze-casting process. *Materials & Design*, v. 91, p. 242–247, 2016. ISSN 0264-1275. Disponível em: <https://www.sciencedirect.com/science/article/pii/S026412751530842X>. Citado 2 vezes nas páginas 4 and 67.

YAMAMOTO, T. et al. Thickness optimization of a multilayered structure on the coupling surface between a structure and an acoustic cavity. *Journal of Sound and Vibration*, v. 318, n. 1, p. 109–130, 2008. ISSN 0022-460X. Disponível em: <https://www.sciencedirect.com/science/article/pii/S0022460X08003313>. Citado na página 49.

YAN, N. et al. Preparation of pore-controllable zirconium carbide ceramics with tunable mechanical strength, thermal conductivity and sound absorption coefficient. *Ceramics International*, Elsevier Ltd and Techna Group S.r.l., v. 46, p. 19609–19616, 2020. ISSN 02728842. Disponível em: <https://doi.org/10.1016/j.ceramint.2020.05.023>. Citado 2 vezes nas páginas 5 and 6.

ZHANG, F.-Z. et al. Gelcasting fabrication of porous ceramics using a continuous process. *Journal of the European Ceramic Society*, v. 26, n. 4, p. 667–671, 2006. ISSN 0955-2219. Proceedings of the International Symposium on Inorganic and Environmental Materials, Eindhoven, NL, October 2004. Disponível em: <https://www.sciencedirect.com/science/article/pii/S0955221905006357>. Citado na página 5.

ZHANG, H. X. et al. Aligned and porous alumina ceramics prepared by camphene-based freeze-casting route: microstructure and properties. *Materials Research Innovations*, Taylor & Francis, v. 19, n. sup4, p. S34–S38, 2015. Disponível em: <https://doi.org/10.1179/1432891715Z.0000000001512>. Citado 3 vezes nas páginas xi, 27, and 28.

ZIELINSKI, T. G. et al. Benchmarks for microstructure-based modelling of sound absorbing rigid-frame porous media. *Journal of Sound and Vibration*, v. 483, p. 115441, 2020. ISSN 0022-460X. Disponível em: <https://www.sciencedirect.com/science/article/pii/S0022460X2030273X>. Citado 2 vezes nas páginas 9 and 72.

ZIELIńSKI, T. G. Inverse identification and microscopic estimation of parameters for models of sound absorption in porous ceramics. *International Conference on Noise and Vibration Engineering 2012, ISMA 2012, including USD 2012: International Conference on Uncertainty in Structure Dynamics*, v. 1, p. 95–108, 2012. Citado na página 37.

ZIELIńSKI, T. G. Normalized inverse characterization of sound absorbing rigid porous media. *The Journal of the Acoustical Society of America*, v. 137, n. 6, p. 3232–3243, 2015. Disponível em: <https://doi.org/10.1121/1.4919806>. Citado 4 vezes nas páginas 17, 37, 41, and 42.

ZIELIńSKI, T. G. Pore-size effects in sound absorbing foams with periodic microstructure: Modelling and experimental verification using 3d printed specimens. *Proceedings of ISMA 2016 - International Conference on Noise and Vibration Engineering and USD2016 - International Conference on Uncertainty in Structural Dynamics*, p. 95–104, 2016. Citado na página 61.

ZOLTOWSKI, P. The error function for fitting of models to immittance. *J Electroanal. Chem*, Elsevier Sequoia S.A, v. 178, p. 11–19, 1984. Citado na página 40.

ZONG, D. et al. Bubble templated flexible ceramic nanofiber aerogels with cascaded resonant cavities for high-temperature noise absorption. *ACS Nano*, American Chemical Society, 9 2022. ISSN 1936086X. Citado na página 6.

ZWIKKER, C.; KOSTEN, C. W. *Sound absorbing materials*. New York: Elsevier Pub. Co., 1949. Citado 2 vezes nas páginas 8 and 9.

Appendices

A Appendix 1: Levenberg Marquardt and gradient equations

Aiming at minimizing a given cost function, dependent of frequencies ω and parameter vector $\mathbf{a}$

$$R(\omega;\mathbf{a}) = 0.5\sum_{\omega}\frac{1}{\sigma_{\text{er}}}|Z^{exp}(\omega) - Z(\omega,\mathbf{a})|^2, \tag{A.1}$$

different parameter sets (vectors) are updated from a starting guess to a final parameter vector that yields a minimum cost function value.

Most deterministic methods rely on the gradient (jacobian) $\nabla R(\omega;\mathbf{a})$ and the Hessian matrix $\nabla^2 R(\omega;\mathbf{a})$. Considering the imaginary and real component of surface impedance Z, the gradient of the cost function is given by (TSAI, 1982)

$$\begin{aligned}\frac{\partial R}{\partial a_k} =& \sum_{i}^{n}\frac{1}{\sigma_{\text{er}}}\Bigg\{\text{Re}(Z^{exp}(\omega_i) - Z(\omega_i,\mathbf{a}))\text{Re}\left(\frac{\partial Z(\omega_i,\mathbf{a})}{a_k}\right) + \\ &+ \text{Im}(Z_i^{exp}(\omega_i) - Z_i(\omega_i,\mathbf{a}))\text{Im}\left(\frac{\partial Z_i(\omega_i,\mathbf{a})}{a_k}\right)\Bigg\},\end{aligned} \tag{A.2}$$

where n is the amount of sampled frequency points and a_k is an element of the parameter vector. Similarly, the hessian is given by

$$\begin{aligned}\frac{\partial^2 R}{\partial a_k \partial a_l} =& \sum_{i}^{n}\frac{1}{\sigma_{\text{er}}}\Bigg\{ - \text{Re}\left(\frac{\partial Z(\omega_i,\mathbf{a})}{\partial a_k}\frac{\partial Z(\omega_i,\mathbf{a})}{\partial a_l}\right) + \text{Re}\left[(Z_i^{exp}(\omega_i) - Z_i(\omega_i,\mathbf{a}))\frac{\partial^2 Z_i(\omega_i,\mathbf{a})}{\partial a_k \partial a_l}\right] \\ &- \text{Im}\left(\frac{\partial Z(\omega_i,\mathbf{a})}{\partial a_k}\frac{\partial Z(\omega_i,\mathbf{a})}{\partial a_l}\right) + \text{Im}\left[(Z_i^{exp}(\omega_i) - Z_i(\omega_i,\mathbf{a}))\frac{\partial^2 Z_i(\omega_i,\mathbf{a})}{\partial a_k \partial a_l}\right]\Bigg\}.\end{aligned} \tag{A.3}$$

The Levenberg-Marquardt method consists on updating an initial guess a_0 by a vector δa_l the same size as a_0 every iteration until a a vector that yields a minimum value for the cost function. It is based on a matrix α'_{kl} defined as (PRESS; TEUKOLSKY; VETTERLING, 1992)

$$\begin{aligned} \alpha'_{jj} &= \frac{\partial^2 R}{\partial a_j \partial a_j}(1+\lambda) \\ \alpha'_{jk} &= \frac{\partial^2 R}{\partial a_j \partial a_k}, \end{aligned} \tag{A.4}$$

where λ is a fudge factor.

Then, the vector δa_l is given by

$$\delta a_l = \frac{1}{2}\alpha'^{-1}. \tag{A.5}$$

The optimal method for updating the factor λ is subject to discussion, though the principle is always the same. The initial value for λ is small. An iteration starts with the solution of Eq. A.5. Then, $R(\mathbf{a}+\delta a_l)$ is evaluated and if $R(\mathbf{a}+\delta a_l) \geq R(\mathbf{a})$, then λ needs to be increased by a substantial factor, the update vector δa_l is subtracted from $\mathbf{a}$ and the iteration begins again using the new λ value. If $R(\mathbf{a}+\delta a_l) < R(\mathbf{a})$, then λ is decreased by a substantial factor and $\mathbf{a}$ becomes $\mathbf{a}+\delta a_l$, proceeding to a new iteration. This variation in the value of factor λ controls the proximity of the solution to either the Gauss-Newton method or the steepest descent method.

Anexxes

A Annnex 1

Module: Generate Pore Network Model *(Avizo XPoreNetworkModeling Extension)*

Description:

This module takes one input: a labeled image representing the separated pore space. It outputs the corresponding Pore Network Model. The extracted Pore Network Model contains the following statistics:

- Number of nodes
- Number of throats
- Coordination number
- Throat equivalent radius
- Throat channel length (defined as distance from pore to pore centers)
- Throat flow rate per second (if Generate Properties is enabled by the user)
- Pore volume
- Pore equivalent radius

If the Generate Properties is enabled by the user it also outputs a spreadsheet giving the following physical properties:

- Absolute permeability (in 2 different units: $darcy$ and μm^2).
- Total flow rate per second used to compute the absolute permeability (μm^3).
- Tortuosity that is a ratio value.

When Generate Properties is enabled this module also simulates an experiment leading to the computation of absolute permeability and tortuosity of the extracted Pore Network Model.

Theoretical details

The module implementation is inspired by [1]. A summary of the important considerations is provided below.
Absolute permeability: The flow is everywhere laminar (Poiseuille flow).
To calculate the absolute permeability of the model, it is assumed that the network is completely filled with only one phase. In steady state flow of an incompressible fluid, mass conservation for each pore body is described as:

$$\sum_{i->j} q_{ij} = 0$$

(1)

Where the summation is performed on all the pore j connected to the pore i ; q_{ij} representing the flow rate between pore i and pore j.
Under laminar flow conditions, the relation between pressure drop and flow rate is linear:

$$q_{ij} = g_{ij}(P_i - P_j)$$

(2)

g_{ij} represents the conductance of the throat between pore i and pore j. Since the conducting throats are represented by cylindrical pipes of radius r_{ij} and length l_{ij}, the hydraulic conductance is given by Poiseuille's law, where μ is the fluid viscosity:

$$g_{i,j} = \frac{\pi}{8\mu}\frac{r_{ij}^4}{l_{ij}}$$

By imposing a pressure difference across the network, this gives a linear system of equations which is solved numerically:

(1)(2) leads to the following matrix equation: $G * P = S$ Where G is the the matrix of conductance, a symmetrical matrix of dimension $N * N$, where N is the number of pores in the network; P is a vector of size N corresponding to the pressure in each pore, unknown of the problem; S is a vector of size N, constrained by the pressure boundary conditions at the inlet and the outlet of the system. The total flow rate can then be computed: Q=$\Sigma(P_i - P_j)g_{ij}$ on each pair of pore i,j intersecting an arbitrary cross section of surface A. The permeability k of the network is finally deduced from Darcy's law:

$$k = \frac{Q}{\Delta P}\frac{\mu L}{A}$$

Where ΔP is the gradient of pressure applied to the boundary (input pressure - output pressure) and L is the length of the network in the flow direction.

Tortuosity: The hydraulic tortuosity returned by the module is based on velocities deduced from the absolute permeability computation described above.
Knowing the velocities in each throat, the tortuosity is deduced by summing up the length of all velocities, divided by the sum of the projection of the velocities along the flow direction:

T = $\frac{\sum_{i=0}^{n} \|v_i\|}{\sum_{i=0}^{n} \|vx_i\|}$ with n being the number of throats, v_i being the velocity of the fluid passing through the throat i, and vx_i being the projection of the velocity along the flow direction of the fluid passing through the throat i.

Units and dimensions

The reference length (voxel size) is automatically converted to obtain μm^2 for absolute permeability. If the units management is activated (see the units management documentation), the reference length (voxel size) is automatically converted to obtain μm^2 for absolute permeability. If the units management is not activated, the voxel size that is indicated in the geometry file is considered to be in μm and the absolute permeability is still converted to μm^2. The permeability results are presented on two columns: the first is in μm^2, the second in darcy. The values are very close since 1 darcy, a common unit for permeability, almost equals 1 μm^2 (1d = 0,9869233 μm^2).

Important considerations

- The calculation of the properties and statistics should be in a correct order of magnitude for materials on which pore separation is possible, well defined and creating obvious throats (the pore network can be approximated by a simple model such as the PNM structure where pores are defined by spheres and throats are defined by cylindrical pipes).
  There is no guarantee that the results will be correct in other cases. For more details on cases where PNM is appropriate, you may refer to [2].
- The number of pore separation may influence the result of the properties. You may tune the PNM to obtain the same value of permeability using another method on the same sample (e.g. XLab Hydro), before further analyzing a bigger sample or a sample of the same type of material.

Connections:

Data `[required]`
The labeled image.

Ports:

Generate Properties

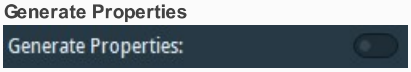

This option enables the Generate Properties options and makes the module generate a spreadsheet with the physical properties of the Pore Network Model generated by the module.

Direction

Visible if Generate Properties is enabled.
This option allows to define the direction of the main flow.

Boundary Values

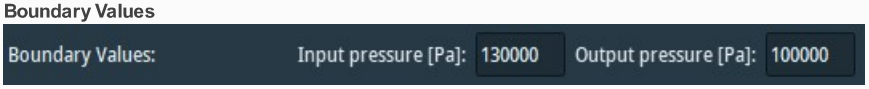

Visible if Generate Properties is enabled.
Input and output pressure imposing the pressure difference across the network. The units to use for pressure are Pa.
Note: absolute permeability is independent from boundary conditions. Only flow rates are rescaled according to the indicated values.

Fluid Viscosity

Visible if Generate Properties is enabled.
Value of the viscosity of the fluid used for experiment simulation (in $Pa.s$)
Note: absolute permeability is independent from boundary conditions. Only flow rates are rescaled according to the indicated values.

References:

[1] Youssef, S., Rosenberg, E., Gland, N. F., Kenter, J. A., Skalinski, M., and Vizika, O. (2007, January 1). High Resolution CT And Pore-Network Models To Assess Petrophysical Properties Of Homogeneous And Heterogeneous Carbonates. Society of Petroleum Engineers. doi:10.2118/111427-MS

[2] Combaret N. Construction d'un modèle de réseau de pores à partir d'une image 3D pour l'estimation de la perméabilité. Université Bordeaux 1, 2012. http://www.theses.fr/2012BOR14696